GAS ASSISTED INJECTION MOULDING: EXPERIMENT AND SIMULATION

Industrial machine experimental studies of the effect of process variables on gas bubble formation, and with simulation based upon a pseudo-concentration method.

Leigh MULVANEY-JOHNSON BEng, MSc

submitted for the degree
of Doctor of Philosophy

Department of Mechanical and Medical Engineering

University of Bradford

2001

Abstract

The gas assisted injection moulding process is an important extension to conventional injection moulding. Gas assist can be applied in a number of ways, but here the penetration of a gas bubble through the polymer melt is of interest. A 3D finite element implementation of a pseudo concentration method is employed to simulate the primary penetration of the gas bubble. The wall thickness prediction is an important result since the extent of bubble penetration is sensitive to the remaining melt fraction. A number of methods for experimental measurement are developed to measure characteristics of the gas assisted injection moulding process dynamics and product. Key process variables, on an industrial gas-assist machine, were measured and analysed, leading to an empirical model for wall thickness prediction. Gas delay time and injection velocity are shown to be most influential in controlling residual wall thickness. Simulation results are evaluated against the empirical model. The trends observed, for simulation and experiment, in wall thickness after changes in process variable settings are found to agree qualitatively. The wall thickness prediction is found to be within 10% of the experimentally obtained measurements.

Contents

1 Introduction **1**

1.1 An overview of the Gas Assisted Injection Moulding process . . . 3

1.1.1 Process advantages and implementation issues 6

1.1.2 Typical GAIM applications 9

1.1.3 Process features and mould design issues 11

1.1.4 Related processes 12

1.1.5 Methods for injecting gas 13

1.2 Modelling cavity filling 16

1.2.1 $2\frac{1}{2}$D and 3D results 16

1.2.2 A simple tube model 18

1.2.3 The pseudo-concentration method 20

1.3 Experimental facility 21

2 Literature review **24**

2.1 Introduction 24

2.2 Investigations into the GAIM process 25

2.2.1 Bubble penetration studies 25

2.2.2 Cavity filling observations of ribbed plaque moulds 32
2.2.3 Determining significant product characteristics and process variables 35
2.2.4 Dealing with process variation 36
2.3 Computer modelling of GAIM cavity filling and product performance 39
2.3.1 Modelling conventional cavity filling 40
2.3.2 Extensions to conventional modelling techniques for GAIM 41
2.3.3 Prediction of product performance from processing conditions 45

3 Experimental procedures 46

3.1 Introduction 46
3.2 Overview of the gas assisted injection moulding processing equipment 46
3.3 Process monitoring 48
3.3.1 LabVIEW data acquisition system 49
3.3.2 Description and calibration of transducers used to measure the GAIM process 50
3.4 Specific pressure integral as an indicator of process stability . . . 54
3.5 Tensile test specimen design and analysis 55
3.5.1 Form of the GAIM tensile test specimen 56
3.5.2 Wall thickness measurement using an image analysis technique 58
3.5.3 Gas bubble penetration 64
3.5.4 Specimen shrinkage 65
3.5.5 Specimen mass 65

3.6 Design of experiments 66
3.6.1 Fractional factorial orthogonal arrays 66
3.6.2 The L18(2^1x3^7) experimental array 67
3.6.3 Factor interactions and confounding 68
3.6.4 Main factor and interaction effects 69
3.7 Summary 75

4 Experimental results **76**

4.1 Introduction 76
4.2 Process control phenomenon 77
4.2.1 Temperature effects on melt delivery 78
4.2.2 Temperature effects on screw velocity 79
4.2.3 Off-line gas injection investigations 82
4.3 Experimental investigations on the tensile specimen 87
4.3.1 Differential wall thickness due to shear heating 87
4.3.2 Gas pressure effects on residual wall thickness 90
4.3.3 Gas pressure effects on specimen shrinkage 91
4.4 An empirical model to describe residual wall thickness 93
4.4.1 Parameters 94
4.4.2 Experimental array 94
4.4.3 Parameter settings 96
4.4.4 Constant parameter settings 99
4.4.5 Experimental data 102
4.4.6 The empirical prediction equation for wall thickness 116

4.5 Summary 118

5 Theory for the simulation of cavity filling 120

5.1 Introduction 120

5.2 Modelling the GAIM process physics 121

5.2.1 Conservation of mass 121

5.2.2 Conservation of momentum 123

5.2.3 Pseudo concentration method 125

5.3 Melt viscosity models for the Pseudo concentration method 126

5.3.1 Newtonian 128

5.3.2 Power law 128

5.3.3 Cross model for shear rate viscosity dependence 129

5.3.4 Williams-Landel-Ferry (WLF) temperature dependence . . 130

5.3.5 Cross-WLF model 132

5.4 Outline of the finite element implementation 133

5.4.1 Linear finite elements 133

5.4.2 Finite element equations 135

5.4.3 Time stepping and upwinding procedures 136

5.4.4 Numerical solution considerations 137

5.5 Simulation methodology 138

5.5.1 Domain meshing 138

5.5.2 Boundary conditions 140

5.5.3 Time stepping interval 140

5.6 Summary 141

6 Simulation results and comparison with experiment 143

6.1 Introduction 143

6.2 FE mesh and boundary conditions 144

6.2.1 Flow symmetry and wall boundaries 144

6.2.2 Mesh density 146

6.2.3 Half and full geometry models 151

6.3 Flow modelling implementation 152

6.3.1 Initial flow conditions 152

6.3.2 Exit flow 154

6.3.3 Methods for gas injection 156

6.3.4 Flow velocity profiles 161

6.3.5 Melt viscosity model 166

6.3.6 Thermal effects within the model 168

6.3.7 Time stepping 174

6.4 Comparison of simulation with experiment 175

6.4.1 Behaviour of the experimental models 175

6.4.2 Material shrinkage 180

6.4.3 Relationship between simulation and experimental settings 182

6.4.4 Simulated wall thickness 187

6.4.5 Simulated and experimental wall comparison 191

6.5 Summary 200

7 Discussion 203

7.1 Experimental issues 206

7.1.1 Choice of material 206
7.1.2 Temperature measurement 206
7.1.3 Material shrinkage 207
7.1.4 Gas delay time 208
7.1.5 Gas injection needle 209
7.2 Issues relating to simulation 210
7.2.1 Computational requirements 210
7.2.2 Wall temperature boundary condition 212
7.2.3 Extent of bubble penetration 213
7.2.4 Secondary penetration 213
7.3 Issues that relate to validation 214
7.3.1 Simulation and process variable settings 214
7.3.2 Comparison of wall thickness 215
7.3.3 The skin layer against the mould wall 216
7.3.4 Moving the validation through time 217
7.3.5 Shear heating of the melt 217

8 Summary and Conclusions **219**

8.1 Experimental conclusions 220
8.2 Simulation conclusions 221
8.3 Validation conclusions 222
8.4 Further work 223

To my wife Kate for her unwavering support and encouragement and to my family for their continued support.

Acknowledgements

The author would like to acknowledge Dr Peter Olley of the University of Bradford for his supervisory role throughout the course of the research. Also, for providing the simulation code used to generate the simulation results within this work.

Thanks also goes to Professor Phil Coates for his valuable direction and encouragement.

Mr Rob Spares provided the post processing application for the visualisation of the simulation results.

Thanks to the EPSRC for providing the funding for this research.

Acknowledgements go to the following people:- Andrew Dawson, Roy Dixon, Mark Fellows, Ron Harding, Ken Howell, Andrew Key, Bob Jowett, Charan Panesar, Colin Parminter, Alistair Wood, Mike Woodhead.

List of symbols

Symbol	*Usage*
$\dot{\gamma}$	shear rate
$\dot{\gamma_w}$	wall shear rate
δ	wall thickness
η	viscosity (dynamic)
η_0	zero shear rate viscosity
λ	characteristic relaxation time
ρ	density
σ	normal stress
σ_i	interfacial surface tension
τ	shear force
c	concentration
$\mathbf{f}$	body force vector
g	gravity
P	pressure
R_b	bubble radius
R_o	tube radius
t	time
Δt	time interval
T	temperature
T_g	glass transition temperature

Symbol	*Usage*
T_s	reference temperature
U	bubble velocity
u	velocity in x direction
v	velocity in y direction
$\mathbf{V}$	velocity vector
w	velocity in z direction

Chapter 1

Introduction

The gas assisted injection moulding (GAIM) process is an important development in the manufacturing of plastic products. GAIM is an enhancement of the conventional injection moulding process. The work presented within this thesis focuses on the evaluation of a finite element implementation of a pseudo-concentration method for the simulation of gas assisted injection moulding cavity filling. The simulation is evaluated against real specimens manufactured on an industrial scale machine. The feature of the specimens of particular interest is the residual wall thickness that remains once the gas bubble has penetrated the melt.

The thesis to be investigated is that a 3D finite element implementation of a pseudo-concentration method is a viable approach toward correctly predicting cavity filling. Comparisons with real process specimens are used to validate this claim.

Important issues relevant to the modelling and experimental investigation of the gas assist process are taken from the literature review chapter, which is chap-

ter 2. The current approach to modelling based upon approximations in the thickness direction are shown to be too simplistic for GAIM when compared with a full 3D model. Much of the validation work currently in the literature compares real products against results from commercial simulation packages, based on thickness approximations, commonly used by mould and product designers. The work done on 3D models has not generally been validated against the industrial scale process. This work aims to provide further justification and knowledge to the process physics of gas assist.

The experimental procedures used for specimen preparation and analysis are outlined in chapter 3. Along with the instrumentation placed on the equipment used to manufacture the specimens, which is important for linking the simulation control with the process conditions. The results of the specimen analysis and the developments of an empirical model to describe the residual wall thickness as a function of processing variable settings are presented in chapter 4.

The method used to model cavity filling is detailed in chapter 5. The pseudo concentration method is implemented into a 3D finite element application. The results of the simulation and a comparison with the experimental results derived in a previous chapter are presented in chapter 6.

The discussion and conclusions bring together the issues relevant to the simulation, experimental work and the validation procedure. An attempt is made to asses the validity of the simulation results and provide some direction for future work.

1.1 An overview of the Gas Assisted Injection Moulding process

Gas assisted injection moulding is a novel process that enhances conventional injection moulding. Fundamentally, GAIM utilises high pressure gas to form the molten polymer to the shape of the cavity and provide pressure during cooling.

It is common for the gas to be injected into a thick channel filled with melt in order to complete the cavity filling. The main stages of the cavity filling process are shown schematically in figure 1.1. Firstly, melt is injected into the mould in much the same way as the conventional injection moulding process. However, the cavity is not usually completely filled with the melt and can be as low as 60% full in some cases. Secondly, gas is injected well upstream of the melt flow front to force the melt to fill the cavity. Methods for injecting gas into the melt are varied and outlined in section 1.1.5.

The gas displaces melt in the centre of the section and leaves a residual thickness of melt against the mould wall. The thickness of the remaining melt is commonly termed *residual wall thickness* and will be termed as such throughout this thesis. The formation of the residual wall and it's correlation to process settings also forms the common thread throughout this work.

The sequence of GAIM process stages are shown in figure 1.2. Once the mould has closed melt is injected into the cavity by the reciprocating screw within the machine barrel, in the conventional manner. At some point within the screw stroke during melt injection an electronic trigger activates the gas assist controller

(a) Melt partially fills the cavity

(b) Melt filling stops and gas injection completes filling (primary gas penetration)

(c) Gas pressure is maintained during melt cooling and shrinkage (secondary penetration)

Figure 1.1: The main stages of GAIM for manufacturing hollow components.

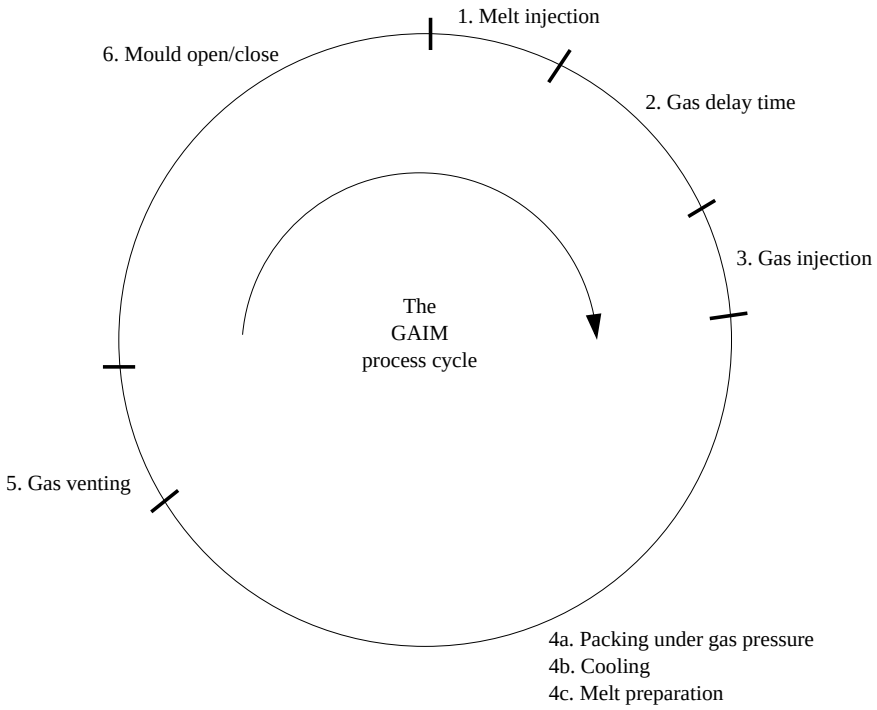

Figure 1.2: The typical GAIM process cycle [1]

to begin its sequence for gas injection. The first step in the gas injection sequence is a delay time between the trigger and the start of gas injection. The length of the delay time varies depending upon process needs, such as prevention of uncontrolled gas penetration. Section 1.1.3 outlines the process variables in more detail.

After the delay time gas is injected into the mould, usually to complete filling and provide packing pressure for the cooling stage. The control of gas is normally based upon a pressure delivery up to a specific time and the availability of up to 5 pressure-time profiles is not unusual. The first pressure-time phase is responsible for any completion of filling within the cavity and forming the residual wall; commonly termed primary gas penetration. Subsequent stages of gas pressure

are used to compensate for melt shrinkage during cooling and solidification. Melt shrinkage occurs from the inside, which preserves melt contacting the mould wall and therefore a faithful shape. During the cooling stage the reciprocating screw is preparing a charge of melt for the next cycle.

Once cooling is complete the gas is vented from the cavity to drop the pressure to ambient. Clearly a pressurised component would deform severely once the mould was opened if gas pressure was not released. The mould then opens, the product is ejected, the mould closes and the process start again with melt injection.

1.1.1 Process advantages and implementation issues

1.1.1.1 Cavity pressure

The GAIM process enhances the conventional injection moulding process to realise process cost savings and extended scope in product design. The basis for the process advantage is the relatively low pressure used to fill and pack the product. Figure 1.3 illustrates the difference in pressure profile between conventional and gas assisted injection moulding.

The pressure through polymer melt rises along the upstream flow path away from the melt front. The pressure required at the gate to drive the melt into filling the cavity and subsequent holding during cooling is significant. Pressures of 1800 bar are common for cup sized mouldings, for example.

The pressure throughout the gas assisted component is more uniform in the region of the gas bubble. The low viscosity of the gas results in an insignificant

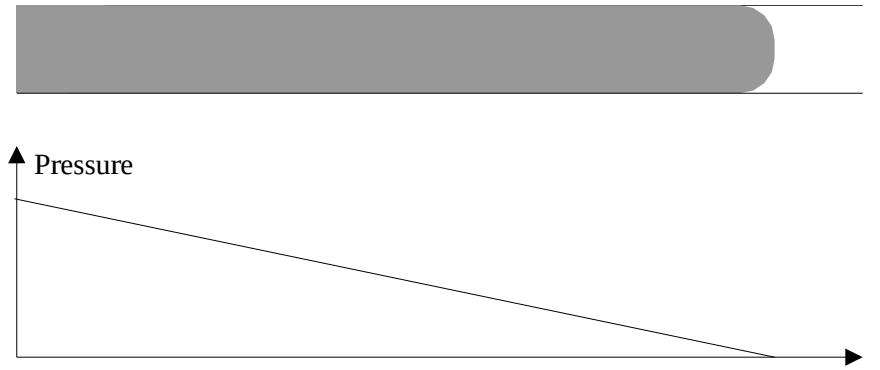

(a) Conventional injection moulding

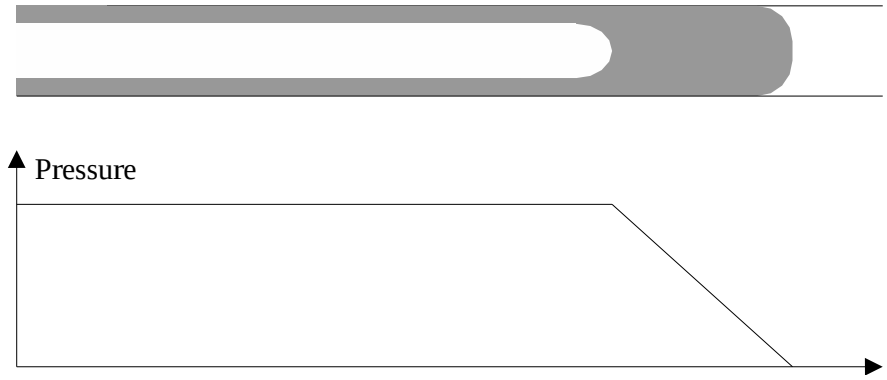

(b) Gas Assisted Injection Moulding

Figure 1.3: Internal pressure profile in conventional and gas assisted injection moulding [2, 1].

pressure gradient through the gas bubble from the source to the bubble tip. Also, a thick section gas channel presents low resistance to flow compared to a thin wall commonly associated with conventional injection moulding.

The result of the gas assist mechanism is an even distribution of pressure within the product. The gas line pressure is available upto the point where the gas bubble ends within the product. Also, the residual stress within the melt, caused by high pressure and shear gradients, is reduced and product warpage after ejection from the mould is reduced.

The gas used is usually inert and nitrogen is a popular choice. The reason for the inert nature of the gas is to avoid oxidisation of the melt while under pressure. Compressed air may cause such problems.

1.1.1.2 Cost implications

Since the melt thickness is relatively low in channels cored out with gas the cooling time is kept to a minimum. The cooling time in the injection moulding cycle is by far the biggest portion of the overall cycle time. Saving made here have cost benefits by increasing production rates. The quantity of melt can also be reduced, which realises a material cost saving.

A major strategic consideration for machine procurement is the size of the clamp force and the melt delivery capability. The relatively low pressure of GAIM allows relatively large moulds with significant projected areas to be filled on machines with clamp forces lower than required for the conventional process. The saving on machine capital cost is significant.

Figure 1.4: A car door handle is a common example of a thick sectioned component that employs gas to core-out a large fraction of the section.

However, additional machinery needs to be purchased to provide and control the gas. Industrial operations often find nitrogen generation units to be more cost effective than buying bottles gas. An initial outlay is required and justifiable confidence in continued gas assisted moulding.

1.1.2 Typical GAIM applications

The product geometries that most commonly use GAIM fall into two categories. These are thick sectioned only and ribbed plaque. An example from each category is shown in figures 1.4 and 1.5.

The thick sectioned only component shown in figure 1.4 is a car door handle. This section in the middle of the handle is approximately 20x20mm, which could not feasibly be considered for the conventional injection moulding process. The

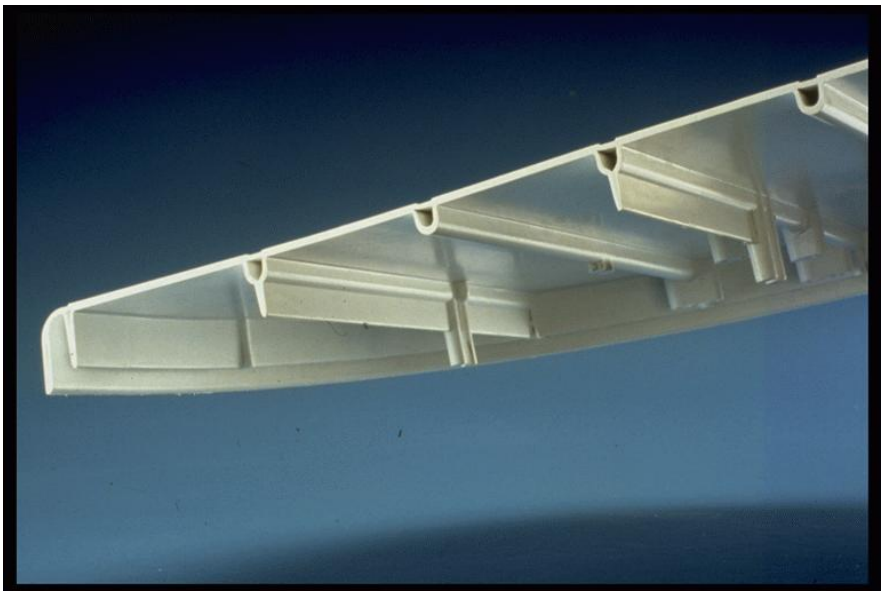

Figure 1.5: Strengthening ribs on a flat panel formed with GAIM.

mould is part filled with melt before gas is injected through a needle near the melt gate.

The car door handle would have been manufactured in two halves if the conventional injection moulding process was used. This requires a post operative assembly that requires resourcing.

Strengthening ribs placed on flat sections, such as table tops, are restricted in section when the conventional injection moulding process is used. The example of ribs that can be designed for gas assist shown in figure 1.5 are significantly greater in section. The stiffness derived from such ribs is much improved and the sink marks normally evident on the opposite surface from the ribs are greatly reduced.

Other examples commonly encountered are car door handles, coat hangers, kettle handles, car bumpers and television housings.

1.1.3 Process features and mould design issues

The conventional rules governing mould design are not generally applicable to the design of moulds for gas assist. For instance the design of strengthening ribs require a gas channel to be of significant section compared to the adjoining flat surface. The conventional rules would attempt to minimise the section while still providing stiffness. Design guidelines are available from a number of sources, such as conference proceedings [3], material suppliers [4] and machinery manufacturers [5].

The ability to simulate mould filling with software such as Moldflow MPI provides opportunity to save considerable expense in the tool design and commissioning stages. However, the softwares have traditionally been used for the conventional process of injection moulding and modules have subsequently been added to provide solutions to variation processes such as GAIM. This has presented a problem since the approximations that are valid for the conventional product geometries are over simplifications for the thicker sectioned GAIM product. As such the mould filling simulation capability is not so readily available.

Additional processing parameters require consideration over and above those relating to the conventional injection moulding process. The conventional process relies upon process settings for melt temperature, plastication, injection velocity, packing pressure and cooling time. The GAIM process considers the same variables, possibly with the exception of packing pressure, but also adds gas delay time, gas injection pressure, gas packing pressure and gas venting time [6].

The additional processing parameters require new skills for process setting

personnel and further process understanding. This extends to the engineers that design the moulds and the part designers that are traditionally more artistically trained.

1.1.4 Related processes

The addition of a second fluid to polymer melt can be found in a number of other processes. Indeed nitrogen gas can be used in other ways to provide pressure to the melt. External gas moulding (EGM) (trade name of Battenfeld Airmould contour) purposely injects gas between the mould wall and the melt purely to compensate for melt shrinkage during cooling. A popular application is to place the gas between solid strengthening ribs to improve the sink on the opposite cosmetic surface. EGM brings added mould complexity since the mould needs to be made gas tight in the appropriate areas, but also vented correctly [7].

Koolgas complements GAIM by cooling the nitrogen, using a vessel of liquid nitrogen, en route to the mould. Cycle times can be reduced by significantly reducing the cooling time. The product ejection temperature is reached quicker using Koolgas [8].

Supercritical fluids offer another route to addressing the issue of excessive shrinkage and cooling time for thick sectioned components. The process involves the dissolving of carbon-dioxide or nitrogen into the melt while inside the machine barrel. The screw inside the machine barrel has a length to diameter ratio of 27 (L/D 22 is normal) to provide a homogenous mixture ready for injection into the mould. Once the melt is injected the carbon-dioxide precipitates out of solution

to form gas bubbles, particularly within the thicker sections where the melt is hot for an extended period of time. The gas bubbles provide sufficient pressure to compensate for the volume reduction associated with melt shrinkage. An additional process advantage of supercritical fluid technology is that the viscosity of the melt is reduced, which assists flow into the mould [7].

Water is also used to form hollow sections. The technology in a commercial form is quite new, but is already demonstrating significant scope for product manufacture. The advantages of using water over gas are that the cooling times of the melt can be dramatically reduced due to the high heat conductivity of the water over the gas. Also, much larger sections with smaller wall thicknesses can be formed. The process does bring with it issues such as the handling of the water, which is more difficult than gas. Also, the process knowledge required is in its infancy [7, 9].

1.1.5 Methods for injecting gas

A number of methods exist for injecting gas into the polymer melt. The methods of delivery are designed to position the start of the gas bubble inside the flow of the melt to form a core. Other methods used in external gas moulding will not be covered. The methods for injecting gas differ mainly in where along the melt flow path the gas is delivered.

The furthest possible point upstream in the melt flow that gas can currently be delivered is at the machine nozzle. Figure 1.6 shows a gas injection nozzle fitted to the end of a machine barrel. This specifically designed nozzle accepts

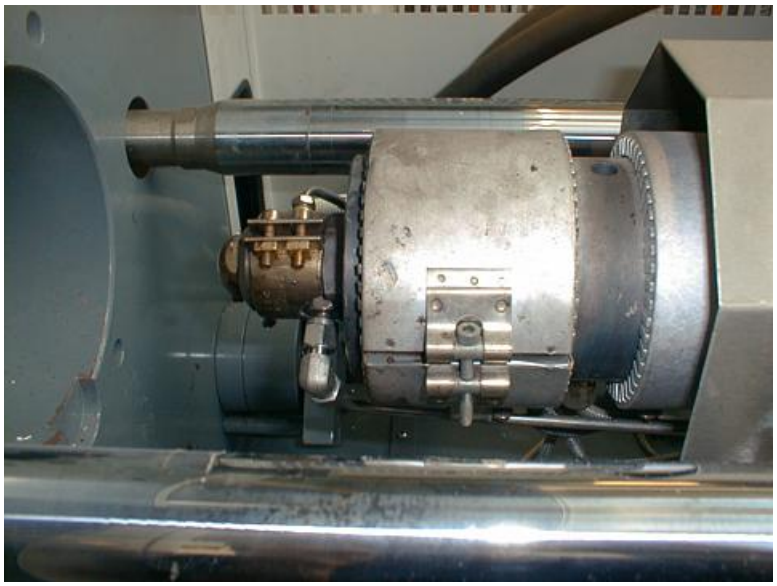

Figure 1.6: Specially designed gas nozzle fitted to the machine barrel

a line for gas delivery, which is channelled through an intricate fitting inside the body to deliver the gas into the centre of melt flow. The intricate fitting allows melt to flow around the outside of the gas injector.

An important feature of the gas nozzle is the non-return valve in the form of a seated ball bearing between the main barrel and the gas injector. Gas is prevented from entering the machine barrel by the valve. The consequence of gas entering the barrel is high pressure gas blowing back through the hopper. A similar valve is located inside the intricate fitting to prevent melt from entering the gas feed line.

Tool modifications or complexity can be reduced by injecting gas from the nozzle and mould change over time is kept down since gas connections to the mould are not necessary. However, the nozzle gas delivery cannot be used with hot runner systems containing melt for the next cycle because variation in shot

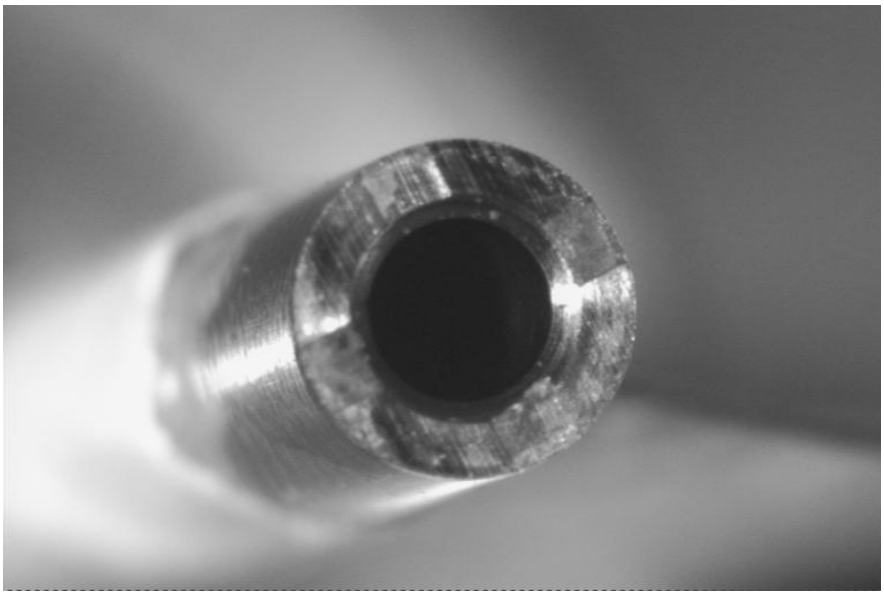

Figure 1.7: A microscope view of the top of the gas needle.

weight and air traps are induced.

An alternative to nozzle gas delivery is offered by the gas injection needle that places the gas either in the runner system (not hot runner) or the component itself. An advantage here is that gas can be delivered to very specific regions of the product and multiple cavities can each have a needle independently controlled.

A gas needle supplied by Battenfeld that protrudes into the melt is shown, in part, in figure 1.7. The top surface of the main needle body is shown through which a flat sided pin passes and screws into part of the body. The central pin is flat headed to the diameter of the pin (3mm) and the head sits on the top surface shown. Gas is supplied to the pin and passes up past the flat sided central pin and into the melt underneath the head of the central pin. The top of the pin body is grooved (as shown in figure 1.7) to allow the gas to pass into the melt, but the grooves are small enough to prevent melt from blocking the needle. The

central pin can be removed easily while the pin is in-situ to allow cleaning and the removal of blockages.

1.2 Modelling cavity filling

The modelling of cavity filling is a vehicle for concurrent engineering by taking process knowledge upstream within product development. The process dynamics contained within a process model are utilised by part and tool designers to optimise the manufacturing step and avoid problems with the product that may require expensive reworking of the mould.

1.2.1 $2\frac{1}{2}$D and 3D results

Commercially available software for modelling conventional injection moulding cavity filling has proved successful. The conventional process typically applies to thin walled components where the flow length is significantly greater than the flow thickness. The Hele-Shaw approximation is used to exploit the high flow length to thickness ratio and significantly reduce computational requirements.

The models based upon flow thickness approximations (so called $2\frac{1}{2}$D) do not provide flow information in the thickness direction. Therefore bubble formation in GAIM is not a fully described geometry. Commercial software has an additional module to solve the gas assisted problem. The results of an analysis are summarised for each element to provide a single number that relates to a fraction of melt within the element. Figure 1.8 is a typical result from a model based upon $2\frac{1}{2}$D implementation. The distribution of the melt and the gas bubble cannot be

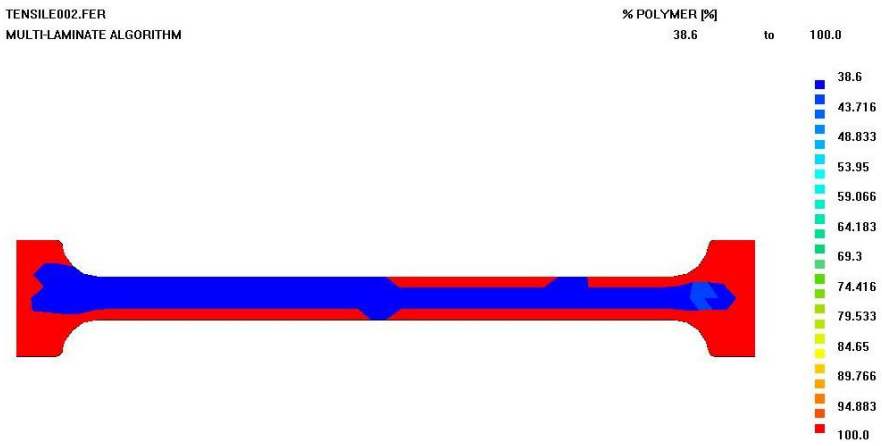

Figure 1.8: A typical GAIM result from $2\frac{1}{2}$D based applications

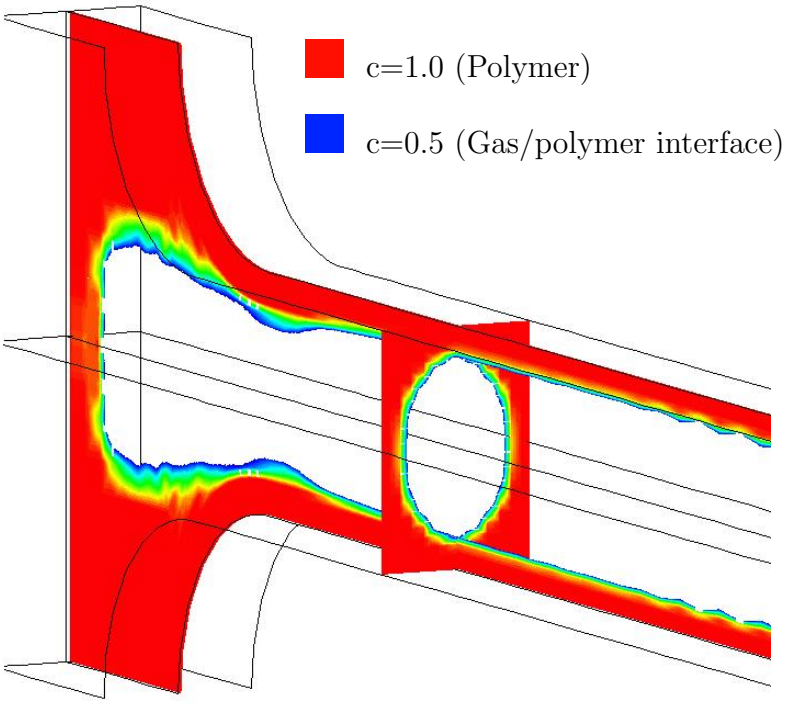

Figure 1.9: A typical GAIM result from a 3D application

determined from this, but an indication is given as to the extent of the bubble penetration.

A typical 3D result, from the modelling implementation used within this thesis, is shown in figure 1.9. The view is presented such that only polymer is shown as a contour and gas is appears as a hole within the flow. The melt and bubble formation across the cavity section and along the length of the section along the centreline is shown. Clearly the form of the bubble is fully described with a 3D model.

1.2.2 A simple tube model

To illustrate the dynamics involved in the volumetric displacement of one fluid with another a very simple volume dispersion model is presented here. This model assumes that the penetrating fluid displaces from the centre of flow.

The extent of bubble penetration into the cavity depends heavily on the melt fraction remaining after the bubble front has passed. To illustrate this point a simple model based upon volumetric displacement within a tube is used. Equation 1.1 is developed from considering a fixed volume cylindrical cavity containing melt to a volume fraction of Km penetrated by a flat ended bubble.

$$\frac{l}{L} = \frac{1}{d^2}(1 - Km) \tag{1.1}$$

where,

$$d = \frac{r_b}{R} \tag{1.2}$$

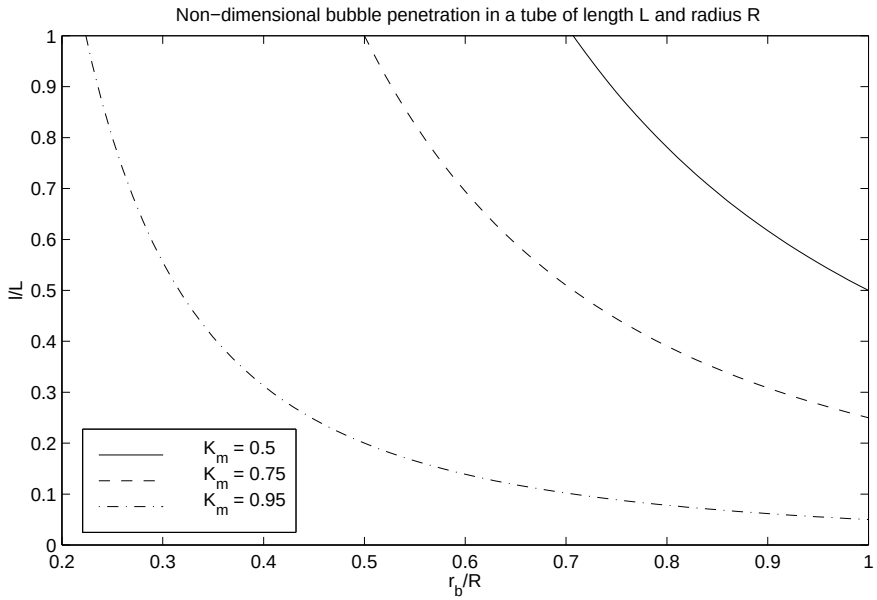

Figure 1.10: Relationship between bubble penetration (l/L) and melt fraction over the section (r_b/R) in a simple tube model.

where l is the bubble length, L is the cavity length, Km is the melt volume as a fraction of the cavity volume, r_b is the bubble radius and R is the cavity radius.

The behaviour of the simple tube model is shown in figure 1.10, where the penetration of the bubble (l/L) is governed by the melt fraction (r_b/R). The model is tested for a range of volume fractions (Km). For relatively small changes in the melt fraction, left by the advancing bubble front, the penetration length is significantly influenced.

The mechanisms that govern bubble formation in the GAIM process are more complex than a simple volume displacement model. For instance, cooling of the melt before gas injection (delay time) will be shown to have a very significant contribution toward wall thickness. The simple model does, however, demonstrate the importance of achieving an accurate prediction of the bubble shape, in

particular melt fraction, over the cross section before any attempt can be made to accurately predict the extent of bubble penetration.

This simple model is just based on volume displacement with a prescribed format for the displacement. This allows an idea of the process dynamics to be introduced readily. A more general geometry with no prescribed format for penetration requires a more sophisticated model that is based on the physics of the process. It has already been pointed out that an approach to modelling that employs a thickness approximation will not yield the necessary information regarding the true bubble geometry.

A 3D implementation of a model is clearly necessary in order to capture the bubble geometry correctly. The process physics that feature significant melt flow in 3D, particularly due to the low aspect ratio of the section dimensions exhibited in thick sectioned gas channels.

1.2.3 The pseudo-concentration method

In order to model a two phase flow, which is the presence of two immiscible fluids within the same domain, some method of separating the fluids is necessary; the pseudo-concentration method is useful for just this application. The method utilises a labelling system for the fluid. The implementation used here is based on a finite element method, so the fluid label is a degree of freedom at a node that describes an element.

The concentration labels, for simplicity, are chosen to be over the range 0 to 1 and are linked to gas and polymer respectively. The boundary that separates the

melt and gas in the real system is very definite. However, the boundary described by the pseudo-concentration method is a gradient that changes from 1 to 0 as the fluid changes from polymer to gas respectively. The absolute boundary is therefore taken at the contour of 0.5 concentration. The position of the boundary contour is usually interpolated from the concentration values at the element nodes.

The melt, at a concentration of 1, is described as a polymer in that its viscosity is determined from a rheological model; the viscosity depends on temperature and shear rate. The gas on the other hand, at a concentration of 0, is considered to be a ficticious fluid with a viscosity that is a number of orders of magnitude lower than the melt viscosity. The viscosity of the ficticious fluid is not representative of gas, which characteristically has a viscosity on the order of 10^{-5}Pas [10]. For numerical reasons the gas is made more viscous than the real fluid.

The finite element implementation of the pseudo-concentration method is covered in more detail in chapter 5.

1.3 Experimental facility

The manufacturing facility available for GAIM products provides the scope to follow an experimental programme in order to validate simulation results. A tensile test specimen mould is available for validation purposes, which is rectangular in section over a gauge length of 200mm.

The machine used for GAIM is a Battenfeld CDK750, which is commonly found within industry. The machine is in two distinct parts, an injection moulding

Figure 1.11: The Battenfeld CDK750 with Airmould

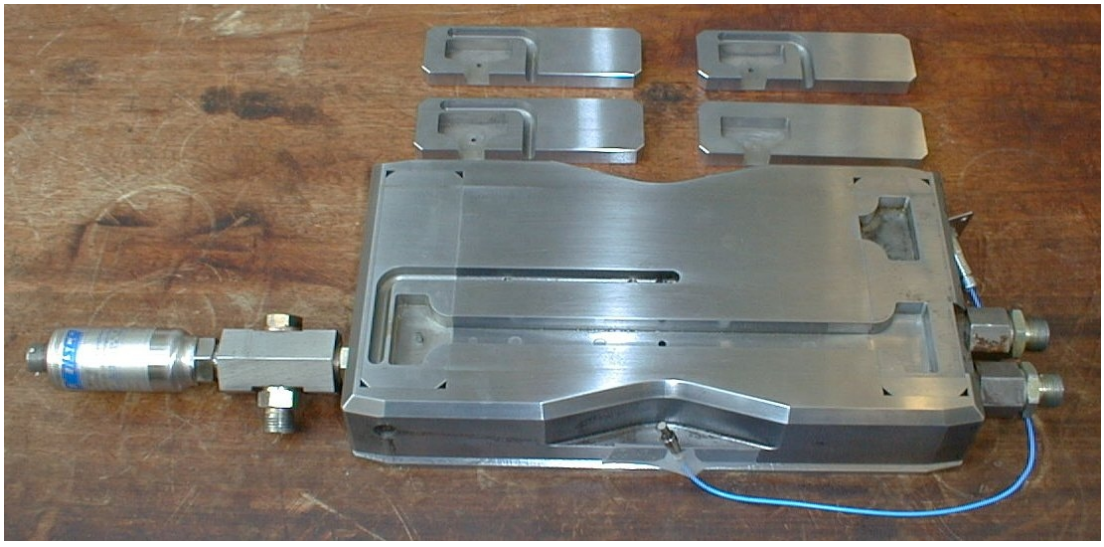

Figure 1.12: The tensile test specimen mould

machine and a gas assist module. The injection moulding machine has a 75 tonne clamp force and is equipped with a robot to handle the moulded specimens. The Battenfeld machine is shown in figure 1.11, where the robot is mounted on top of the fixed mould platen, the Airmould gas supply unit and controller is attached to the far end of the injection moulding machine.

The mould for specimen production is shown in figure 1.12. The form of the tensile specimen is clearly cut from the steel; the gas injection needle protrudes up into the cavity within the left hand tab; a runner system feeds melt from the centre of the cassette to one end of the specimen; gas is injected into a manifold where a pressure transducer is also mounted to measure the line pressure.

Chapter 2

Literature review

2.1 Introduction

The fundamental principle of a low viscosity fluid penetrating a higher viscosity fluid has been investigated for over 65 years. The fluids of interest have varied from Newtonian oils displaced by air to higher viscosity non-Newtonian fluids like polymer melts displaced by high pressure nitrogen gas. Applications for the principle of gas penetration include oil extraction from porous rock and the manufacture of catalytic converters found in automobile exhaust systems.

The application of interest here is the application of high pressure gas to penetrate non-Newtonian fluid. The effects of temperature and the penetration rate are of particular interest since they are significant processing factors in GAIM. An outline of the bubble penetration characteristics found with a number of different fluids is outlined in the first part of this chapter. The effect of cross sectional geometry is also discussed, but this is related to the oil extraction applications

since research within the GAIM field is limited here.

Particle tracking velocimetry has made possible advanced experimental observations on the bubble tip during gas penetration. This type of experimental technique provides flow field information valuable for model validation. Combining particle tracking velocimetry with mould filling visualisation adds further possibilities for validating the theory driving cavity filling predictions.

An added dimension to the physics governing gas penetration in GAIM is the process variability, which is generally not considered in the modelling phase. Studies have shown that cavity geometry is a significant factor in the robustness of the final product to changes in the process due to noise. Noise is typically viewed as a variation in factors that are beyond process control. An example would be temperature variations in the melt. Since noise will always exist in some form and at some level, the product should not be sensitive to the noise - this is termed robustness. The idea of a moulding window diagram (or mould-ability diagram) is described and results from other researchers are shown.

2.2 Investigations into the GAIM process

2.2.1 Bubble penetration studies

The phenomenom of a viscous fluid displaced by a significantly less viscous fluid (gas) has been of interest for many years, certainly since Fairbrother and Stubbs carried out their experiments in 1935, taken from Taylor [11]. This area of research was initially undertaken to investigate enhanced oil reclamation methods,

$Ca = \frac{U\eta}{\sigma_i}$	Capillary number	Surface tension relative to viscous forces
$Bo = \frac{\rho g R_o^2}{\sigma_i}$	Bond number	$\frac{Bo}{Ca}$ is gravity relative to viscous forces
$Re = \frac{\rho U R_o}{\eta}$	Reynolds number	Inertia forces relative to viscous forces
$De = \lambda\dot{\gamma}_w$	Deborah number	Ratio of material to process time scale
$\lambda = \frac{\sigma\dot{\gamma}_w}{2\eta}$		Characteristic relaxation time

Table 2.1: Dimensionless numbers characteristic of gas bubble penetration through a viscous fluid in a tube of radius R_o [12]

and later the coating of monoliths in catalytic converters. Fairbrother and Stubbs related the remaining fraction of liquid to the relative speed between the bubble and liquid fronts. The non-dimensional groups shown in table 2.1 are suggested to characterise a long gas bubble penetrating a liquid [12].

Capillary number (Ca) describes the relative importance between viscous and interfacial forces during gas penetration. U is the bubble front velocity, μ is the viscosity of the liquid and σ_i is the interfacial tension between the gas and liquid. The capillary number, therefore tends to increase with increasing bubble velocity.

Reynolds number (Re) indicates the relative importance between fluid inertia and viscosity. Similarly, the ratio between Bond (Bo) and capillary numbers indicate the importance of gravity in determining flow characteristics. In all cases the fluid viscosity is generally dominant so inertia and gravity can be disregarded.

The Deborah number (De) is only applicable to viscoelastic fluids in this context. Here the response of the fluid to extensional shear is considered against the characteristic process extension rates.

It is important to note the different terminologies used to describe the fraction of fluid remaining against a vessel wall. A convenient measure of the residual fluid is the quantity remaining as a fraction of the total cross section and is often referred to as m. Another common measurement is thickness ratio, where the wall thickness, δ is given as a fraction of a centreline to wall dimension. For example, the thickness ratio in a tube of radius, R is δ/R.

2.2.1.1 Newtonian behaviour

Fairbrother and Stubbs work was carried out at low rates of gas penetration (Ca<0.09). Taylor [11] showed the relationship derived by Fairbrother and Stubbs was only accurate at these low capillary numbers, were interfacial tension is more significant in forming the bubble tip shape. Taylor showed, using glycerine and golden syrup, that the fraction of fluid left behind in a tube after gas penetration increases with increasing capillary number, to an asymptotic value of $m = 0.56$ ($\delta/R = 0.34$). The highest capillary number Taylor operated at was 2.0, but he believed a higher value would increase the residual fraction of fluid still further.

Cox (1962) [13] increased the maximum capillary number to in excess of 10, again using golden syrup as the viscous fluid and carbon tetrachloride as the driving fluid. At 20°C the viscosity ratio between the fluids is $4\text{x}10^4$. Cox found that the fluid fraction approached an asymptotic value of 0.6 ($\delta/R = 0.37$). This confirmed Taylors prediction that higher capillary number would result in a higher asymptotic value than those measured.

The use of a tube for gas bubble penetration studies was found to be im-

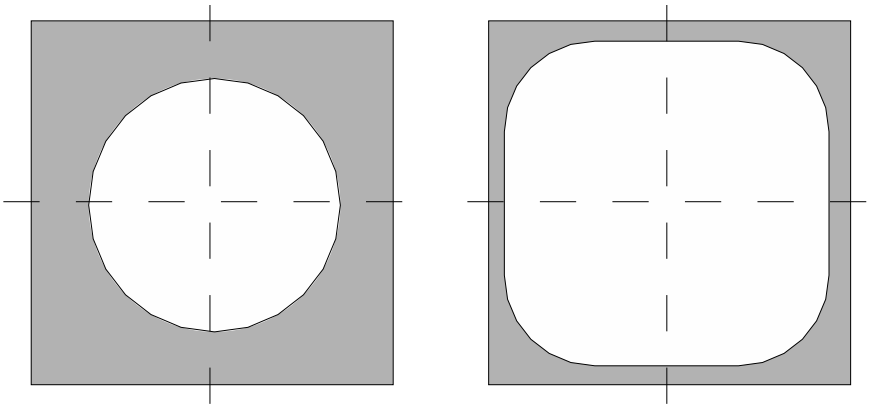

(a) (b)

Figure 2.1: Schematic of the fluid interface in (a) axisymmetric bubble (b) non-axisymmetric bubble (from Kolb, [14])

practicable for oil recovery research. A square capillary of 2mm section was used by Kolb and Cerro [14] to more closely simulate the capillary shape in rocks containing oil. The specimen cross section used in this thesis is rectangular.

The bubble shape within the square capillary changed dramatically depending upon the capillary number. Figure 2.1 shows an axisymmetric and non-axisymmetric bubble shape, which are associated with high and low capillary numbers respectively. The fraction of fluid remaining increases with increasing capillary number.

The transition in bubble shape between axisymmetric and non-axisymmetric occurred at a capillary number of 0.1. It was seen that the fraction of fluid remaining approached an asymptotic value of 0.64, which is higher than the value of 0.60 found with circular sections. Clearly, the corners of the section tend to "collect" the fluid and this effect is also seen using polymer melts in GAIM.

2.2.1.2 Shear thinning and temperature effects on wall thickness

More recently, Poslinski et. al [15, 16] investigated the bubble penetration mechanism with particular attention to GAIM. Experiments were carried out at room temperature with shear thinning viscoelastic silicone liquids. Capillary numbers were 10^3, which is typical in the cavity filling stage of GAIM. It was found that wall thickness ratio tended toward an asymptotic value of 0.35, which is observed with Newtonian fluids. However, at low Ca the viscoelastic coating tended to be thinner than the Newtonian counterpart. The shear thinning behaviour tends to modify the curve of capillary number against thickness ratio, but the asymptotic value here is approximately 0.35.

Koelling et. al. [12] have also used shear thinning fluids and report a more dramatic reduction in fractional coverage than Poslinski. Injection moulding experiments using polystyrene and polycarbonate materials confirm this trend. However, a comparison of the rheological data for the shear thinning fluids used by Poslinski and Koelling shows significant differences. The fluid used by Poslinski shear thins at very low shear rate and is approaching an asymptotic viscosity at $\dot{\gamma} \approx 10s^{-1}$. The fluid used by Koelling is starting to shear thin at $\dot{\gamma} \approx 10s^{-1}$ and does not reach an asymptotic value within the range published, which is $\dot{\gamma} \approx 200s^{-1}$. It is feasible, therefore, to explain the apparent disagreement in fractional coverage results in terms of material rheology. The fluid used by Poslinski is reaching Newtonian behaviour at low Ca. The fluid used by Koelling is still well within the shear thinning region over the respective capillary number range.

The experiments carried out on processing machinery by Koelling et. al. [17] using polystyrene and polycarbonate materials have shown a connection between material rheology and fractional coverage. Both materials are shear thinning, but polycarbonate, compared with polystyrene, has a significantly extended Newtonian region before the onset of shear thinning. Results are published showing fractional coverage against flow length through the mould. In the case of polystyrene, which readily shear thins, the fractional coverage reduces with increasing gas pressure. However, polycarbonate material does not show any change in fractional coverage with increasing gas pressure until near the end of penetration where the bubble accelerates significantly and the shear rate is high enough for the material to shear thin.

Poslinski combined the results gained from the gas penetration studies with a one dimensional cooling analysis. Not surprisingly, the frozen layer of polymer melt that forms due to contact with the mould wall increases in thickness over time. However, for cooling times less than 10 seconds at least 80% of the melt remained within 10°C of the core temperature. The highest temperature gradient was at the wall throughout the frozen layer. Therefore, within the typical GAIM processing ranges the majority of the residual wall thickness can be attributed to the molten polymer, which is predominantly governed by the gas penetration rate. Any increase in thickness ratio is due to the fluid fraction deposited on top of the frozen layer.

2.2.1.3 Viscoelastic effects on bubble front shape

The first Particle Tracking Velocimetry (PTV) study of a long bubble penetrating a viscoelastic fluid in a capillary tube was carried out by Gauri and Koelling [18]. Here the viscoelastic effect on the bubble front shape during penetration is of particular interest. The fluid was seeded with particles that illuminate under a sheet of laser light. The bubble is filmed using a traversing camera and the film is analysed frame-by-frame to determine individual particle velocities and hence fluid velocity. Analysis of PTV data provides information about the bubble penetration velocity, the fluid velocity field around the bubble tip, extension and shear rates in the bubble vicinity.

An ideal elastic fluid, called a Boger fluid, which does not shear thin was used. At low bubble velocities ($Ca<1.7$) the fractional coverage is close to that of Newtonian fluids. The fractional coverage observed using Boger fluid deviates from the Newtonian results at higher bubble velocities, where extensional shear rates are becoming significant. The asymptotic value of fractional coverage found at $Ca\approx10$ is around 0.60 and 0.65 for Newtonian and Boger fluids respectively. Therefore extensionally thickening Boger fluids tend to reduce the penetrating bubble radius and increase the fractional coverage. In fact, Gauri shows that the fractional coverage results for Boger and Newtonian fluid diverge at a Deborah number of 1, when elastic effects become significant.

2.2.2 Cavity filling observations of ribbed plaque moulds

The observation of cavity filling can indicate the mechanism by which certain phenomena occur. Moulds with glass windows provide an excellent solution and allow the whole cycle to be recorded for later analysis.

2.2.2.1 The path of least resistance

It is generally recognised that the gas bubble will penetrate through the molten polymer along the path of least resistance. Yang [19] shows this with a stepped plaque were the melt flow and gas bubble travel from a thick to thin section. At the step the gas bubble expands in a direction along the step since the resistance to flow in the forward direction (the thin section) is temporarily greater.

Yang [20] calculated the flow leading effect of thicker rib sections, as shown in equation 2.1,

$$\frac{R_{rib}}{R_{cavity}} = \frac{H_{cavity}^3}{H_{rib}^3 S} \tag{2.1}$$

where, R is the resistance to flow, H is the cavity thickness and S is a shape factor related to the size of the rib compared to the cavity. By inspection, if the rib thickness (H_{rib}) is double that of the cavity (H_{cavity}) then the resistance to flow in the rib is $\frac{1}{8}$ that of the cavity.

2.2.2.2 Uneven filling

Experiments conducted on multiple rib moulds by Yang and Wang [19, 21] have shown that gas bubble penetration is not even. A ribbed plaque cavity, shown schematically in figure 2.2, fills the first two transverse ribs (nearest the melt

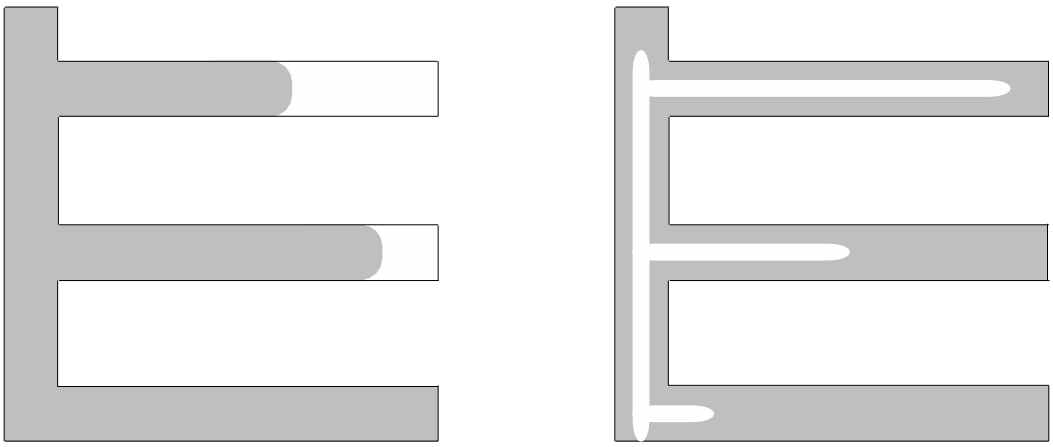

(a) Before gas injection

(b) After gas injection

Figure 2.2: Multiple ribs that split the flow of gas exhibit uneven bubble penetration. The rib furthest from the polymer gate fills the least with melt allowing for higher gas penetration. (Figure adapted from Yang [19].)

injection gate) and partially fills the last rib. If rib sections are too big compared with the thin walled sections then the melt front in the ribs can lead that in the thin sections excessively. This can result in air traps within the thin sections and gas fingering. The gas penetrates further into the rib furthest away from the gate because this has the most free space at the end of polymer injection. The cavity used by Wang typically showed a 20% greater penetration into the ribs furthest away from the gates compared with those nearest the gates.

Investigations that correlate process settings to the penetration of gas into multiple ribs were conducted by Zhao [22]. Ideally, the final product should show maximum gas penetration without any fingering into the thin walled sections. Over the process setting ranges available the melt delivery (lowest is best) and delay time (highest is best) were found to have the greatest effects.

2.2.2.3 Splitting the gas bubble flow

Splitting of the gas bubble penetration along different channels is not easy to control. The gas bubble flow has been found to be unstable in symmetrical cavities even if the melt flow before gas injection is symmetrical. Yang [19] used a double rib cavity with an adjoining rib into which gas was injected to investigate this phenomenon. The final position of the gas bubble was not symmetrical along each rib, yet the melt front location was symmetrical immediately before the injection of gas. Yang stated that once a gas bubble started to lead there was no self restoring mechanism, therefore the system is unstable.

Bifurcation is the splitting and then rejoining of the melt flow, typically around a boss or other cut-out within the component. The melt flows either side around the boss and rejoins at the other side. When the gas is injected the bubble flow splits to either side of the boss, but typically does not rejoin on the other side. One flow path is dominant and continues along the channel past the boss, but the other flow path stops before reaching the other side of the boss. Lui [23] conducted experiments on bifurcation to show the effect processing conditions and polymer gate location had on the stability of flow. Fundamentally, once the flow has been split it will never recombine to form a continuous cavity around the obstacle. However, Liu shows that stability of flow could be influenced by a combination of mould design and processing conditions. Liu defines stability as the consistency by which the gas flow favours one branch of the bifurcation to the other over repeated cycles. It was found that placing the melt injection gate on one side of the cavity instead of centrally at the end of the mould provides more

consistency in which branch of the bifurcation the gas penetrates; that is better stability. The reason for the greater consistency is that the side gate promotes melt to flow further in one branch of the bifurcation that the other. The pressure gradient, from the centrally located gas needle, is greater to the melt front that has travelled less distance around the bifurcation and therefore the gas bubble favours that route as the path of least resistance. Other processing conditions are cited to improve stability, which are decreased mould and melt temperature, increased gas pressure and extended delay time.

2.2.3 Determining significant product characteristics and process variables

The GAIM process is more complex than simply gas bubble penetration through a fluid. Studies have been outlined in section 2.2.1 have shown that thermal effects on melt rheology are significant. A number of processing variables influence thermal history and gas bubble penetration characteristics. In order to understand GAIM process control a quantitative relationship is necessary between product characteristics and process variable settings.

A popular method available to investigate process variables is statistical design of experiments. Any number of responses from the product or process can be used as quality characteristics. Yang et .al. [24, 25] used the depth of sink marks on product as the quality characteristic and correlated this with the following process variables:- melt temperature; gas pressure; melt injection velocity; hold pressure; melt delivery; gas delay time. Melt temperature and melt delivery were found to

have the most effect on the depth of sink marks.

Similarly, Kapilla [26] used the length of bubble penetration into the melt as a quality characteristic. High and low viscosity materials, some glass filled, were used. Melt temperature and melt delivery were the most influential processing variables in bubble penetration in all cases.

2.2.4 Dealing with process variation

In any process there will be variation in product as a result of variations from process variables. In the case of GAIM, variations in melt temperature, mould temperature, melt quantity and raw material properties will influence the variability seen in the product. The sensitivity of product quality characteristics to these variations is a measure of process robustness.

2.2.4.1 Moulding window diagrams

A mould-ability diagram, or moulding window, is useful for showing the limits of process settings. Figure 2.3 shows a moulding window that is typical for the GAIM process. In this case the component was a ribbed plaque, where the gas channel formed the base of the rib. Here, injection stroke, which represents the quantity of melt delivered into the mould, is plotted against gas pressure. The upper and lower limits of each variable form a boundary inside which an acceptable component is produced. With respect to figure 2.3, if the gas pressure is too low the melt will not fill the entire cavity. Conversely, if the gas pressure is too high gas will push into the thin section of the component where rigidity

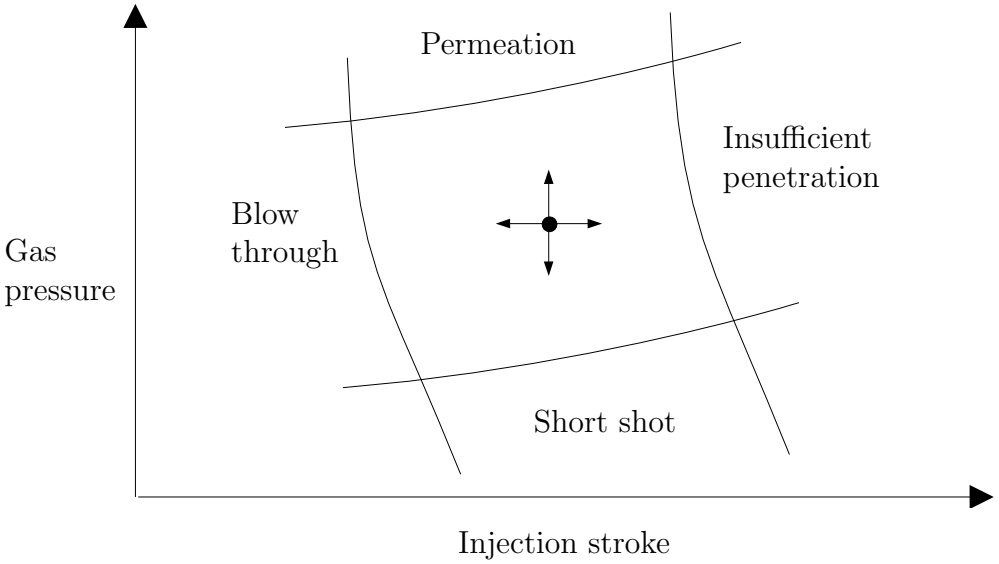

Figure 2.3: The moulding window plot clearly shows the region bound by upper and lower limits of two processing parameters that will produce an acceptable component. Taken from Chen [27].

is adversely affected - this is called gas permeation or fingering. Similarly, if the initial melt delivery is too high then insufficient volume remains within the cavity for gas to penetrate. Conversely, if melt delivery is too low then gas will blow out of the melt before the end of the cavity is reached.

Ideally, the moulding window is as big as possible to allow for variations in processing parameters from set point. Cavity geometry is an important factor in the robustness and mould-ability of a product. Tool design rules that apply to conventional injection moulding do not apply to GAIM.

2.2.4.2 Effect of strengthening rib design on mould-ability

Chen et. al. [27] has tested rib geometries that provide rigidity to an otherwise flat structure. The ribs also behave as a flow leader to control the path of gas penetration [19]. Ribs of semicircular and rectangular sections (aspect ratio 0.5 min) and of increasing size were tested for mould-ability. The relative sizes of moulding window area defines the mould-ability index that ranges from excellent (5) to none (0). Rectangular sections are regarded as an equivalent semicircular radius (R_{eq}) and the thickness of the flat section is t. A plot of mould-ability index against R_{eq}/t shows that the size of the moulding window (i.e. mould-ability) increases when the ratio between rib cross sectional area and part thickness increases. The minimum value of R_{eq}/t to produce a good component is 2. These results contradict the design guideline for conventional injection moulding, where a maximum ratio of rib to part thickness is 0.5 [28, 20].

Increasing the size of a rib cross section too much can cause the melt in the rib to excessively lead the flow in the thinner section. This can develop air traps. Also, the residual wall thickness can increase to a point where the cooling time becomes excessive.

Yang et. al. [20, 24, 29, 25] have investigated the design of rib transition features. Figure 2.4 shows typical rib construction and the geometrical features employed at the base of a rib to act as a gas flow leader. The findings that correlate mould-ability with increased rib cross sectional area agree with the findings of Chen, mentioned previously. Ideally the gas bubble is best placed at the base of the strengthening rib to maintain rigidity and prevent sink marks on

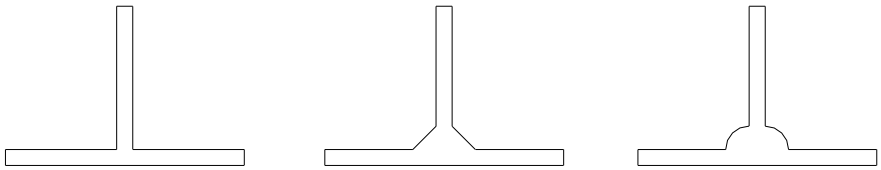

Figure 2.4: The mould-ability of rib sections can be improved by introducing a transition feature. Shown are a) right angle, b) chamfer and c) radius transition. Taken from Yang [20].

the opposite face. Yang found that chamfered and semi-circular transitions at the base of a rib tended to constrain the gas bubble penetration to the base of the rib. The semi-circular transition gave slightly better rigidity performance over a right angled and chamfer transition for an equivalent cross sectional area. The residual wall thickness was also more uniform in the semi-circular case, which assists uniform cooling.

2.3 Computer modelling of GAIM cavity filling and product performance

The approaches to modelling GAIM are typically governed by the computational requirements. The simulation products applied to conventional injection moulding are efficient and are widely used. However, these methods do not provide a full 3D definition of the gas bubble geometry. In order to obtain full 3D information a more complex 3D procedure needs to be employed, but this requires significantly more computational resource that may not be viable for some commercial

applications.

Simulation packages have been termed 3D, however this only refers to the product geometry that is defined in a Cartesian coordinate system [30]. The flow solvers only calculate velocities along the plane of flow and only approximate the fountain flow effect in the thickness direction. Such solvers are commonly referred to as $2\frac{1}{2}$D and employ the Hele-Shaw approximation.

2.3.1 Modelling conventional cavity filling

The products manufactured using the conventional injection moulding process are thin sectioned and the norm is to minimise variations in wall thickness. Therefore, the flow length to wall thickness ratio is high allowing scope for reductions in the calculated variables to significantly reduce the computational requirements. An approximation to flow in the thickness direction is typical for describing the fountain flow effect observed between parallel plates and within tubes. The Hele-Shaw approximation is one such method widely used in commercial mould filling packages.

2.3.1.1 The Hele-Shaw approximation

The generalised Hele-Shaw flow of inelastic, non-Newtonian fluids under non-isothermal conditions are set out by Turng (AC technology, developers of C-MOLD) [1],

$$\frac{\partial}{\partial z}\left(\eta\frac{\partial u}{\partial z}\right) - \frac{\partial P}{\partial x} = 0 \tag{2.2}$$

$$\frac{\partial}{\partial z}\left(\eta\frac{\partial v}{\partial z}\right) - \frac{\partial P}{\partial y} = 0 \tag{2.3}$$

$$\frac{\partial}{\partial x}\left(b\bar{u}\right) + \frac{\partial}{\partial y}\left(b\bar{v}\right) = F(x,y,t) \tag{2.4}$$

$$\rho C_p\left(\frac{\partial T}{\partial t} + u\frac{\partial T}{\partial x} + v\frac{\partial T}{\partial y}\right) = k\frac{\partial^2 T}{\partial z^2} + \eta\dot{\gamma}^2 \tag{2.5}$$

where, b is the half-gap thickness in z, $(^{-})$ denotes an average over z. The material properties η, C_p and k are viscosity, specific heat and thermal conductivity respectively. u and v are the velocity components in the x and y directions respectively. T, P and $\dot{\gamma}$ are temperature, pressure and shear rate respectively. The term $F(x,y,t)$ denotes the change in volume due to density variation during the cooling phase.

2.3.2 Extensions to conventional modelling techniques for GAIM

Commercial mould filling simulation packages such as C-Mold (now owned by Moldflow) and Moldflow offer modules to extend the solver capabilities to simulate gas assisted injection mould filling. Representation of the gas channels and multiple fluid injection are additional considerations. The results obtained from these methods generally report the fraction of polymer and gas within any given element, but the distribution of gas and polymer within the elements is not known. The bubble shape over the cross section of the cavity is therefore not available.

2.3.2.1 Representation of gas channels

Gas channels such as ribs have been represented by one dimensional beam elements superimposed onto the shell elements that represent the structure of the product [31, 32, 33, 34, 35, 36]. Gas channels are not generally tubular, but the cross sectional area can be equivalently represented by specifying an equivalent diameter (D_{eq}) to the beam element.

Although the beam cross sectional area matches that of the actual gas channel, the surface area around the outside of the channel may not be equivalent. Any difference in surface area will show an inaccuracy in the heat transfer. Therfore, a shape factor is applied to the beam element to account for this difference in surface area.

A mesh connects the beam element to the shell elements that represent the main structure of the product. Wang [21] has shown that the refinement of this mesh has a significant bearing on the gas penetration through the melt. Gas penetration is dependent upon melt temperature. The temperature profile over time of melt inside the beam element will be very different to that of melt inside an adjoining shell elements, representing thin walls. A finer mesh is therefore needed to accurately map the temperature profile in the connecting region. Wang found that a low mesh density reduced the temperature inside the beam element too quickly; under prediction of gas penetration was a problem.

2.3.2.2 Discrimination between polymer and gas

The assignment of labels to dissimilar fluids in the modelling domain is a typical dual filling parameter technique. This principle is adapted from the modelling of co-injection moulding where two different polymer materials are injected into a single mould cavity. Chen [37] explains how C-Mold utilises two parameters to define gas and melt, which are f_{gas} and f_{melt} respectively. Values for these parameters are calculated at nodes and are in the range $0 \leq f \leq 1$. Nodes that connect elements containing the gas polymer interface are within the range $0 \leq f \leq 1$. Other nodes that are inside the gas or polymer regions will have the values $f_{melt} = 0; f_{gas} = 1$ and $f_{melt} = 1; f_{gas} = 0$ respectively.

A pseudo-concentration approach has been used by Haagh [2, 38, 39]. A single material parameter, c, is assigned to each nodal point. The concentration parameter is in the range $0 \leq c \leq 1$, where polymer and gas are represented by $c = 1$ and $c = 0$ respectively.

2.3.2.3 Secondary gas penetration

When primary penetration of the melt by the gas bubble is complete, compensation for melt shrinkage during cooling forms the secondary penetration phase. Secondary penetration has been shown to be a highly significant contribution to final bubble position [40]. Therefore some modelling approaches have attempted to consider the adjustment of the gas bubble position, after primary injection, due to polymer shrinkage under maintained gas pressure.

Chen et. al. [35, 41] developed an isotropic melt shrinkage model to predict

bubble front advancement in both the planar and gapwise directions. The control volume finite element method, used to model primary gas penetration, was found to incorrectly predict both final penetration length and geometry correctly. This suggests that a pressure driven flow model can not reliably predict secondary penetration.

Chen et. al. provide the only published material found by the author to tackle the significant problem of secondary penetration by the gas bubble during the cooling phase.

2.3.2.4 Three dimensional models

The fundamental advantage of 3D models over $2\frac{1}{2}$D is that no assumptions about the final bubble shape needs to be made in order to complete the simulation. Flow physics determine the shape of the bubble because velocities are calculated in three dimensions.

The approach used by Haagh [2, 38, 39] to model mould filling utilises brick elements to form a 3D fixed grid. There is no need for elaborate re-meshing of the grid during the solution. The fixed grid approach using linear quadrilateral elements is used within this thesis.

The results from 3D models will contain information about the position of the polymer melt and the gas bubble through the thickness and along the direction of flow. This type of result becomes important when the shape of the gas channel is irregular and the bubble formation is also irregular. For example, the rectangular capillary investigated by Kolb [14] and shown in figure 2.1 is irregular in shape.

The collection of polymer in the corners is typical, but only a 3D simulation result would provide information about this effect.

An attempt to improve the accuracy of flow front prediction and gas bubble front location is made by Coupez et. al. [42] using an adaptive mesh. As the interface between two fluids passes through the mesh a routine reduces the size of the elements containing the fluid interface. CPU time to run the re-meshing routine is reported to be comparatively small

2.3.3 Prediction of product performance from processing conditions

The application of gas to strengthening ribs to provide better structural performance has highlighted a need to predict the structural performance based on the expected filling results; this has been attempted by Hu et. al. [34]. In the work of Hu, a 3D solid model was constructed for stress analysis and the geometry taken from a manufactured ribbed plaque moulding. By comparison, a thin shell model is also constructed, but the mesh is taken from a flow simulation employing a $2\frac{1}{2}$D approach and superimposed beam elements to represent the gas channels. The results of the load deflection analysis compared with the experiment on the real moulding show that the 3D model is more accurate, partly due to the 3D model being based on the real geometry in the first place. However, this exercise exposes the need for a fully described bubble geometry from the flow simulation to improve the accuracy of a subsequent stress analysis.

Chapter 3

Experimental procedures

3.1 Introduction

An overview of the equipment used in manufacturing the tensile test specimens will be given. The phenomenon observed within the process measurement is discussed in more detail in chapter 4.2.

3.2 Overview of the gas assisted injection moulding processing equipment

The current state of the art for GAIM is to attach gas injection equipment with a separate controller to an existing injection moulding machine. The processing machinery used in this thesis is supplied by Battenfeld (UK). The system comprises of a standard injection moulding machine attached to a gas injection system, which has the trade name Airmould. Important specifications of the

Screw diameter	40	mm
Max screw stroke	160	mm
Max hydraulic pressure	140	bar
Intensification ratio	11.25	
Max screw velocity	106	mm/s
Max screw rotation speed	275	RPM
Max back pressure	40	bar
Max clamp force	750	KN
Max gas pressure	350	bar
Max gas control valves	4	

Table 3.1: Machine specifications for the Battenfeld CDK750 injection moulding machine and Airmould system. (Taken from machine manual [43].)

machine are shown in table 3.1.

The entire GAIM system comprises of three modules that include the injection moulding machine, the gas injection system and the robot, each with there own controllers. Both the robot and gas injection controllers connect to the injection moulding machine controller.

A signal to the gas injection controller from the injection moulding machine triggers the timer sequences and gas pressure time profiles. This trigger is the only signal communicated. The robot communication is more complicated since interlocks on the doors covering the tool platens and the melt injection unit must be incorporated to prevent injury from the robot operation. Similarly the robot needs to receive information about the cycle and ensure collection of the product is completed at the right time to avoid damage.

Hydraulic and servo-electric are two major types of actuation system for injection moulding machines. The Battenfeld is a hydraulic, which means that all actuation of the clamping mechanism and the melt injection system is controlled

using hydraulic cylinders. The servo-electric machines utilise re-circulating ball lead screws, driven by motor, to actuate the clamping and melt injection systems.

The state of the art for hydraulic machine control is to utilise a servo valve for controlling the hydraulic pressure used to actuate the melt injection screw, inside the machine barrel. A servo-valve directs hydraulic oil into the actuation cylinder for the screw from an already pressurised source. This means that the time response of the hydraulic pressure driving the melt injection unit is relatively small. The pressure following to controller set points is much improved over previous systems. One such system is the proportional control that utilises a hydraulic motor to directly generate the injection pressure. The motor needs to increase in speed to increase the available hydraulic pressure. Therefore, due to significant inertia within the motor, the time response to controller set points is significant enough to limit the control of melt injection.

3.3 Process monitoring

Process monitoring gives substantial insight into the actual state of a process. Significant differences between the process settings and the actual process response are observed. A computer data acquisition system is implemented to log signals from transducers placed on the melt and gas injection units.

Injection pressure and screw displacement have been identified as important process responses for the conventional injection moulding process [44, 45]. The injection pressure profile over time, during primary melt injection, is a *fingerprint* for the process stability. The profile of the pressure signal indicated restrictions

Feature	Specification
Max sample frequency	500 KS/s per channel
Resolution	12 bit (1 in 4096)
Max channels	16
Interface	PCI bus

Table 3.2: National instruments data acquisition card: specification [46].

to flow within the cavity. The repeatability of the pressure profile from shot to shot is an indicator of process stability. Changes in material, melt temperature and other process variables usually influence the form of the profile. The use of the injection pressure profile is described more fully in section 3.4.

3.3.1 LabVIEW data acquisition system

Signals from the transducers that monitor the GAIM process are collected by a PC running LabVIEW software. An integral part of the LabVIEW system is the National Instruments data acquisition (DAQ) card, which is mounted inside a PC. The DAQ card provides an interface for the signals from the transducers. The specification of the DAQ card is listed in table 3.2.

The LabVIEW system, which includes the DAQ card, handles various voltage ranges, which are, ± 5, ± 10 and 0 to +10V. The latter range of 0 to +10V is used here since some of the transducers provide that range as a standard output. This voltage range also offers maximum resolution over the 12 bit analogue to digital conversion.

The data logging is started by a trigger signal from the injection moulding machine control system. The signal used indicates the start of melt injection, also called primary injection. The trigger signal from the machine is a step change

in voltage from 0 to +24V. A voltage divider reduces the +24V trigger signal to +10V before connection into a digital input on the DAQ card.

3.3.2 Description and calibration of transducers used to measure the GAIM process

The melt injection unit comprises a heated barrel and a feed screw that injects melt into a cavity and is actuated by a hydraulic piston. This system of the injection moulding machine prepares the melt from polymer granules and injects the melt, through a nozzle, into the mould cavity. Both the position of the screw and the hydraulic pressure controlling the piston are monitored.

The nitrogen gas is injected into the mould through a needle that protrudes into the melt. An alternative method is to inject gas through a specially equipped nozzle fitted to the end of the machine barrel. A pressure transducer is fitted to the gas injection manifold mounted on the tool. Here the gas pressure into the needle can be measured as close as possible the the needle. This is important because the gas pressure drop through the piping to the gas needle due to flow does not effect the measurement.

Gas can penetrate from the cavity back into the machine barrel if left unchecked. The specially equipped gas injection nozzle fitted to the end of the machine barrel is used to stop this uncontrolled gas penetration. Unfortunately, this arrangement prevents nozzle pressure and temperature measurements being made, which would otherwise have been possible with a specially designed rheometric nozzle.

The specifications of the transducers used to monitor the process are listed in

Transducer	Specification
Screw position	Temposonics LP TTM-R0-M-0160-R 0–160mm range
Hydraulic pressure	Dynisco IDA354-2CD21 0–200 bar range
Gas pressure	Dynisco IDA354-2CD21 0–200 bar range

Table 3.3: Specification of transducers used to monitor the GAIM process.

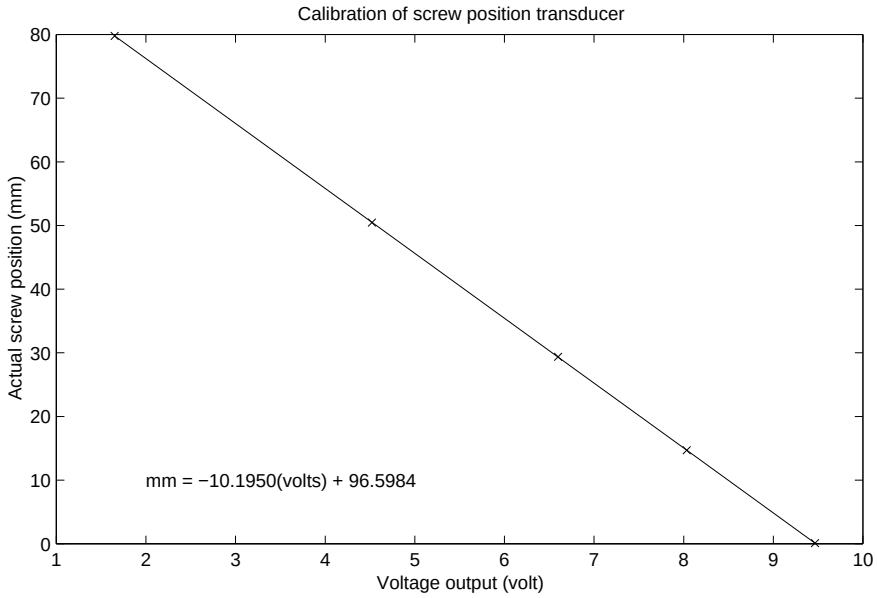

Figure 3.1: Calibration of the screw displacement transducer.

table 3.3.

3.3.2.1 Screw displacement and velocity

A displacement transducer attached to the screw actuation piston measures the position of the injection screw. A magnetorestrictive linear displacement transducer (MLDT) is used, which is supplied with an analogue output module (AOM). The AOM provides two signals, one for displacement and the other for velocity. Each signal is output form the AOM in a 0 to +10V range.

The calibration of the screw displacement transducer requires relationship

between a measurement on the screw position with vernier callipers and the voltage signal into LabVIEW. The measured screw position needs to be offset to match the position of the screw reported by the UNILOG 4000 controller. A plot of the calibration points and the equation of the calibration are shown in figure 3.1.

The velocity of the screw is calculated from the displacement against time data.

The repeatability and maximum range of the displacement transducer is 0.006mm and 160mm respectively [47]. However, the resolution obtainable from the data acquisition system is 160mm/4096 = 0.039mm.

3.3.2.2 Hydraulic injection pressure

The hydraulic oil pressure transducer is connected to the output port of the servo-control valve that controls the oil pressure driving the injection screw. The transducer is a stain gauge type from Dynisco instrumentation which has a shunt calibration feature. However, in order to check the calibration thoroughly a Budenburg dead weight testing device is used. The Budenburg provides an accurately know hydraulic pressure to calibrate the transducer voltage against. The calibration points and equation are shown in figure 3.2.

The accuracy and repeatability of the transducer is 0.5 bar (±0.25% f.s.d.) and 0.2 bar (±0.1% f.s.d.) respectively [48]. The resolution of the data acquisition system is 200 bar/4096 =0.049bar, which is better than the transducer.

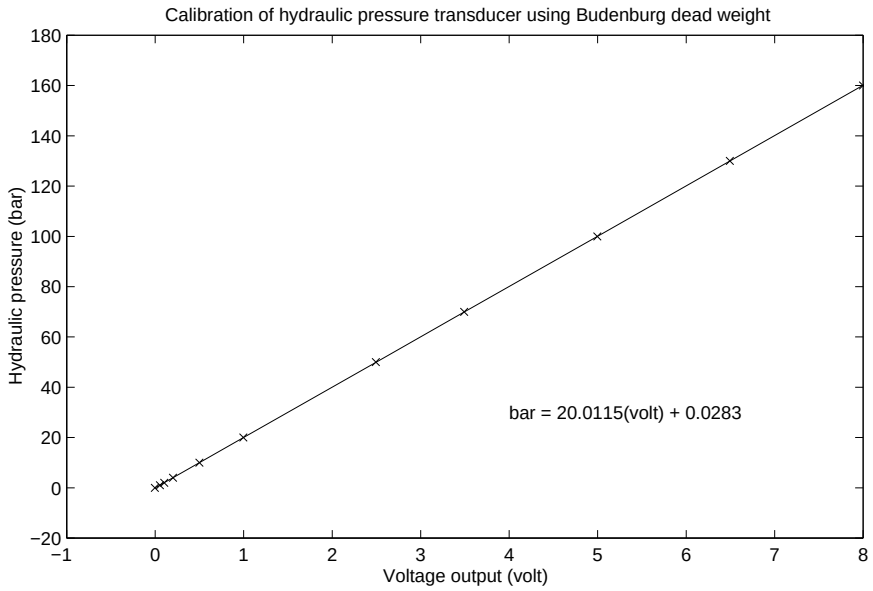

Figure 3.2: Calibration of the hydraulic pressure transducer.

3.3.2.3 Gas pressure

The gas pressure transducer has the same specification as the hydraulic pressure transducer. Although the maximum gas pressure available is 350 bar, in practice this was not utilised and was generally below 200 bar. The damage pressure for this transducer is 500 bar, which is in excess of the maximum pressure the transducer may experience. Again the Budenburg dead weight testing machine is used for calibration and the calibration result is shown in figure 3.3.

The resolution of the gas pressure transducer is the same as the hydraulic pressure transducer, which is 0.049bar.

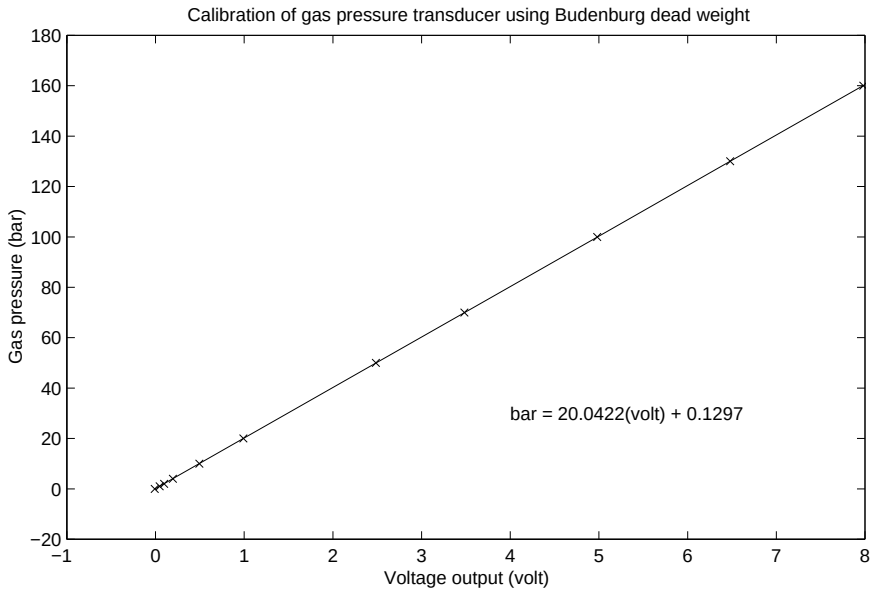

Figure 3.3: Calibration of the gas pressure transducer.

3.4 Specific pressure integral as an indicator of process stability

An integral of the injection pressure profile is taken in order to obtain a gauge of process stability. The calculation of the viscosity index (VI) is illustrated in figure 3.4, which shows a typical hydraulic pressure profile during melt injection under velocity control. The integral is taken in a low noise region, which is over the range 60% to 80% of the primary injection curve. The VI is calculated in real time by a computer module that logs hydraulic pressure. During manufacturing of the specimens the display of VI shows a change over time that corresponds to the system settling after start up. Specimens manufactured during the start up phase are discarded.

Changes in the VI value are associated with changes in material, melt tem-

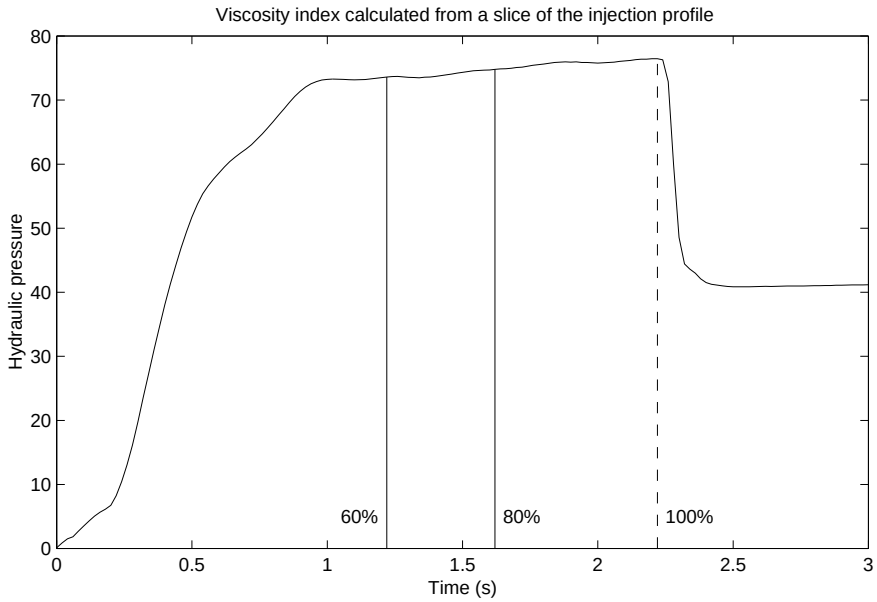

Figure 3.4: The viscosity index is calculated by integrating the melt injection pressure curve in a low noise region between 60% and 80% of the primary injection time.

perature and mould temperature. This list is not exhaustive. The development of the VI measurement and technology used to provide the value at the machine in real time can be attributed to authors such as Speight, Dawson and Coates [45, 49, 50].

3.5 Tensile test specimen design and analysis

A number of measurements are made on the tensile specimens produced by the GAIM process. Weight is a useful indication of process stability and relates to the fraction of polymer present within the mould. A wall thickness measurement is made on a cross section from the gauge length. Shrinkage after ejection and the gas bubble penetration into the melt are monitored. These sections outline the

design features of the tensile test specimen and the analysis methods employed.

3.5.1 Form of the GAIM tensile test specimen

The tensile test specimen form provides a gauge length of constant section over 13 section lengths. The simple cross sectional form is useful for comparison with simulation results. The complete cavity form is shown in figure 3.5. The melt is injected into the cavity in a runner system that channels the melt to the specimen. Melt flows into the specimen through a gate. The gates available in this work are a tab gate shown in figure 3.5 and an open gate that does not restrict flow from the runner.

The gas injection needle protrudes into the centre of melt flow. Gas must be injected behind the melt flow front in order to core out the melt and to complete filling of the cavity. The tab gate is useful since it prevents gas from flowing back along the runner system and into the machine barrel. However, the tab gate will be shown to cause shear heating within the melt and a differential wall thickness along the gauge length is observed. A gas injection nozzle with a non-return valve is fitted onto the barrel to prevent gas penetration into the machine barrel when the tab gate is not in place. This arrangement also facilitates injection of gas from the gas nozzle fitted to the barrel.

There is no standard for designing the tensile test specimen since the gas assisted injection moulding process is not covered by any of the ISO or BS standards. The standard that do relate to plastics are generally for determining material properties and require test specimens made by the conventional injection

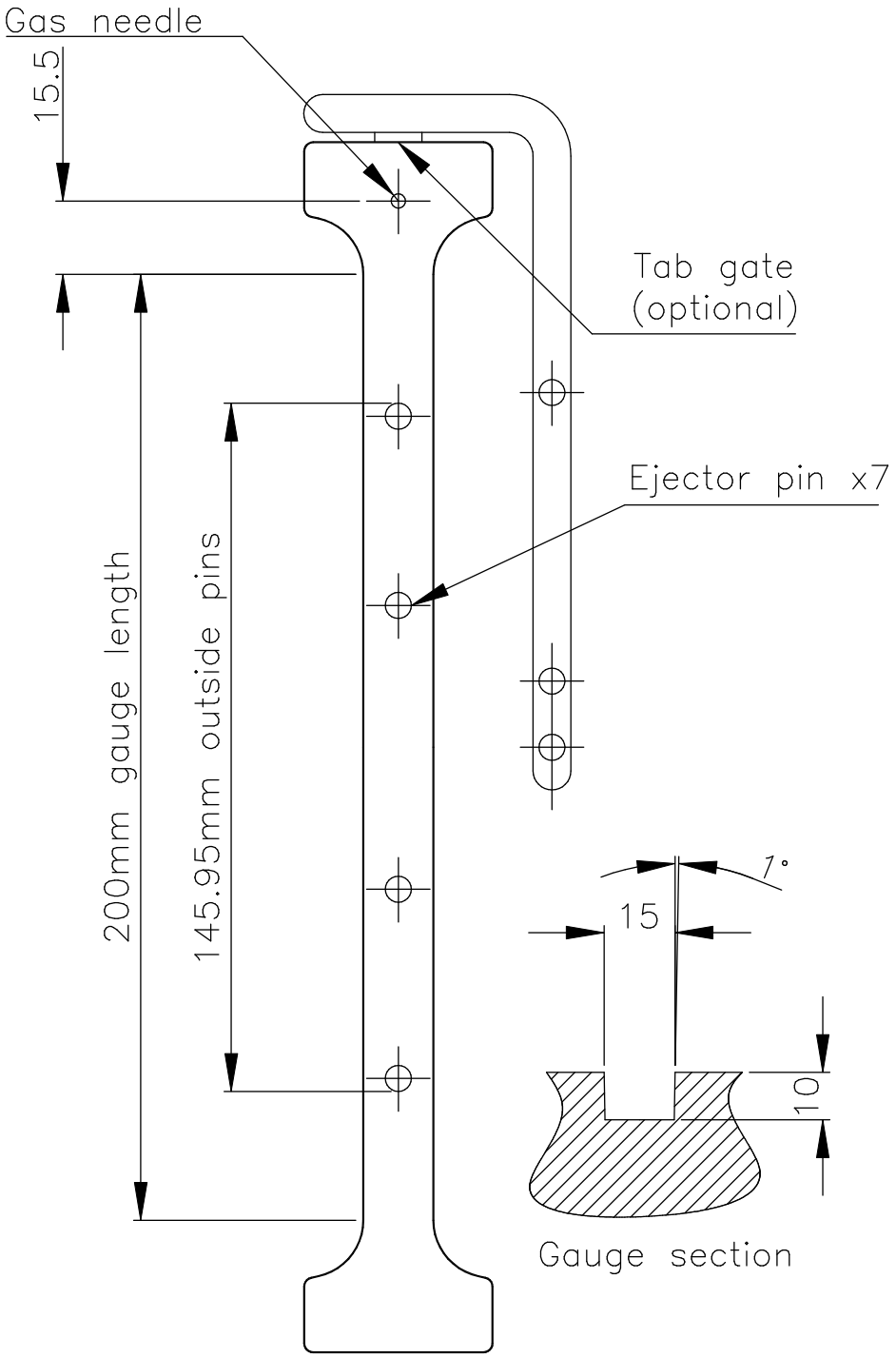

Figure 3.5: An outline of the cavity used to form the GAIM tensile test specimen.

moulding process [51].

3.5.2 Wall thickness measurement using an image analysis technique

The image analysis technique developed here provides residual wall thickness measurements. A section is extracted from the gauge length and placed on a standard flat bed scanner. An grey scale image of the section is produced from scanning that can used to provide the wall thickness data. The image is made up from pixels that discretise the section into known units of area, analogous to placing fine graph paper over the image.

A program written to analyse the pixels within the image counts the number of pixels from one surface to another. The pixel count is then converted into a dimension that specifies wall thickness.

3.5.2.1 Measurement locations

A section is extracted from the specimen gauge length in order to measure the residual wall thickness. Also, a section is cut from the last to fill area of the specimen to expose the bubble penetration tip for measurement of its position. Figure 3.6 shows the positions of the cut lines more clearly. The section for wall thickness analysis is extracted at a position 50mm along the gauge length.

Wall thickness measurements are taken along the central axes of the long and short cross section dimensions. Figure 3.7 shown the central axes of the cross section and indicates the label assigned to identify each wall. The FIXED

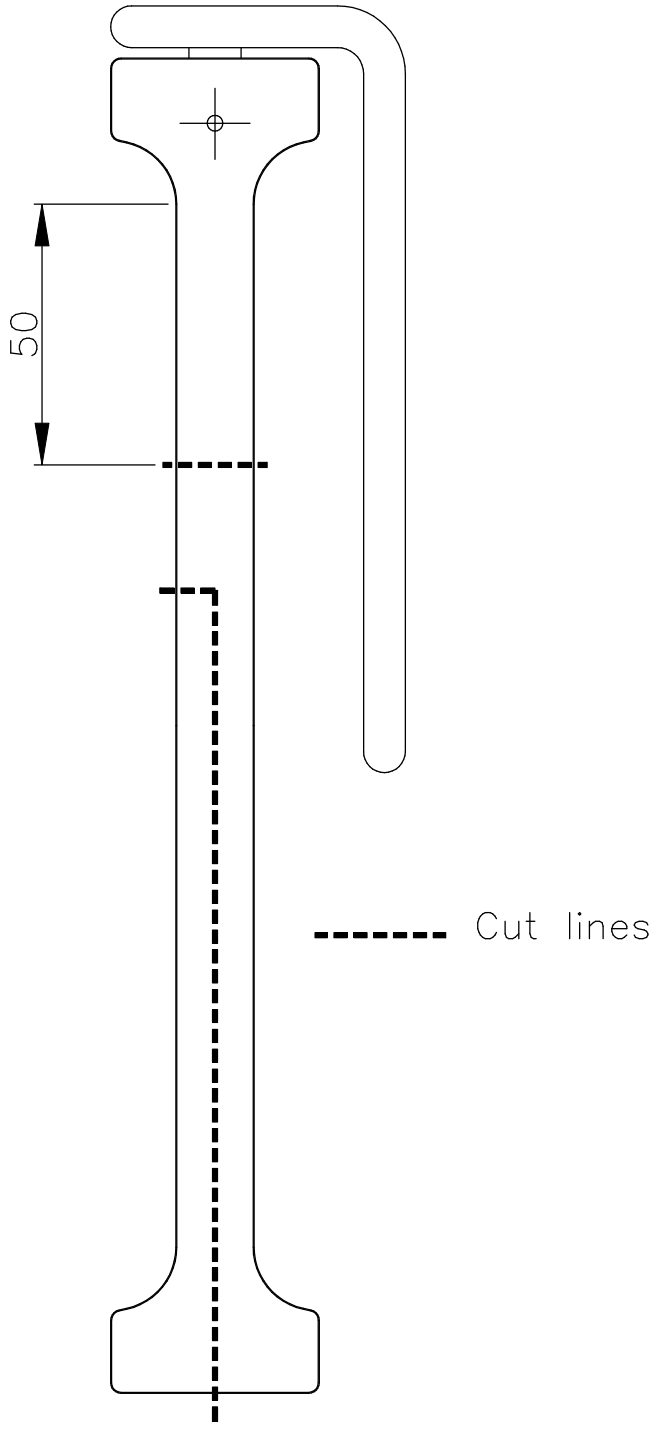

Figure 3.6: The section for scanning is taken from a position 50mm along the gauge length. Bubble penetration is measured along the centreline.

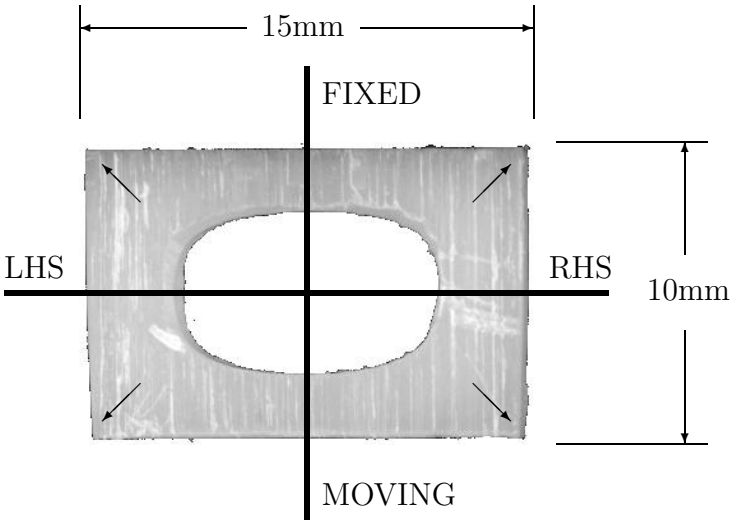

Figure 3.7: Definition of wall thickness measurement positions and corner points

and MOVING walls relate to the fixed and moving halves of the mould cavity respectively. LHS and RHS relate to the left and right hand walls respectively to an observer looking along the gauge length against the flow direction (i.e. towards the gas needle). The cross section of the gauge length has the dimensions 15mm by 10mm and has a 1^o draft on the LHS and RHS sides to facilitate ejection from the mould.

The image analysis software locates the corners of the cross section by finding the intersections of the upper and lower extremities of material pixels in the x and y directions. This accuracy of this method is dependent upon a squared orientation of the cross-section on the scanner. To ensure good orientation a plastic film was set up on the scanner to locate the cross section against before scanning.

Once the corners of the specimen cross section have been found the central x-y-axes can be determined. A routine searches along these axes to find a material

pixel that indicates a surface. The routine counts the pixels to the next surface to determine the distance between the surfaces and provide a wall thickness measurement.

An issue for the image analysis software is what constitutes a material pixel? The pixel colour within the image of the cross section is represented by a grey scale. The scale is from 0 to 255, where 0 and 255 represent black and white respectively, in between a shades of grey. In order to decide if a pixel is a material pixel a threshold value for the grey scale is set, so only pixels above the value represent material.

Figure 3.8 shows the original scanned image after applying a number of different threshold values to indicate which pixels the image analysis software will count as material. If the threshold is too low, as in figure 3.8a, which is set to 5, rouge pixels that are almost black may be counted. The rouge pixels are probably from ambient light and reflections off the material.

Setting the threshold value too high, as in figure 3.8d, which is set to 190, genuine material pixels may not be counted. A threshold of 40 gives the closest representation of the original image. Figure 3.9 indicates how the image pixel count above the threshold value changes with the threshold value. A big change in pixel count is evident at the low thresholds as the rouge pixels are eliminated from the count. The steadily decreasing pixel count between threshold 10 to 70 shows a pixel count of 67.66% and 67.22% of the total image respectively. A threshold value of 40 is used to determine material pixels.

The nominal optical resolution of the scanner is quoted to be 600 dots per

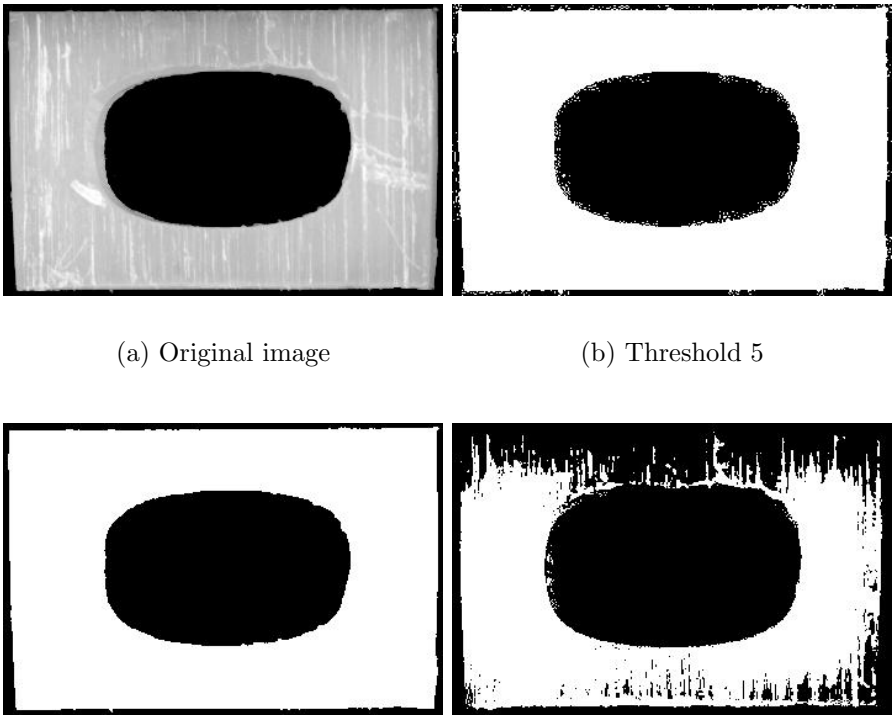

(a) Original image (b) Threshold 5

(c) Threshold 40 (d) Threshold 190

Figure 3.8: Application of a pixel grey scale threshold to the cross section image

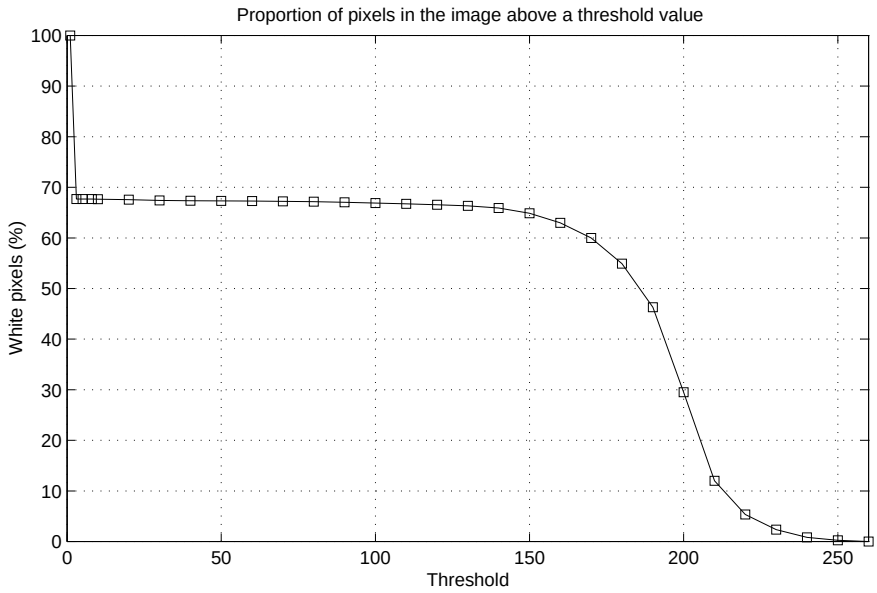

Figure 3.9: The proportion of the cross section image above the grey scale threshold value.

inch (dpi). The resolution is checked using a slip gauge that has accurately known dimensions and sharp edges. The slip gauge is scanned at different resolutions and the size in pixels checked against the nominal resolution setting. Figure 3.10 shows a plot of the difference between the actual resolution and the nominal setting controlled by the scanner software.

A resolution of 600dpi is the highest possible optically, so is used to obtain images of the specimen cross sections. A correction is made for the difference between the actual and nominal resolutions in the x and y directions. Other higher resolutions are possible, but the scanning software interpolates between pixels to infer the higher resolution, which may introduce some error.

The resolution of a pixel at 600dpi is nominally 0.042mm. A digital vernier calliper has a resolution of 0.01mm with a repeatability of $\pm$0.02mm. The im-

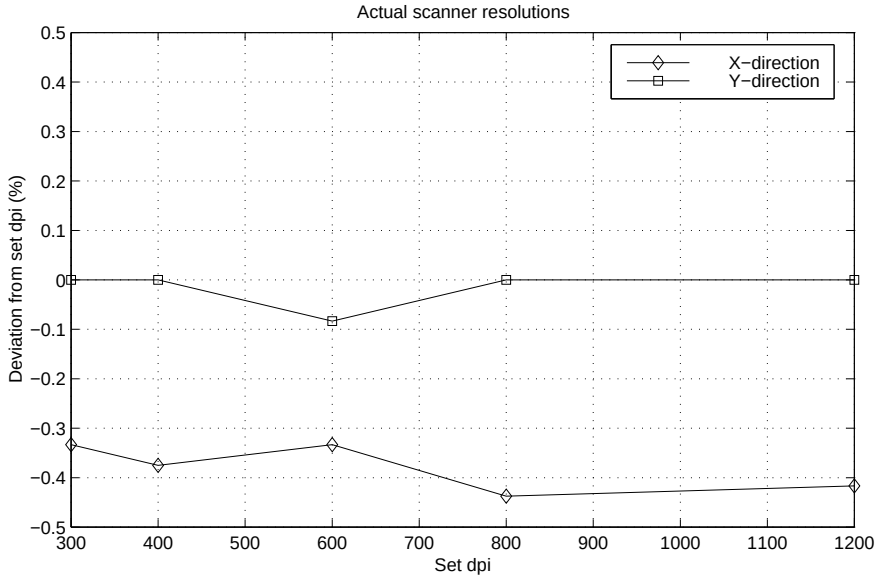

Figure 3.10: Nominal scanner resolution checked against the actual value.

age analysis technique is less accurate than a vernier calliper in terms of raw resolution. However, the positioning of the vernier calliper to measure the wall thickness is less repeatable by the human hand. Also, the image of the cross section provides a permanent record that can be used to make other measurements in future work, such as area, second moment of area and bubble shape.

3.5.3 Gas bubble penetration

The gas bubble penetration into the melt is measured with vernier callipers. A section is made along the length of the specimen, shown in figure 3.6, to expose the gas bubble and observe the penetration tip. This method does rely upon the gas bubble forming in the centre of the specimen, which is observed to be the case. The penetration measurement is taken from the gas needle location (seen as a hole in the wall) to the bubble tip. The observed gas bubble penetration

included primary and secondary penetration.

3.5.4 Specimen shrinkage

Ejector pin marks on the specimen gauge length are used to determine the post ejection shrinkage of the specimen. The ejector pin locations within the tool are known. The outside dimension of the relevant ejector pins is 145.95mm and is illustrated in figure 3.5. The distance between the matching ejector pin impressions left on the specimen gauge length are recorded. Shrinkage is determined according to equation 3.1.

$$shrinkage\ (\%) = \frac{145.95 - marks\ distance}{145.95}\ \text{x}\ 100 \tag{3.1}$$

It is important to ensure that the specimens have fully cooled and ceased changing shape before measuring the shrinkage dimension. Moller [52] has shown that the treatment of plastics products after ejection from the mould can effect the final dimensions. The specimens here are left to cool overnight before any dimensional measurement are taken.

3.5.5 Specimen mass

The specimens, tensile bar and runner system, are weighed using a digital balance. Again, the specimens must be fully cooled to prevent the air currents generated by the hot plastic form lifting the specimen and effecting the mass reading. Also, to ensure repeatability in placement of the specimens on the balance, the specimens are hung from a wire frame that sits upon the balance. It has been found that

specimens placed flat on the scale cause the mass reading to vary upto ±1.0g, presumably due to variation in centre of mass.

3.6 Design of experiments

The design of experiments approach is an efficient method for generating an empirical model of system response. An example is the mapping of the fuel flow and NO_x response of an engine to variables such as engine speed, torque and spark angle [53]. The method is used here to map the formation of the residual wall thickness to GAIM process variables.

3.6.1 Fractional factorial orthogonal arrays

An approach to experimentally obtaining data on a systems response to changes in system variables is to hold all other variables constant and change only 1 variable at a time. This is commonly termed a full-factorial approach. If say 3 variable are tested at 2 levels then $2^3 = 8$ experiments are necessary to cover all permutations. However, if many variable are tested at a number of different levels, the number of experiments can be significant. For example, 7 variable tested at 2 levels needs $2^7 = 128$ experiments, 13 variables at 3 levels requires over 1.5 million experiments to cover all possible combinations.

Run	**A**	**B**	**C**	**D**	**E**	**F**	**G**	**H**	Response
1	-1	-1	-1	-1	-1	-1	-1	-1	y_1
2	-1	-1	0	0	0	0	0	0	y_2
3	-1	-1	+1	+1	+1	+1	+1	+1	y_3
4	-1	0	-1	-1	0	0	+1	+1	y_4
5	-1	0	0	0	+1	+1	-1	-1	y_5
6	-1	0	+1	+1	-1	-1	0	0	y_6
7	-1	+1	-1	0	-1	+1	0	+1	y_7
8	-1	+1	0	+1	0	-1	+1	-1	y_8
9	-1	+1	+1	-1	+1	0	-1	0	y_9
10	+1	-1	-1	+1	+1	0	0	-1	y_{10}
11	+1	-1	0	-1	-1	+1	+1	0	y_{11}
12	+1	-1	+1	0	0	-1	-1	+1	y_{12}
13	+1	0	-1	0	+1	-1	+1	0	y_{13}
14	+1	0	0	+1	-1	0	-1	+1	y_{14}
15	+1	0	+1	-1	0	+1	0	-1	y_{15}
16	+1	+1	-1	+1	0	+1	-1	0	y_{16}
17	+1	+1	0	-1	+1	-1	0	+1	y_{17}
18	+1	+1	+1	0	-1	0	+1	-1	y_{18}
									$\bar{y}$

Table 3.4: The L18(2^1x3^7) orthogonal array

3.6.2 The L18(2^1x3^7) experimental array

A number of orthogonal experimental arrays are available, some with 2 levels and others with more, for each factor. Also, some arrays are arranged such that interactions between main factor effects can be studied. Interactions and the potential problem of confounding will be outlined in section 3.6.3.

The experimental array used here is an L18(2^1x3^7), which can test 7 factors at 3 levels and 1 factor at 2 levels. The array is shown in table 3.4. The experiment will consist of setting each experimental variable to the prescribed setting over each of the 18 runs and recording the response for the respective run.

One reason for choosing the L18 array is that interactions are spread evenly

across all columns, so the effects of all 8 factors can be studied without confounding, which is numerically blending an interaction with a main effect [53, 54]. Three level settings for each factor have an advantage over two levels because non-linearity can be observed in the factor effect upon the response. This is explained later in this section.

The coding system of -1, 0 and +1 within the array is convenient for later analysis, when quadratic and interaction columns will be generated.

3.6.2.1 Orthogonality and balance

The experimental array shown in table 3.4 displays the properties of balance and orthogonality, which are fundamental to the analysis of the experimental data. A correlation of zero exists between any of the columns within the array. This means the effect of any variable assigned to a column can be calculated independently of other variables and this is the property of orthogonality. An analogy can be drawn with the spacial orthogonality between Cartesian axes (x,y,z) where the movement along one axis is independent of movement along any of the others. In essence the data sets do not move with each other. The property of balance exists in each column since there is an equal occurrence of a variable settings. Specifically, the number of +1, 0 and -1's in any column is the same [53].

3.6.3 Factor interactions and confounding

Interactions between main factors are likely to exist in any system. Some experimental arrays can be used to study interactions if the factor column is made up

from a combination of two or more other columns. However, if a column that can be used to study an interaction is assigned to a main factor then the effect observed for that column is a combination of the main effect and the interaction. This is called confounding. If the interaction is strong then the effect of the main factor could, depending on the sign, be increased or cancelled out by the interaction. The L18 array in table 3.4 does not have inherent interaction columns, so confounding is eliminated [53].

3.6.4 Main factor and interaction effects

The analysis of the experimental data within the frame work of the L18 array will utilise multiple regression. The standard L18 array is extended to form the quadratic elements of the variable effects upon the responses and any interaction present. Figure 3.11 shows the quadratic columns and the interaction columns between factors A and B. The quadratic columns for each factor are generated by squaring each element in the factor column and subtracting the mean of the new quadratic column. Subtracting the mean of the values within the column ensures that the covariance between columns is zero, which maintains orthogonality. The quadratic columns are used to determine the component of non-linearity on the response.

Analysis of an experimental array will reveal which of the main factors are the most significant to the system response. Analysis of means (ANOM) is used to provide a response table for each factor by finding the mean response at each factor level. For example, equation 3.2 shows how to calculate the effects E_{-1}, E_0

	Main Factors								Quadratic and interactions								
RUN	A	B	C	D	E	F	G	H	Bq	Cq	Dq	Eq	Fq	Gq	Hq	AxB	AxBq
1	−1	−1	−1	−1	−1	−1	−1	−1	1/3	1/3	1/3	1/3	1/3	1/3	1/3	1	− 1/3
2	−1	−1	0	0	0	0	0	0	1/3	− 2/3	− 2/3	− 2/3	− 2/3	− 2/3	− 2/3	1	− 1/3
3	−1	−1	1	1	1	1	1	1	1/3	1/3	1/3	1/3	1/3	1/3	1/3	1	− 1/3
4	−1	0	−1	−1	0	0	1	1	− 2/3	1/3	1/3	− 2/3	− 2/3	1/3	1/3	0	2/3
5	−1	0	0	0	1	1	−1	−1	− 2/3	− 2/3	− 2/3	1/3	1/3	1/3	1/3	0	2/3
6	−1	0	1	1	−1	−1	0	0	− 2/3	1/3	1/3	1/3	1/3	− 2/3	− 2/3	0	2/3
7	−1	1	−1	0	−1	1	0	1	1/3	1/3	− 2/3	1/3	1/3	− 2/3	1/3	−1	− 1/3
8	−1	1	0	1	0	−1	1	−1	1/3	− 2/3	1/3	− 2/3	1/3	1/3	1/3	−1	− 1/3
9	−1	1	1	−1	1	0	−1	0	1/3	1/3	1/3	1/3	− 2/3	1/3	− 2/3	−1	− 1/3
10	1	−1	−1	1	1	0	0	−1	1/3	1/3	1/3	1/3	− 2/3	− 2/3	1/3	−1	1/3
11	1	−1	0	−1	−1	1	1	0	1/3	− 2/3	1/3	1/3	1/3	1/3	− 2/3	−1	1/3
12	1	−1	1	0	0	−1	−1	1	1/3	1/3	− 2/3	− 2/3	1/3	1/3	1/3	−1	1/3
13	1	0	−1	0	1	−1	1	0	− 2/3	1/3	− 2/3	1/3	1/3	1/3	− 2/3	0	− 2/3
14	1	0	0	1	−1	0	−1	1	− 2/3	− 2/3	1/3	1/3	− 2/3	1/3	1/3	0	− 2/3
15	1	0	1	−1	0	1	0	−1	− 2/3	1/3	1/3	− 2/3	1/3	− 2/3	1/3	0	− 2/3
16	1	1	−1	1	0	1	−1	0	1/3	1/3	1/3	− 2/3	1/3	1/3	− 2/3	1	1/3
17	1	1	0	−1	1	−1	0	1	1/3	− 2/3	1/3	1/3	1/3	− 2/3	1/3	1	1/3
18	1	1	1	0	−1	0	1	−1	1/3	1/3	− 2/3	1/3	− 2/3	1/3	1/3	1	1/3

Figure 3.11: The L18(2^1x3^7) array is extended to produce quadratics and interactions.

and E_{+1} for the settings -1, 0 and +1 respectively, of factor C on the response. A similar calculation can be made for all other factors and interactions to provide a response table of effects.

$$\begin{aligned} \frac{y_1 + y_4 + y_7 + y_{10} + y_{13} + y_{16}}{6} &= E_{C(-1)} \\ \frac{y_2 + y_5 + y_8 + y_{11} + y_{14} + y_{17}}{6} &= E_{C(0)} \\ \frac{y_3 + y_6 + y_9 + y_{12} + y_{15} + y_{18}}{6} &= E_{C(+1)} \end{aligned} \tag{3.2}$$

3.6.4.1 Effects plot

An effects plot is used to visualise the effects calculated in equation 3.2. An example plot for 2 factors at 3 levels is shown in figure 3.12, which shows how the response is effected by factor settings. The relative influence that each factor

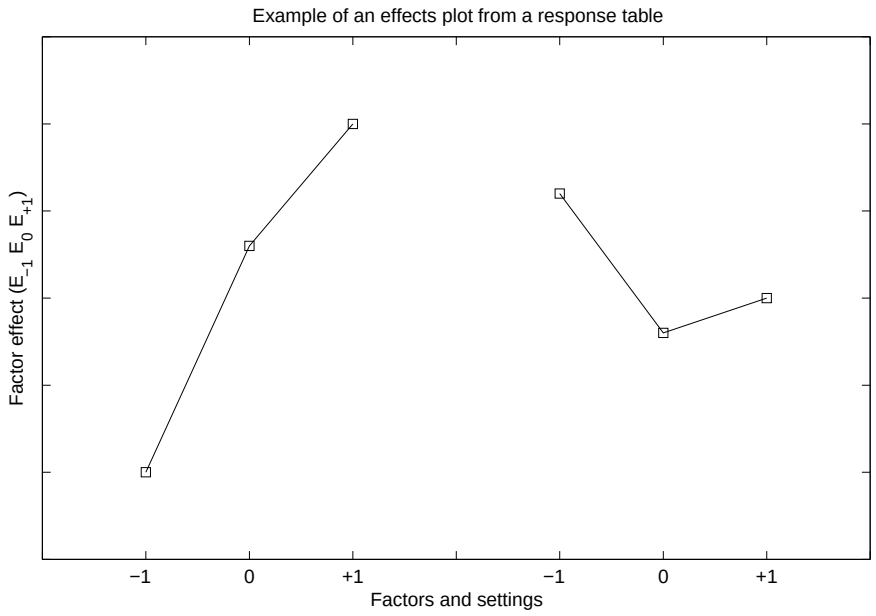

Figure 3.12: Example of an effects plot for 2 factors at three levels.

has on the response can also be gauged from an effects plot.

3.6.4.2 Multiple regression analysis

Multiple regression is used to provide a model of the response variable described by the independent variables. The regression model is of the form shown in equation 3.3.

$$y = b_0 + b_1x_1 + b_2x_2 + \cdots + b_nx_n \tag{3.3}$$

The predicted response is denoted by y, the independent variables are x and the respective regression coefficients are b. The values of b are calculated using a least squares method that seeks to minimise the residual value [55]. The residual is the difference between the observed and the predicted response.

The details of the least squares calculation will not be presented here. A

computer program (MS Excel) is used to calculate the regression statistics. The regression statistics are used to determine the significance of each variable in effecting the response. The t-statistic indicates the ratio between the value of a regression coefficient and the standard error. Grove and Davis [53] propose that a t-statistic greater than 2.0 indicates that a coefficient is significant, although tables do exist of critical t values. This rule means that a coefficient has to be at least twice as big as its standard error before it is considered likely to represent a real effect [53].

The p-value from the regression statistics shows the probability that the relevant coefficient is modelling random noise. The lower the p-value the more likely that the coefficient is active. The goodness of fit of the regression model to the observed responses is indicated by the R^2 values that is termed the coefficient of multiple determination [55]. An R^2 value of 0.96 would indicate that 96% of the variation within the observed response is covered by the regression model and 4% is due to extraneous factors not accounted for in the model. The rules on the R^2 value are not fixed, but the closer the value is to 1.0 the better and it can be used to see the effect of dropping or including a variable from the regression equation.

3.6.4.3 Half normal plots

Normal and half normal plots are used to highlight which of the effects are real or just random variation within the system. The coefficient values obtained from the regression statistics are converted to an absolute value and ordered in magnitude. The coefficient values are then plotted against a normal distribution, which is

obtained from determining a half normal score for each coefficient. The next section explains how the half normal scores are obtained.

If the coefficients obtained are just modelling random noise and are in no way related to the response data, then the points on the half normal plot will lie on a straight line. However, active coefficients that relate to variables that have an effect on the response data lie off the general trend of the plot and are called outliers. These points would therefore lie outside the normal distribution and are not the result of random noise.

3.6.4.4 Half normal scores

The standard normal distribution, or normal probability, is described by the probability density function [56] shown in equation 3.4,

$$y = \phi(z) = \frac{1}{\sqrt{2\pi}} e^{-\frac{z^2}{2}} \tag{3.4}$$

where ϕ is the probability density and z is the standard deviation.

The normal probability function has a mean of 0.0 and a standard deviation of 1.0, as shown in figure 3.13. The area under the curve is equal to 1.0.

The expected standard deviation values for a normal distribution are calculated from the probability density function (equation 3.4), provided the divisions of area for the distribution are known. In figure 3.13 the area under the curve has been split in to 7 equal areas (5 x 1/6 th's and 2 x 1/12 th's at the extremes) to provide 3 half normal scores, which are the 3 standard deviations defining the split lines.

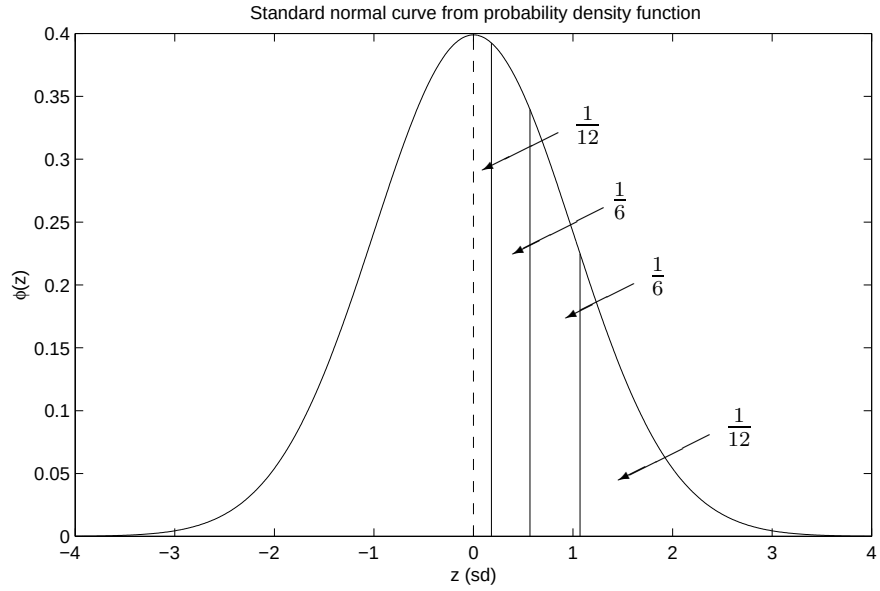

Figure 3.13: The standard normal distribution curve generated from the probability density function. The mean (μ) is 0, the standard deviation (σ) is 1 and the area under the curve is equal to 1 [56, Stroud].

The first score (a_1) is calculated from equation 3.5,

$$\frac{1}{4s} = \int_0^{a_1} \frac{1}{\sqrt{2\pi}} e^{-\frac{z^2}{2}} dz \tag{3.5}$$

and the remaining scores are calculated from equation 3.6,

$$\frac{1}{2s} = \int_{a_{n-1}}^{a_n} \frac{1}{\sqrt{2\pi}} e^{-\frac{z^2}{2}} dz \tag{3.6}$$

where s is the number of half normal scores required, a_n is the n'th half normal score and z is the standard deviation. The central area under the curve is split evenly over the mean so the first half normal score relates to the area under the curve between the mean and the first split line.

The probability density function cannot be integrated by conventional means. Equations 3.5 and 3.6 are solved using an iterative method based on Simpson's rule [56].

3.7 Summary

The gas assisted injection moulding process variables are monitored using suitable transducers and a computer data acquisition system. The process signals that are monitored are screw displacement, hydraulic pressure and gas pressure. A real time calculation of the specific pressure integral during primary melt injection provides and indication of process stability.

The form of the specimen tool provides a long constant section gauge length of rectangular cross section. The design is based loosely around a standard tensile test specimen, but the thick section and introduction of gas far exceeds the standard specifications. The tool has interchangeable inserts that allow the gate system to be changed.

The test specimen is weighed and measured for shrinkage. Subsequently, the specimen is sectioned and scanned for later image analysis to determine the residual wall thicknesses for comparison with simulation.

A design of experiments approach has been used to examine the connection between processing variables and the residual wall thickness observed in the specimens. Multiple regression is used to provide a model relating residual wall thickness to process variable settings.

Chapter 4

Experimental results

4.1 Introduction

The residual wall thickness formed during gas penetration through the polymer melt is influenced by a number of processing variables. The most notable variable is the delay time between the end of polymer melt injection and the start of gas injection. During this period of time the polymer cools at the mould wall, which causes a significant increase in viscosity and the residual wall thickness is increased. Other factors such as gas pressure, melt temperature and mould temperature also influence the residual wall thickness, but to a lesser extent.

The first part of the experimental results chapter examines the general process phenomenon observed through measurement of the process and product. Later in the chapter an empirical model is developed to link the process settings to the residual wall thickness observed in the product. This model will be used to compare against results from the simulation of the cavity filling using the

pseudo-concentration method.

A statistical design of experiments method is used to develop the empirical model. This method is commonly known as Taguchi design of experiments (DoE) [54, 53] after Professor Genechi Taguchi who pioneered the transfer of the method from Japan to the west in the early 1980's [57]. Design of experiments involves the use of fractional factorial arrays to investigate the relationship between a response and factors thought to influence the response. Multiple regression is used to formulate a model of the system that links the responses, in this case wall thickness, to the experimental factors, which are the GAIM processing variables. Normal plots and t-statistics are used to indicate which of the processing variables are influential in determining residual wall thickness and should be included within a regression model. Residuals between the experimentally observed responses and the predicted responses are used to calibrate the accuracy of the model.

4.2 Process control phenomenon

The understanding of the GAIM process is improved by taking measurements of relevant process variables. Process signals from transducers used to measure the process variable show how close the actual signal variable setting differs from the set point, therefore indicating control accuracy and precision. Within this section the melt and gas injection systems are monitored and process phenomenon is revealed that may be linked to variation within the product.

Figure 4.1: The relationship between specimen mass and melt delivery stroke (shot size) at different melt temperatures.

4.2.1 Temperature effects on melt delivery

The preparation of melt during GAIM is identical to the conventional injection moulding process. The quantity of melt delivered into the cavity effects the final position of the gas bubble. The sensitivity of the gas bubble position to melt delivery is related to the cavity geometry.

The melt preparation is controlled by a number of factors. The screw rotation speed, pressure on the screw during metering (back pressure), metering stroke (shot size) and melt temperature. The experimental work presented later in section 4.4 investigates the changes in residual wall thickness upon changes to a number of processing factors. One of the processing factors included within the study is melt temperature.

Figure 4.1 shows the result of a study to determine how the melt temperature

can effect the melt preparation, in particular, the final delivery of melt into the mould measured by recording specimen mass. Figure 4.1 indicates that specimen mass is related to the shot size, which is set directly on the machine controller. This relationship is consistent to within a specimen mass of 0.3g over the recommended processing temperature range of the polymer, which is 210–250°C . Similar tests carried out at a melt temperature setting of 200°C show that the melt delivered into the cavity is significantly lower than if the melt is within the recommended processing temperature range. These data would indicate that the density of the melt is higher within the recommended processing range of 210–250°C than at 200°C .

Once the injection screw has completed preparation of the melt the screw is allowed to move back without rotating to release pressure from the melt. This is termed decompression. A decompression of 1mm is added to the metering stroke here, which prevents pressurised melt from running into the mould during mould opening.

4.2.2 Temperature effects on screw velocity

The setting for screw velocity is specified as a percentage of the maximum available velocity, which is 106mm/s. The actual velocity of the screw during injection of the melt is dependent upon the melt temperature. There is clearly a link between the melt temperature and melt viscosity, which impacts upon the necessary injection pressure.

Figures 4.2 to 4.4 show how the actual screw velocity lags behind the set point.

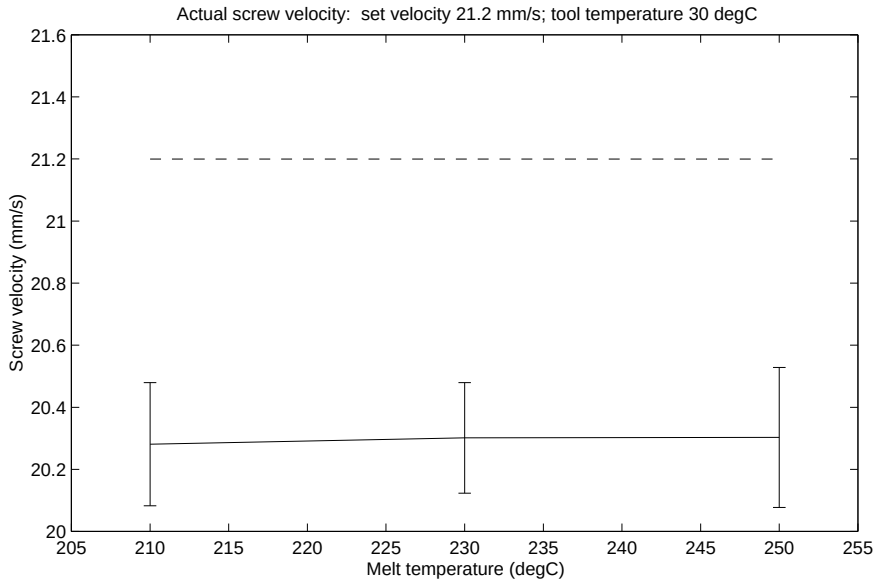

Figure 4.2: Screw velocity set point 20% (21.2mm/s).

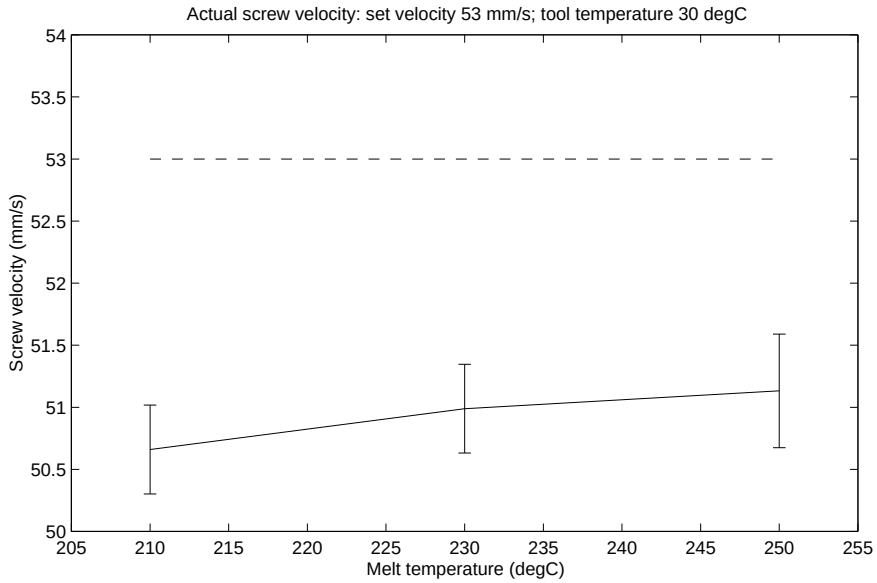

Figure 4.3: Screw velocity set point 50% (53.0mm/s).

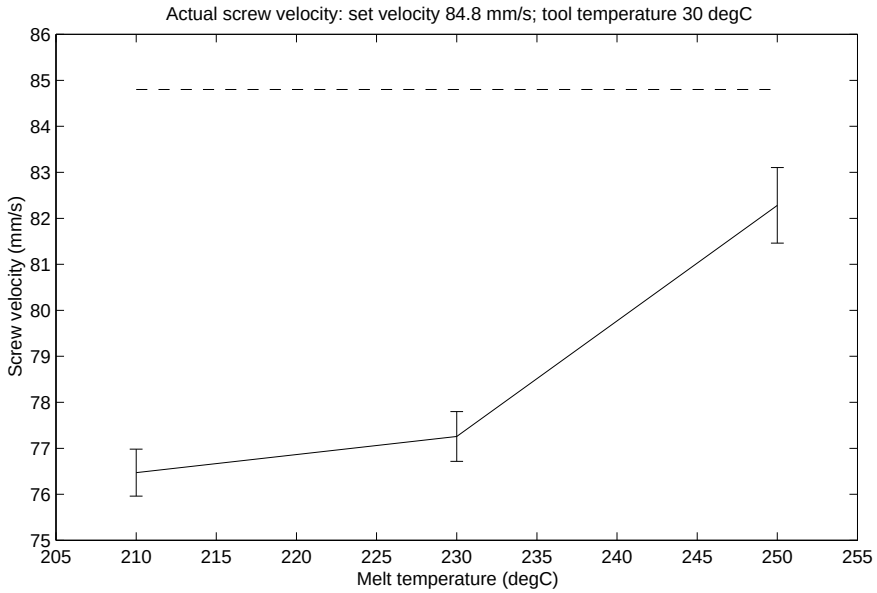

Figure 4.4: Screw velocity set point 80% (84.8mm/s).

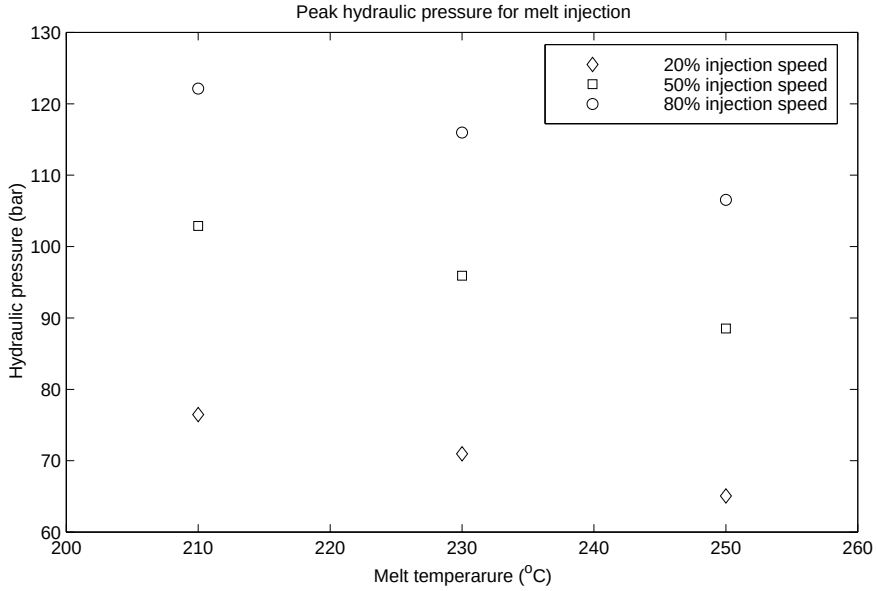

Figure 4.5: The peak hydraulic pressure during primary injection is effected by the velocity and the melt temperature.

Error bars are $\pm\sigma$ and show the variation in the velocity over 10 samples. In conjunction with the screw velocity data the maximum hydraulic pressure during the velocity controlled phase is shown in figure 4.5. This shows the peak pressure for a range of screw velocity settings and melt temperatures. The maximum hydraulic pressure available to the melt injection unit is 140 bar.

The magnitude of the screw velocity lag at each set point depends upon the melt temperature. At the lowest velocity setting of 20% (figure 4.2 the actual velocity only lags by approximately 1mm/s and does not improve significantly with an increase in melt temperature. The required hydraulic pressure is less than 80 bar at the lowest melt temperature and decreases to 65 bar at the highest melt temperature.

At the highest velocity setting of 80% (figure 4.4) the screw velocity lag is approximately 8mm/s when the melt temperature is at the lowest setting and approximately 2.5mm/s at the highest melt temperature setting. The required hydraulic pressure (figure 4.5) is close to the maximum available from the system when the melt temperature is at 210°C .

4.2.3 Off-line gas injection investigations

The gas needle design is inherited from the design of the Battenfeld gas needle. Openings 25μm deep allow the pressurised gas to escape into the polymer melt. The openings are small enough to prevent melt from entering the needle and causing a blockage. The gas needle has a central pin with flats that allow gas to travel to the head, were it is allowed to escape from under the head of the central

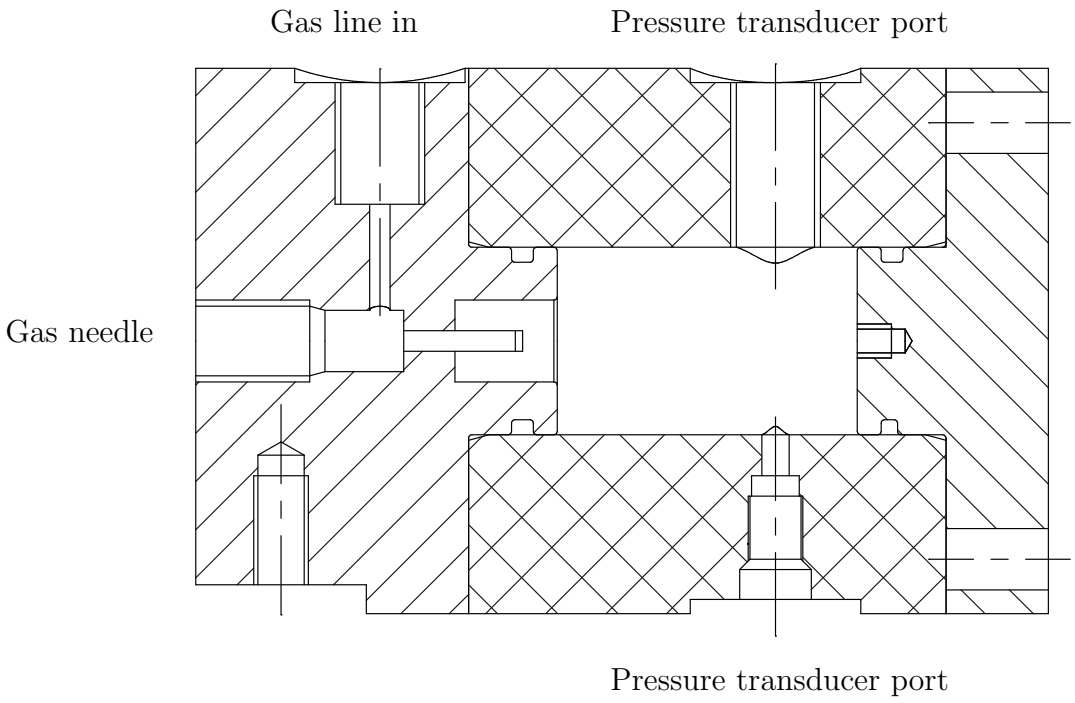

Figure 4.6: Pressure chamber for gas needle investigations.

pin.

A chamber for the gas needle is available in order to understand better the flow of nitrogen gas through the needle and into the melt during primary injection. This is an off-line test that monitors the pressure increase within a closed volume to line pressure. The volume of the chamber is approximately 1.4 times that of the tensile test specimen cavity. The design of the gas chamber is shown in figure 4.6 The gas needle can be mounted in the end cap and supplied with nitrogen gas. The supply pressure is monitored by the pressure transducer used to monitor the gas pressure in the process. The pressure in the gas chamber is monitored with a second pressure transducer. Both signals are logged through the LabVIEW data

acquisition system.

Figures 4.7a and 4.7b show the gas pressure build up within the gas chamber from two different gas needle configurations. Firstly, the central pin is removed from the needle. This configuration would indicate how much resistance to flow exists within the body of the needle without the influence of the pin restriction. Secondly, the central pin is fitted and the gas can only escape into the chamber through the openings under the head of the central pin.

For the case of the open gas needle the pressure rise within the gas chamber closely follows the line pressure. This indicates that the inherent resistance to flow within the body of the gas needle is insignificant. Where the central pin is in place the chamber pressure displays a significant lag behind the line pressure. The rise time of the chamber pressure to line pressure is approximately 1.5 seconds. Clearly within the process this rise time may not be directly applicable since the gas bubble volume is constantly changing during primary injection. The off-line test indicates that the gas pressure driving the bubble penetration may be lower than the set pressure.

An interesting feature of the line pressure signal is that it is comparatively unstable while the chamber pressure is still rising and only settles once the chamber pressure has reached line pressure. This indicates that while gas is flowing through the needle the line pressure signal displays some instability. This instability is observed within the process and may indicate when the bubble pressure has reached the line pressure.

The ideal gas law was used to estimate the mass flow rate of gas through

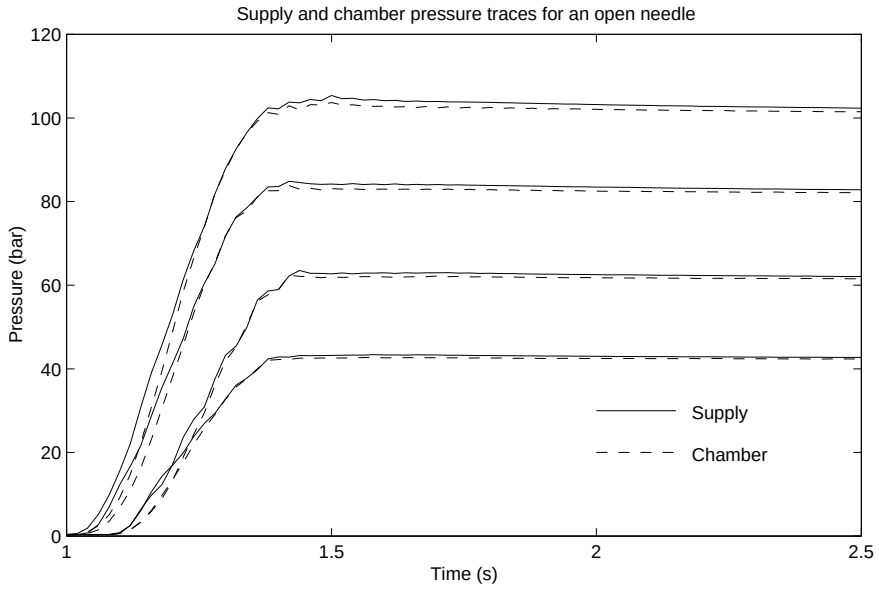

(a) Open needle

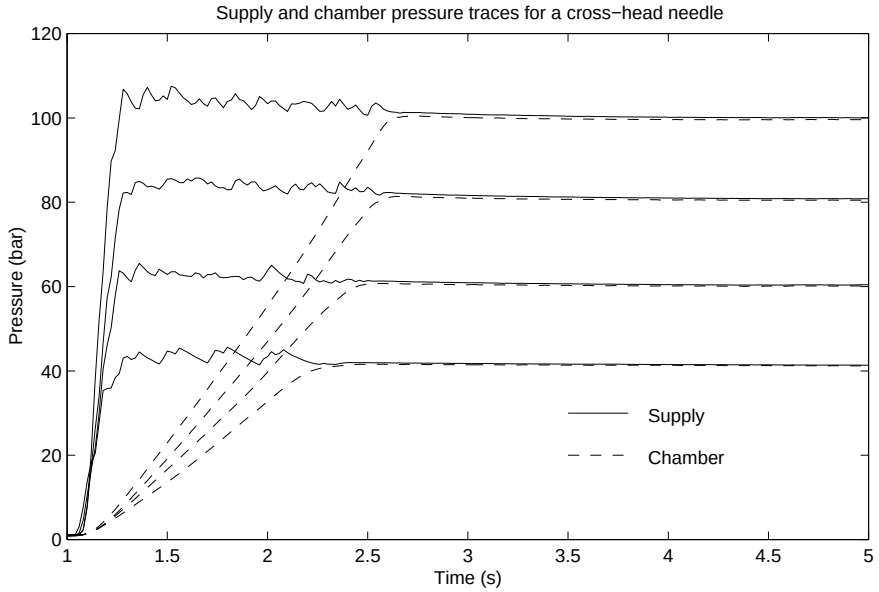

(b) Cross head needle

Figure 4.7: Line pressure and chamber pressure development over time for line set pressures of 40, 60, 80 and 100 bar

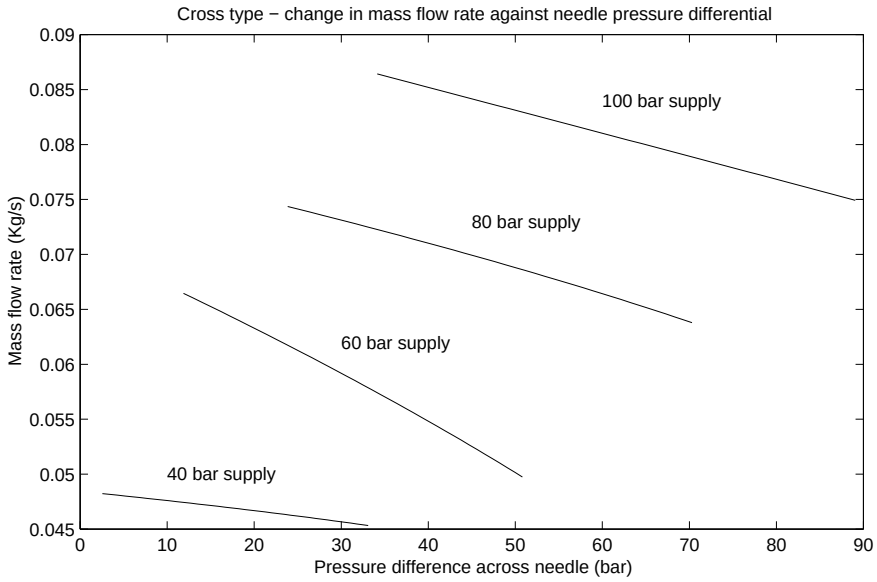

Figure 4.8: Calculation of mass flow rate through the gas needle using the ideal gas law.

the needle during injection into the chamber. The ideal gas law is shown in equation 4.1

$$PV = nRT \tag{4.1}$$

where, P is pressure (chamber pressure), V is volume (chamber volume), n is the number of moles of gas present, R is the universal gas constant and T is the gas temperature measured in Kelvin.

The relationship between the number of moles of nitrogen gas present within the chamber volume and the measured chamber pressure is the basis upon which the mass flow rate of gas into the chamber is calculated. This approach is simplistic and relies upon the temperature of the gas remaining constant. Normal room temperature (20°C) is taken as the gas temperature.

Figure 4.8 shows the calculated mass flow rate through the gas needle using

the ideal gas law equation. Mass flow rate is plotted against the pressure difference across the gas needle, which is the difference between the line and chamber pressures. The mass flow and pressure difference relationship is calculated at the different set line pressures. Since the calculated mass flow appears to be significantly line pressure dependent the adiabatic treatment of the gas flow is not sufficient to provide an accurate estimate. The direct measurement of mass flow rate using a flow meter for example is not possible since the time scale over which the mass flow rate changes is too short.

4.3 Experimental investigations on the tensile specimen

This section will present some of the phenomena associated with the GAIM process. These data assist in making the decision over which of the processing parameters to include within the empirical model experiment.

4.3.1 Differential wall thickness due to shear heating

In conventional injection moulding a small gate is typically between the runner system and the cavity that forms the product. The small gate allows the runner system to be separated from the product easily, either during or after ejection from the mould. GAIM can use a small gate to prevent the gas bubble penetrating into the runner system. Figure 4.9a shows the "tab" gate configuration between the runner system and the tensile test bar cavity. The gas needle is shown protruding

into the cavity. When the fixed and moving halves of the mould are brought together the gap between the tab gate and the fixed half of the mould is 25μm.

Since the polymer melt is forced through a small gap a significant amount of shear heating is thought to take place. Evidence of the shear heating is seen in the wall thickness differential between the fixed and moving platen. Figure 4.10 shows that the wall thickness at the fixed wall is consistently thinner than the wall at the moving platen and a difference in wall thickness of 0.2mm is typical. A range of gas pressures (40–100 bar) are used to check that this trend is consistent. The tab gate may cause a temperature gradient across the melt that increases from the moving to the fixed side of the mould (i.e. toward the tab gate side of the mould). The temperature gradient would therefore effect the position of the bubble within the section.

To contrast the effect of the tab gate an insert with the tab gate removed provides an open channel between the specimen and the runner. Figure 4.9b shows the mould configuration without the tab gate in place. The differential between wall thickness against the fixed and moving platens is significantly reduced. The average wall thickness over 18 experimental runs shows a difference of 0.03mm, which is taken from section 4.4. This comparison indicates that the tab gate does effect the wall thickness distribution across the section.

The absence of the tab gate requires the gas injection nozzle with the non-return valve to be fitted to the end of the machine barrel. The gas is free to penetrate the runner system and will enter the machine barrel unless prevented from doing so by the non-return valve.

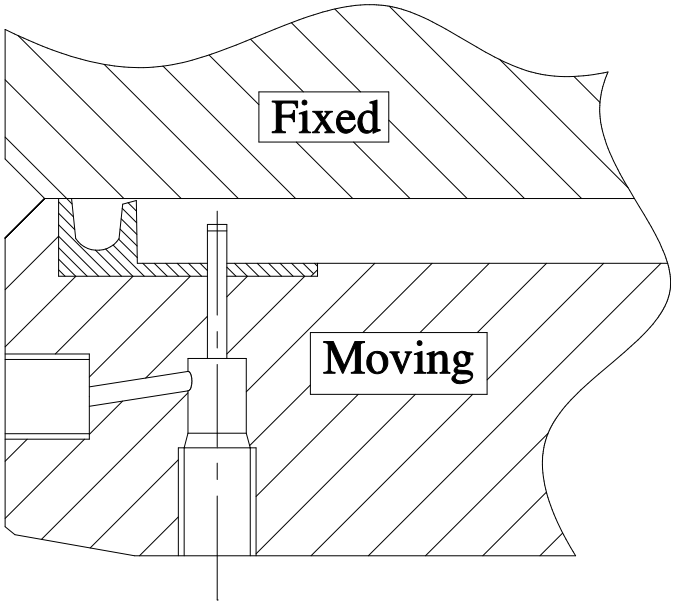

(a) Tab gate in place

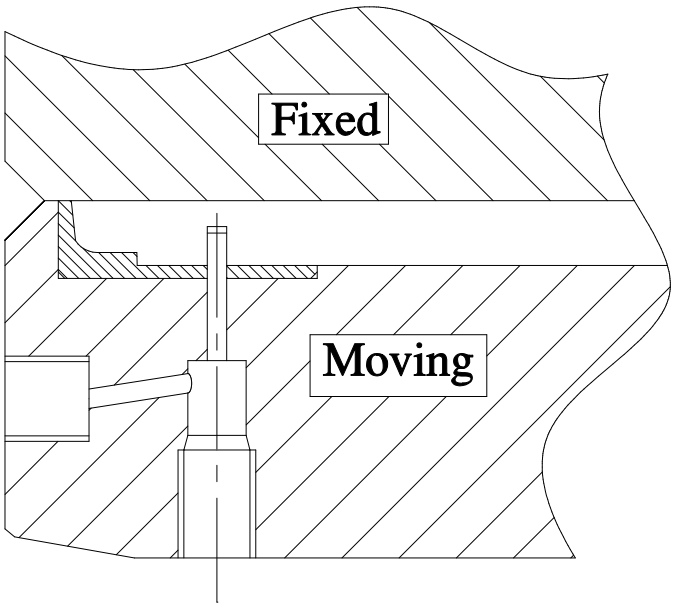

(b) Open channel to specimen

Figure 4.9: The tensile specimen with a tab gate and open channel.

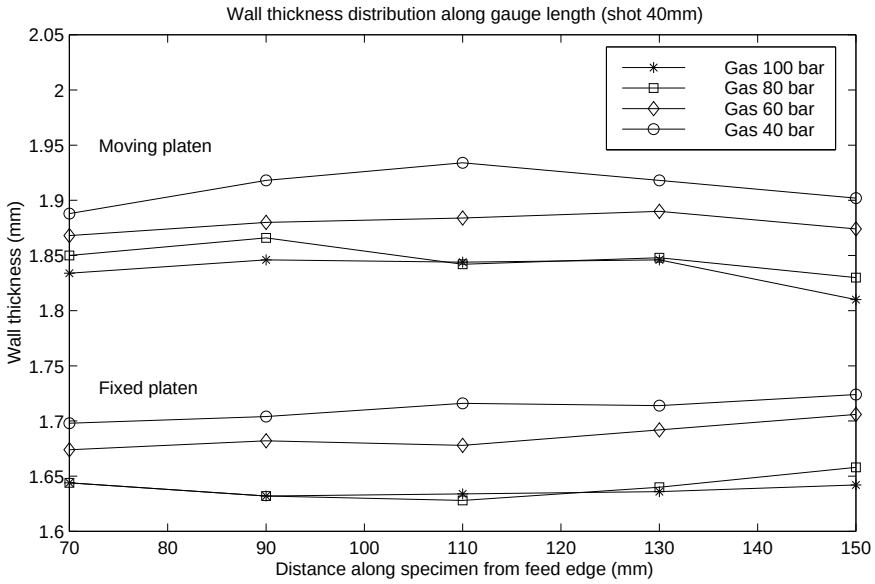

Figure 4.10: Differential wall thickness between the fixed and moving platens due to the tab gate. The wall thickness is within a 2.5% variation along the gauge length

4.3.2 Gas pressure effects on residual wall thickness

The gas pressure setting during primary gas injection influences the residual wall thickness. Generally, increasing gas pressure causes a reduction in the wall thickness. This trend has been observed by other authors using Newtonian and Boger fluids [13, 11, 14, 15, 16] where the increasing capillary number moves the residual wall thickness toward an asymptotic value.

Figure 4.11 shows that wall thickness tends to decrease as the gas pressure is increased. However, the correct measurement of specimens formed using a gas above 100bar is difficult because blisters on the internal wall and trapped pressurised gas bubbles. The reduction in wall thickness over the 40 to 100bar range is approximately 4%, where the melt temperature is 190^{o}C .

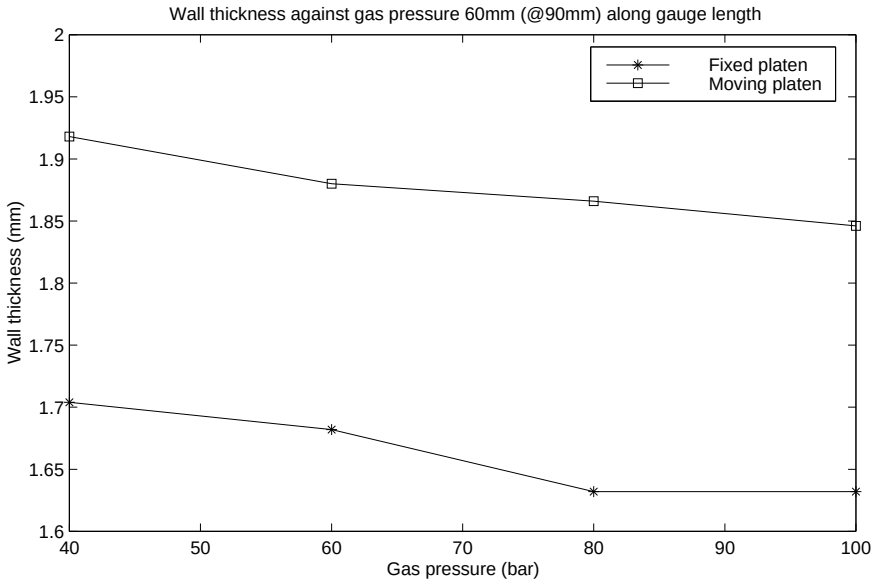

Figure 4.11: Wall thickness decreases with increasing gas pressure. Measurements are taken 60mm along the gauge length from the gas needle.

The reduction in wall thickness means that more material is pushed ahead of the gas bubble as the gas pressure is increased. Therefore, the gas bubble penetration also reduces with increasing gas pressure.

4.3.3 Gas pressure effects on specimen shrinkage

Packing pressure to the specimen can be maintained for most of the cooling phase with GAIM. This is an advantage over conventional injection moulding where the gate freeze time limits how long the packing pressure is maintained for.

Specimen section shrinkage can be measured by comparing the specimen depth dimension to the dimension of the cavity used to form the respective dimension. Figure 4.12 shows the calculated shrinkage of the overall section in two regions. Firstly, before the bubble tip where the cross section is hollow and secondly

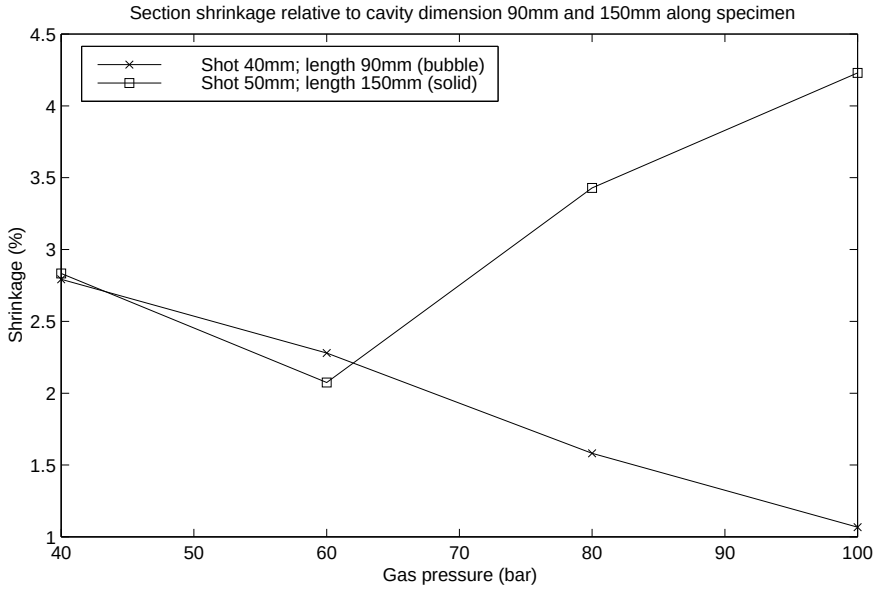

Figure 4.12: Comparison of section shrinkage before (90mm) and after (150mm) the bubble tip, which are hollow and solid sections respectively.

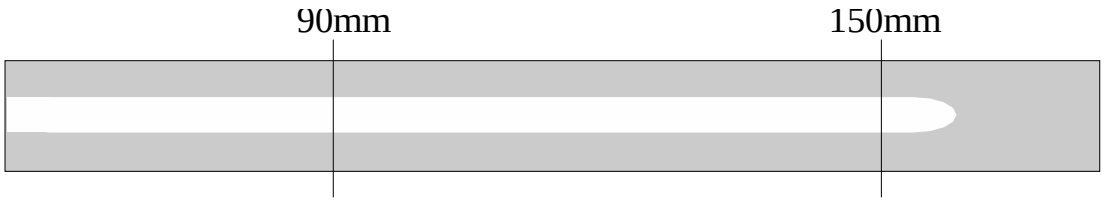

(a) Low gas pressure

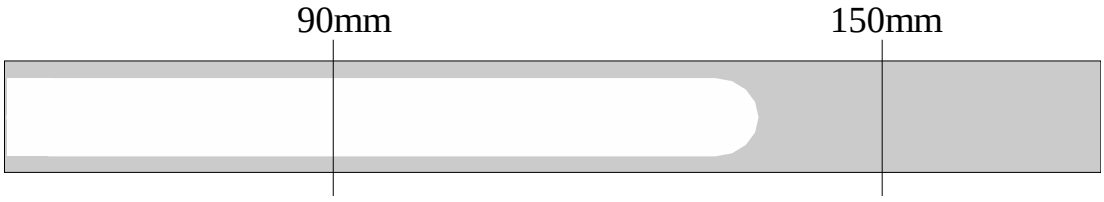

(b) High gas pressure

Figure 4.13: Measurement locations for section shrinkage. Bubble penetration reduced with increased gas pressure

after the bubble tip where the cross section is solid. Since the bubble penetration reduces as the gas pressure increases the bubble tip position relative to the 150mm measurement position changes from just after to just before, relating to hollow and solid sections respectively. Figure 4.13 is a schematic to illustrate this phenomena.

The cross section shrinkage reduces as the gas pressure is increased during the cooling phase. The shrinkage at a hollow cross sections is as low as 1% where the gas pressure is 100bar. However, as the gas bubble tip moves back the section at the 150mm position becomes solid. Shrinkage of a solid cross section is significantly increased, even though a high gas pressure is maintained further up-stream. The respective shrinkage of the solid cross-section is 4.25% at 100bar gas pressure.

4.4 An empirical model to describe residual wall thickness

A model based on experimental data will describe the residual wall thickness. The inputs to the model are processing parameter settings, such as melt temperature and gas delay time. The output from the model is residual wall thickness. A model is produced for each of the four walls along the centrelines of the cross section.

The formation of the residual wall in GAIM is clearly influenced by the processing conditions. An investigation to determine and rank the influence of processing parameters on residual wall formation follows a design of experiments

procedure. The experimental array used allows upto 8 parameters to be studied. The first of the 8 parameters is studied at two levels and the remaining parameters at 3 levels. This array does not exhibit interaction columns, which avoids the issue of confounding.

4.4.1 Parameters

The 6 processing parameters are included in the experiment and are summarised in table 4.1 along with the respective units of measurement. Each parameter occupies 1 column of the available 8 within the experimental matrix, which is shown in table 4.2.

The STT is the setting seen on the water heater/cooler attached to the mould. The SMT relates to the setting of the heater bands on the injection moulding machine barrel. IV is the speed at which the injection screw in the barrel covers the melt delivery stroke. This is a percentage of the maximum the machine can achieve, which is $106mms^{-1}$ [43]. The GP is a single stage injection of gas to a set point. The gas delay is measured between the gas trigger signal and the injection of gas. GT is the position of the screw when the IMM controller signals a trigger to the gas controller.

4.4.2 Experimental array

The array in table 4.2 has 18 separate experimental runs. The settings for the parameters under investigation are indicated by the setting code in each relevant column. This array can be used to study upto 8 parameters. The L18 array

Abbreviation	Definition	
STT	Set Tool Temperature	(°C)
SMT	Set Melt Temperature	(°C)
IV	Injection Velocity	(%)
GP	Gas Pressure	(Bar)
GD	Gas Delay	(Sec)
GT	Gas Trigger	(mm)

Table 4.1: Definition of abbreviations used for parameters

	Main Factors								Quadratic and interactions						
RUN	**STT**	**SMT**	**IV**	**GP**	**GD**	**GT**	**e1**	**e2**	**SMTq**	**IVq**	**GPq**	**GDq**	**GTq**	**STTx SMT**	**STTx SMTq**
1	−1	−1	−1	−1	−1	−1	−1	−1	1/3	1/3	1/3	1/3	1/3	1	− 1/3
2	−1	−1	0	0	0	0	0	0	1/3	− 2/3	− 2/3	− 2/3	− 2/3	1	− 1/3
3	−1	−1	1	1	1	1	1	1	1/3	1/3	1/3	1/3	1/3	1	− 1/3
4	−1	0	−1	−1	0	0	1	1	− 2/3	1/3	1/3	− 2/3	− 2/3	0	2/3
5	−1	0	0	0	1	1	−1	−1	− 2/3	− 2/3	− 2/3	1/3	1/3	0	2/3
6	−1	0	1	1	−1	−1	0	0	− 2/3	1/3	1/3	1/3	1/3	0	2/3
7	−1	1	−1	0	−1	1	0	1	1/3	1/3	− 2/3	1/3	1/3	−1	− 1/3
8	−1	1	0	1	0	−1	1	−1	1/3	− 2/3	1/3	− 2/3	1/3	−1	− 1/3
9	−1	1	1	−1	1	0	−1	0	1/3	1/3	1/3	1/3	− 2/3	−1	− 1/3
10	1	−1	−1	1	1	0	0	−1	1/3	1/3	1/3	1/3	− 2/3	−1	1/3
11	1	−1	0	−1	−1	1	1	0	1/3	− 2/3	1/3	1/3	1/3	−1	1/3
12	1	−1	1	0	0	−1	−1	1	1/3	1/3	− 2/3	− 2/3	1/3	−1	1/3
13	1	0	−1	0	1	−1	1	0	− 2/3	1/3	− 2/3	1/3	1/3	0	− 2/3
14	1	0	0	1	−1	0	−1	1	− 2/3	− 2/3	1/3	1/3	− 2/3	0	− 2/3
15	1	0	1	−1	0	1	0	−1	− 2/3	1/3	1/3	− 2/3	1/3	0	− 2/3
16	1	1	−1	1	0	1	−1	0	1/3	1/3	1/3	− 2/3	1/3	1	1/3
17	1	1	0	−1	1	−1	0	1	1/3	− 2/3	1/3	1/3	1/3	1	1/3
18	1	1	1	0	−1	0	1	−1	1/3	1/3	− 2/3	1/3	− 2/3	1	1/3

Factor settings

−1	30	210	20	30	0	0.2	−	−
0	−	230	50	55	5	0.6	−	−
+1	60	250	80	80	10	1.0	−	−

Table 4.2: The experimental array and factor settings.

can only be used to study interactions between columns 1 and 2. The interaction pattern between other columns is complex, which minimises the effect of confounding [53].

The settings for the parameters that relate to the code are shown in the box under the experimental array. The codes for the parameter settings are chosen to be -1, 0 and +1 to represent the levels of each parameter. This coding system is useful for the generation of the interaction columns and simplification of subsequent analysis.

So, for example, in run 6, the STT is at setting -1, which corresponds to 30°C . SMT is at setting 0, which corresponds to 230°C . IV is at setting 1, which corresponds to 80%. The pattern continues for GP, GD and GT in the next 3 columns. The 2 empty columns, marked e1 and e2, do not have any associated settings. They are checking columns used to monitor the effect of changing nothing at all in the experiment.

4.4.3 Parameter settings

Generally, the range of the parameter set values in an experimental study like this is as wide as possible in order to generate the widest possible process map. However, if the relationship between the processing parameter and the response, in this case wall thickness, is not linear then the range needs at least 3 equally spaced set points to detect non-linearity. The range of the parameters is a compromise between the desired range and the ability for the process to manufacture suitable specimens at extremes of the parameters settings.

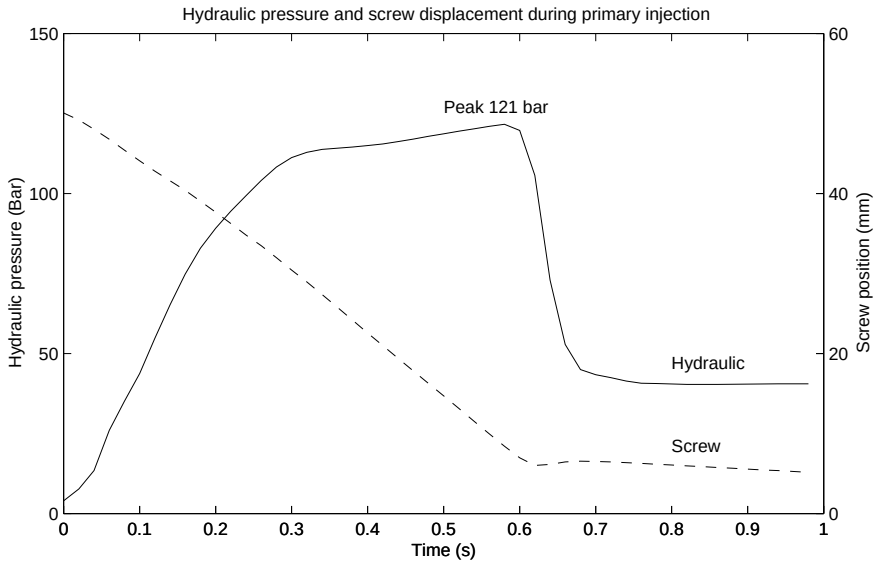

Figure 4.14: Hydraulic pressure trace from run 3 of the experimental array. The maximum available hydraulic pressure on the CDK750 is 140 bar. The corresponding screw displacement is shown dotted.

The recommended processing conditions for the material (HDPE) taken from the manufacturers data sheets [58] and the Moldflow material database [59] are used as a starting point. The recommended processing temperature range of the material is 210°C to 250°C . The recommended tool temperature range is 30°C to 60°C .

A percentage of the maximum injection velocity is used as a set point on the machine control system. Therefore the range is from 0 to 100%. The maximum setting for injection velocity was determined by examining the hydraulic pressure profile during primary injection and considering the maximum available pressure from the machine for this phase. The demand for hydraulic pressure during primary injection will be greatest when the melt temperature and tool temperature are at their lowest settings. This is because the resistance to melt flow is greatest.

This situation exists in experimental run number 3, seen in table 4.2, were the set values for STT, SMT and IV are -1, -1 and +1 respectively.

Figure 4.14 is a hydraulic pressure trace during primary injection taken from run 3 of the experimental array. The peak pressure is 121 bar, which is 14% lower than the maximum available hydraulic pressure of 140 bar. The setting on the controller was at 80% here. The maximum of the injection velocity range is 80% to compromise between maximising the range for the experiment and leaving a margin between the limit of the machine. The minimum of the injection velocity is set at 20% to put the range in the middle of the maximum range available.

The gas delay time range is limited by total solidification of the melt before gas injection. A delay time of 10 seconds was found to significantly increase the wall thickness, but not to the point where the gas bubble needs more than 30 bar gas pressure to form the specimen. The tool temperature, melt temperature and injection velocity are at their lowest settings for determining the maximum delay time. The minimum delay time is set to 0 seconds.

The gas pressure range is determined from inspection of the specimens. The lowest feasible gas pressure just forms a specimen when the resistance to formation is greatest. This greatest resistance to formation under gas pressure is when the tool temperature, melt temperature and injection velocity are lowest and the gas delay time is highest. 30 bar provides just enough pressure to form the specimen under these conditions. The highest gas pressure is well below the maximum available, which is 350 bar. High gas pressure for primary gas penetration can lead to problems such as blistering and trapped pockets of pressurised gas that

cause the specimen to burst on ejection from the mould. Measurements cannot be taken from a specimen that is deformed. The highest melt temperature and lowest delay time were the conditions at which high gas pressure during primary gas bubble penetration caused problems. The highest limit of gas pressure is 80 bar.

The trigger for the gas injection control unit is sent from the injection moulding machine controller when the screw displacement reaches a set value. The range of trigger value is limited by the requirement for melt flow near the gas needle to be stationary before gas is injected. Again, pockets of pressurised gas and blow through occur if the gas is injected before the melt has stopped flowing. A range of 0.8 mm doesn't provide any problems with the specimens, irrespective of location within the stroke.

4.4.4 Constant parameter settings

The remaining injection moulding machine settings for the manufacture of the specimens were kept constant. Only the process parameters in the experimental array are changed during specimen manufacture. The main profiles involved in manufacturing the test specimens are melt injection, hold (packing) pressure, gas injection and melt preparation.

The basic injection velocity profile is shown in figure 4.15. The melt preparation phase rotates the screw until the screw position is at 45.5mm. A decompression of 1mm draws back the screw, without any rotation, to a position 46.5mm, which is the start position for the injection of melt into the cavity. The injection

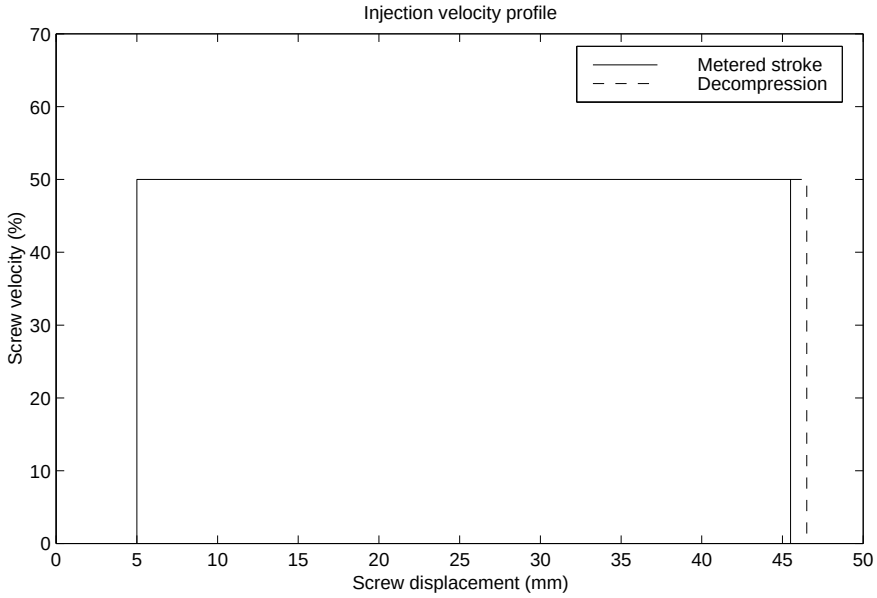

Figure 4.15: A screw velocity profile for primary injection. Decompression of 1mm after metering.

profile is a single phase that specifies a velocity (IV) for the screw to travel until the switch-over position is reached. In this case the switch-over position is 5mm.

The switch-over signal initiates the hold pressure profile, shown in figure 4.16. The purpose of the hold pressure is to push the remaining melt into the cavity, resulting in the screw reaching the end of the barrel (bottoming out). The switch from velocity to pressure control is completed before the end of the barrel to prevent damage to the screw tip. The purpose of the first hold pressure stage (50 bar) is to ensure a consistent delivery of melt into the cavity. The second stage of hold pressure (30 bar) is used to prevent melt from being pushed out of the cavity by the gas pressure. The non-return valve in the gas nozzle should also ensure this doesn't happen. The intensification ratio between the hydraulic and barrel pressures is 11.25, so 30 bar hydraulic provides 337.5 bar inside the barrel. That

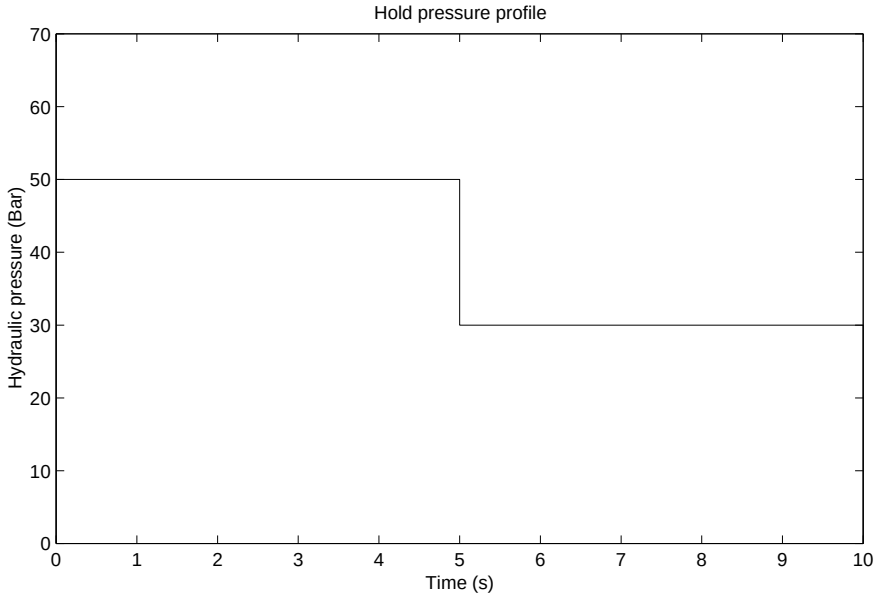

Figure 4.16: A hold pressure profile that is initiated after switch-over.

pressure is well above the maximum 80 bar gas pressure used in the experiment.

The gas pressure profile is a simple single stage and is shown in figure 4.17. Gas injection starts after the delay time. A trigger signal from the IMM controller starts the delay time counter. The trigger signal is initiated when the screw position reaches a set value. The delay time range is 0 to 10 seconds, noted previously. Next the gas is injected directly to the set pressure and maintained for 5 seconds. This is long enough for the gas bubble to form, but doesn't deplete the receiver pressure too much if gas blow through should occur. After the primary gas injection stage the gas bubble is sealed by closing all of the inlet and outlet valves for 20 seconds. During this time the melt is cooling and shrinks. The gas bubble expands into the shrinking melt resulting in a gradual gas pressure decay of the bubble. The gas is released after the 20 seconds.

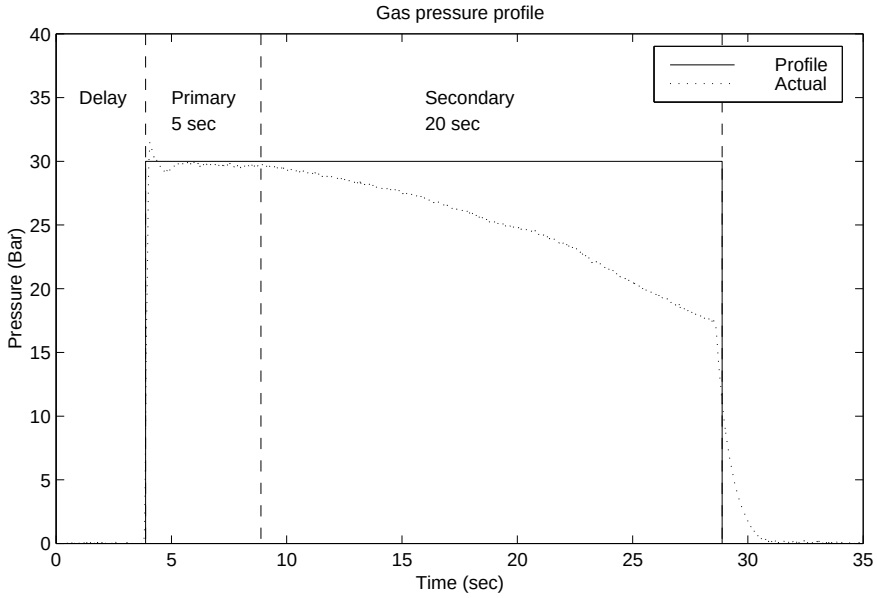

Figure 4.17: A gas pressure profile. The primary phase maintains pressure and secondary phase closes all gas valves

4.4.5 Experimental data

The multiple regression analysis correlates processing factor settings to residual wall thickness along the specimen gauge length. The processing factors have assigned to them regression coefficients and the wall thickness is the response variable.

4.4.5.1 Measured wall thickness results

The wall thickness is measured along the central axis of a cross section using the image analysis technique outlined in section 3.5.2. Cross sections from three specimens are measured to obtain an average wall thickness. The results for each experimental run are shown in table 4.3 and the mean wall thickness over all runs is termed $\bar{y}$. Wall thickness results for the fixed and moving platen walls are

Run	FIXED	MOVING	Average LHS RHS	Average FIX MOV
1	1.67	1.72	2.82	1.69
2	1.92	2.01	2.94	1.96
3	2.12	2.10	3.26	2.11
4	1.99	2.03	3.02	2.01
5	2.12	2.16	3.02	2.14
6	1.50	1.54	2.44	1.52
7	1.77	1.81	2.71	1.79
8	1.92	1.91	2.77	1.91
9	2.13	2.20	2.87	2.17
10	2.13	2.13	3.16	2.13
11	1.61	1.65	2.59	1.63
12	1.86	1.89	2.94	1.88
13	2.12	2.03	3.11	2.08
14	1.45	1.54	2.66	1.50
15	1.88	1.95	2.86	1.91
16	1.85	1.89	3.04	1.87
17	2.19	2.15	2.92	2.17
18	1.47	1.45	2.28	1.46
$\bar{y}$	1.87	1.90	2.86	1.89

Table 4.3: The measured residual wall thickness for each experimental run. $\bar{y}$ is the mean wall thickness over all 18 runs

listed separately. However, loss of orientation for the left and right hand walls during sectioning requires the average of the two walls to be taken and used as the response. The average between the fixed and moving platen walls is also listed and a regression analysis is completed on this data.

A response table is constructed from the wall thickness data to show the effect that each processing parameter setting has on the residual wall thickness. Analysis of means (ANOM) is used to calculate the average wall thickness over the factor settings at each level and the results are shown in table 4.4. Note that tool temperature (STT) only has 2 responses because it only has 2 possible levels,

Wall		STT	SMT	IV	GP	GD	GT	e1	e2
	-1	1.90	1.89	1.92	1.91	1.58	1.88	1.85	1.86
FIXED	0		1.84	1.87	1.88	1.90	1.85	1.90	1.85
	+1	1.84	1.89	1.83	1.83	2.13	1.89	1.87	1.90
	-1	1.94	1.92	1.94	1.95	1.62	1.87	1.90	1.89
MOVING	0		1.88	1.90	1.89	1.95	1.89	1.93	1.89
	+1	1.85	1.90	1.86	1.85	2.13	1.93	1.86	1.92
Average	-1	2.87	2.95	2.98	2.85	2.58	2.83	2.89	2.82
LHS RHS	0		2.85	2.82	2.83	2.93	2.82	2.84	2.83
	+1	2.84	2.76	2.77	2.89	3.06	2.91	2.84	2.92
Average	-1	1.92	1.90	1.93	1.93	1.60	1.87	1.87	1.88
FIX MOV	0		1.86	1.89	1.88	1.93	1.87	1.91	1.87
	+1	1.85	1.89	1.84	1.84	2.13	1.91	1.87	1.91

Table 4.4: Response table of factor effects on wall thickness.

all other factors have 3 possible settings.

The response table is represented graphically using effects plots shown in figures 4.18 to 4.21. The effects plot is a simple representation of the response data to help with understanding of the system. For each factor the average response at each setting response is plotted. In each of the plots gas delay time (GD) has the largest effect on wall thickness. Since the factor is tested at 3 levels any non-linearity within the response can be seen. The response at level 0 causes a kink in the response curve and shows the quadratic nature of the effect upon the response.

4.4.5.2 Regression analysis

A multiple regression is carried out for each of the wall thickness responses: fixed, moving, average LHS RHS and average fixed moving. The regression variables are each of the main factors plus the quadratic and interaction variables derived

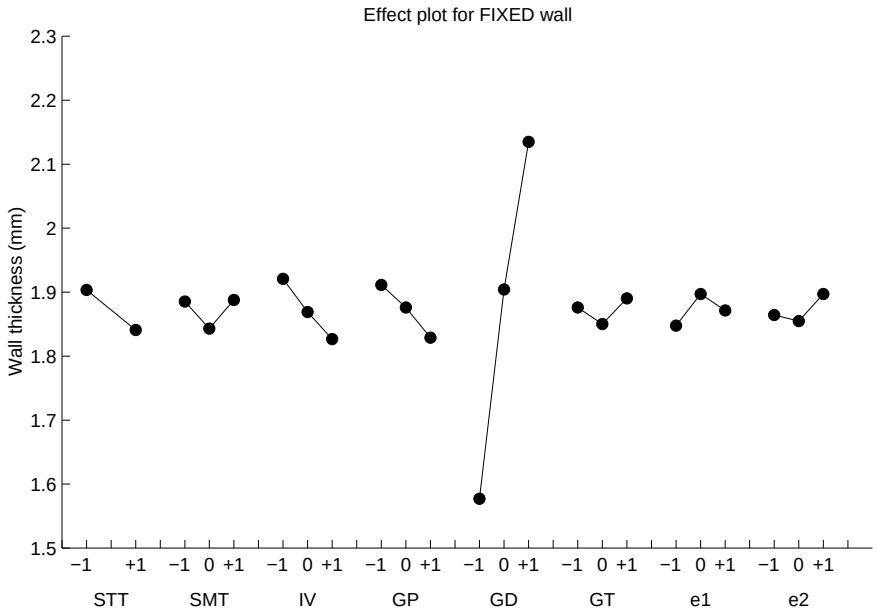

Figure 4.18: Effect of factor settings on FIXED wall.

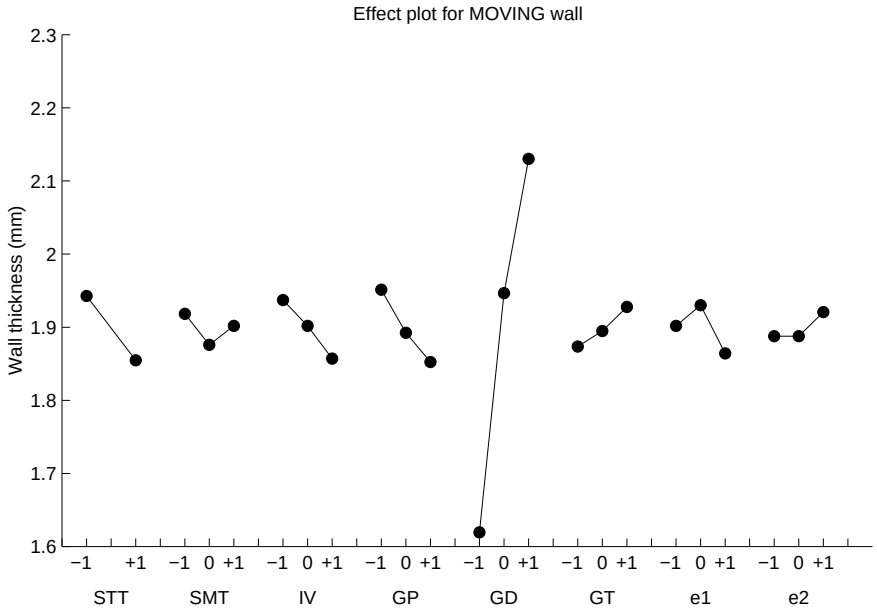

Figure 4.19: Effect of factor settings on MOVING wall.

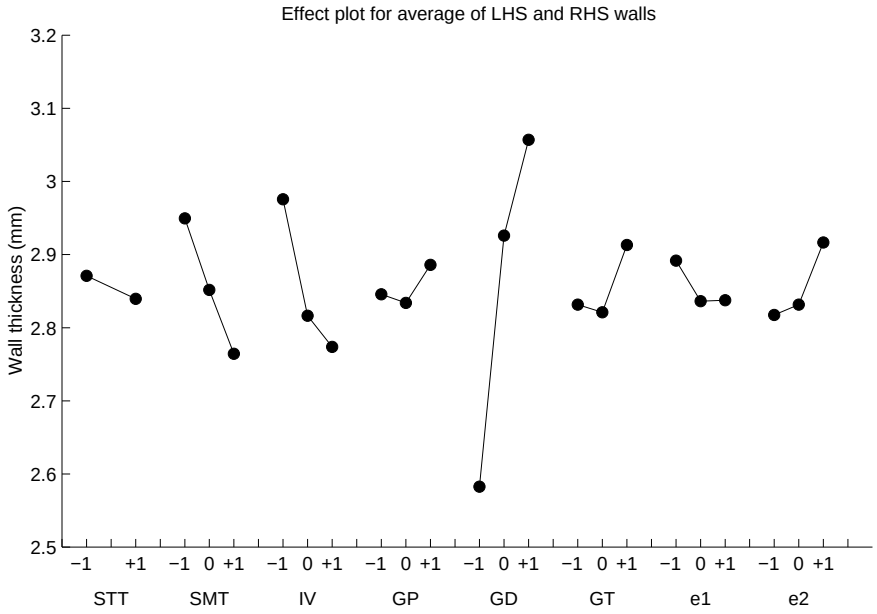

Figure 4.20: Effect of factor settings on the average LHS RHS walls.

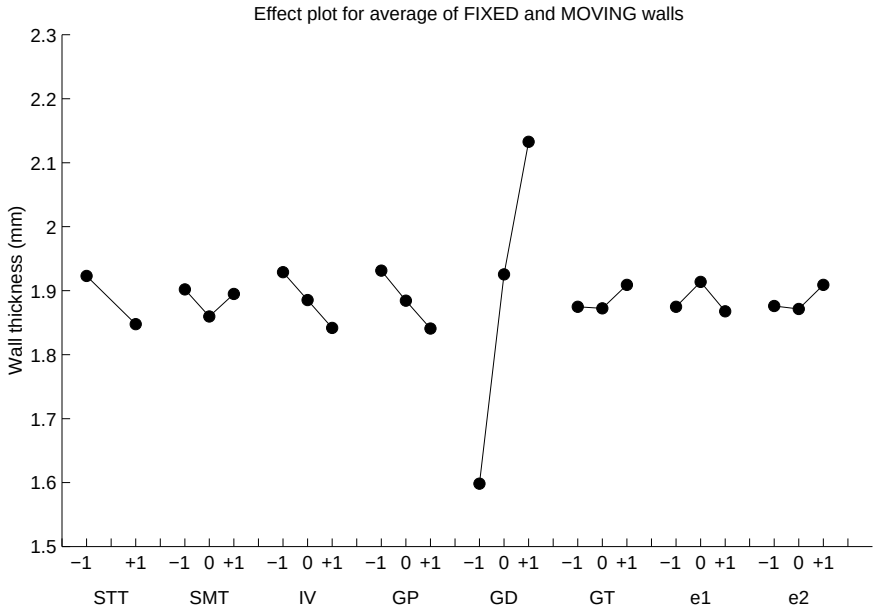

Figure 4.21: Effect of factor settings on the average FIXED and MOVING walls.

from the main factors. A total of 15 regression coefficients are obtained. The multiple regression output is tabulated for each response in figures 4.22 to 4.25. Each regression coefficient (*coeff*) has a t-statistic (*t-stat*) and probability value (*P-value*) to assist in judging the significance of the coefficient. The coefficients are listed in order of absolute magnitude, which is convenient for comparison with the half-normal plots that also assist in judging the significance of the coefficients.

The R^2 value indicates how well the regression equation fits the experimental data points, a value of 1.0 is the best fit. However, since noise exists within the data a perfect fit is not necessarily desirable.

The half-normal plots indicate the relationship between the coefficients and a normal probability distribution and are also shown in figures 4.22 to 4.25. The dotted line is the trend of coefficients that are considered in-active and fit the normal probability distribution. The largest absolute coefficient values are always on the right hand side of the half normal plot. Points lying off the trend line are called outliers and don't fall within the normal distribution. Therefore, the outliers refer to factors that actively influence the response data.

The most significant outliers in all wall thickness responses are gas delay time (GD) and the quadratic of gas delay (GDq), which is the non-linearity within the effect of gas delay time. The normal plots indicate that the gas delay time is a significant factor and should be included within the regression equation. In order to determine which of the other factors must also be included within the regression equation the regression statistics are inspected.

The t-statistic indicates the ratio between the coefficients value and the stan-

Factor	Coeff	Std. err	t-stat	P-value
Intercept	1.8721	0.0152	122.8913	0.0001
SMT	0.0012	0.0187	0.0634	0.9552
IVq	0.0047	0.0323	0.1460	0.8973
GPq	-0.0059	0.0323	-0.1821	0.8723
GT	0.0071	0.0187	0.3788	0.7413
STTx SMTq	-0.0083	0.0323	-0.2553	0.8223
e1	0.0118	0.0187	0.6302	0.5929
e2	0.0165	0.0187	0.8830	0.4704
STTx SMT	-0.0177	0.0187	-0.9469	0.4436
STT	-0.0314	0.0152	-2.0602	0.1756
GTq	0.0329	0.0323	1.0186	0.4156
GP	-0.0412	0.0187	-2.2074	0.1580
SMTq	0.0436	0.0323	1.3482	0.3100
IV	-0.0471	0.0187	-2.5236	0.1276
GDq	-0.0482	0.0323	-1.4926	0.2741
GD	0.2789	0.0187	14.9496	0.0044
R^2	0.9919		Multiple R	0.9960
F	16.4		Residual σ	0.0222

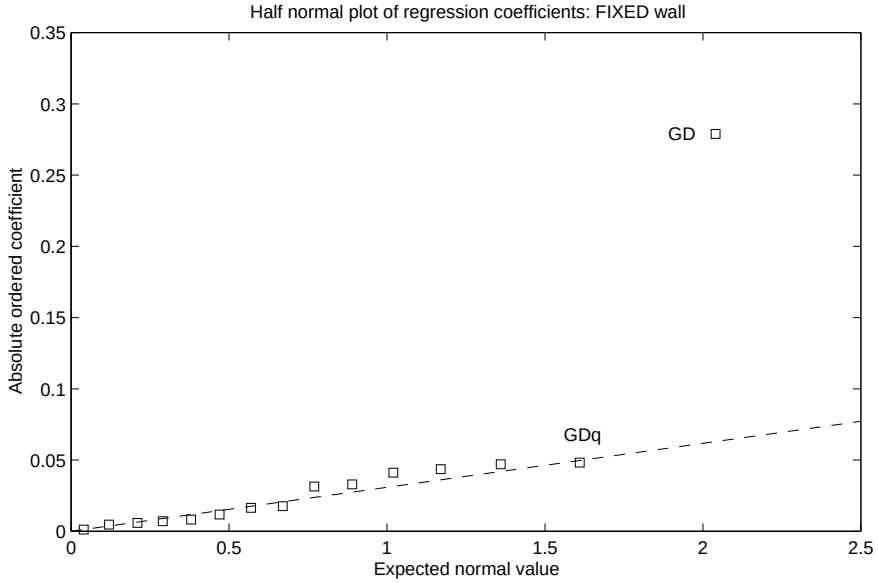

Figure 4.22: Multiple regression output and half-normal plot for FIXED wall.

Factor	Coeff	Std. err	t-stat	P-value
Intercept	1.8988	0.0166	114.2234	0.0001
IVq	-0.0047	0.0353	-0.1330	0.9063
GTq	0.0059	0.0353	0.1668	0.8828
SMT	-0.0082	0.0204	-0.4044	0.7251
GPq	0.0094	0.0353	0.2675	0.8141
STTx SMTq	-0.0129	0.0353	-0.3668	0.7490
e2	0.0165	0.0204	0.8088	0.5035
e1	-0.0188	0.0204	-0.9251	0.4526
STTx SMT	-0.0224	0.0204	-1.0986	0.3865
GT	0.0271	0.0204	1.3295	0.3151
SMTq	0.0341	0.0353	0.9680	0.4352
IV	-0.0400	0.0204	-1.9651	0.1883
STT	-0.0439	0.0166	-2.6422	0.1183
GP	-0.0494	0.0204	-2.4281	0.1359
GDq	-0.0718	0.0353	-2.0359	0.1787
GD	0.2554	0.0204	12.5443	0.0063
R^2	0.9893		Multiple R	0.9946
F	12.2720		Residual σ	0.0242

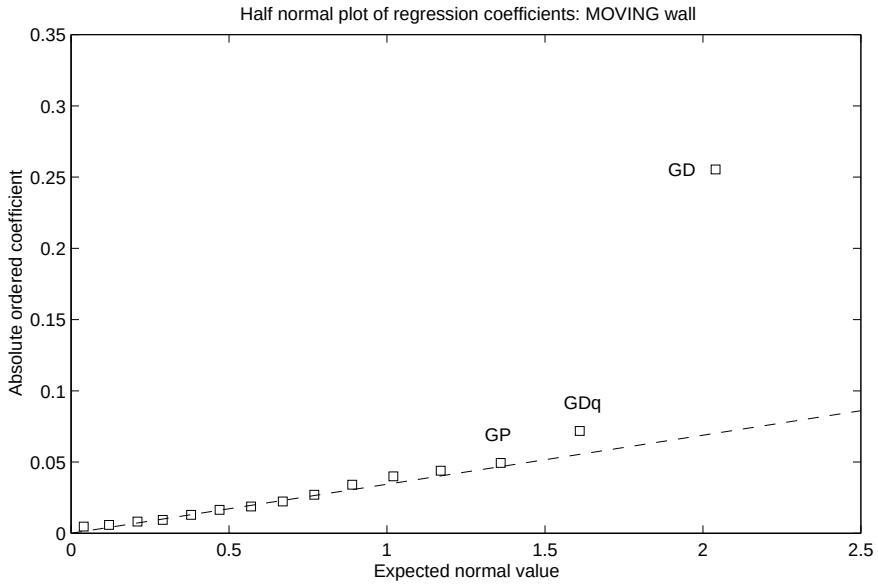

Figure 4.23: Multiple regression output and half-normal plot for MOVING wall.

Factor	Coeff	Std. err	t-stat	P-value
Intercept	2.8553	0.0151	188.9023	0.0000
SMTq	0.0053	0.0321	0.1650	0.8841
STT	-0.0157	0.0151	-1.0402	0.4075
STTx SMT	0.0171	0.0185	0.9246	0.4528
GP	0.0201	0.0185	1.0833	0.3919
e1	-0.0271	0.0185	-1.4657	0.2804
GPq	0.0319	0.0321	0.9935	0.4252
GT	0.0407	0.0185	2.1986	0.1590
e2	0.0496	0.0185	2.6771	0.1158
GTq	0.0513	0.0321	1.6005	0.2506
IVq	0.0584	0.0321	1.8211	0.2102
STTx SMTq	-0.0643	0.0321	-2.0056	0.1827
SMT	-0.0926	0.0185	-5.0031	0.0377
IV	-0.1009	0.0185	-5.4496	0.0321
GDq	-0.1062	0.0321	-3.3120	0.0803
GD	0.2372	0.0185	12.8108	0.0060
R^2	0.9923		Multiple R	0.9961
F	17.1993		Residual σ	0.0220

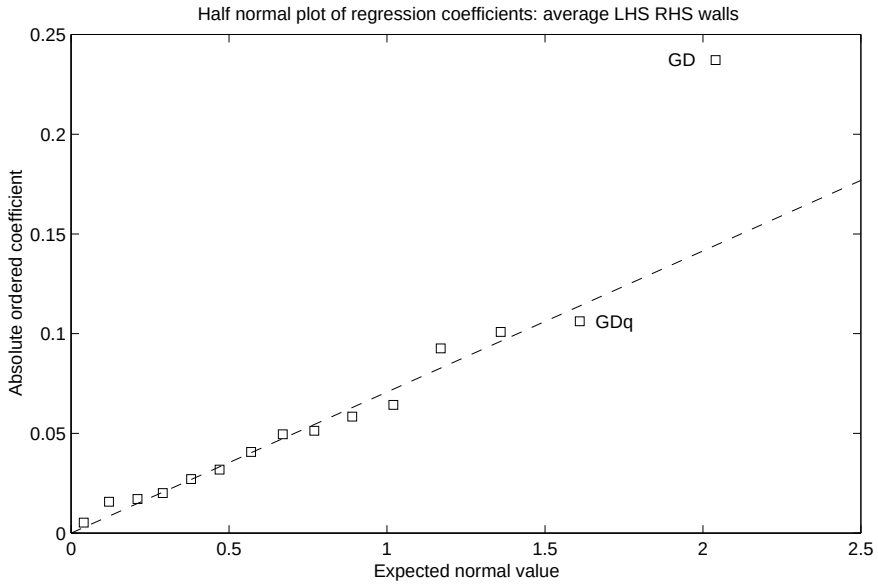

Figure 4.24: Multiple regression output and half-normal plot for average LHS and RHS walls.

Factor	Coeff	Std. err	t-stat	P-value
Intercept	1.8854	0.0158	119.4165	0.0001
IVq	0.0000	0.0335	0.0004	0.9997
GPq	0.0018	0.0335	0.0530	0.9626
SMT	-0.0035	0.0193	-0.1823	0.8722
e1	-0.0035	0.0193	-0.1829	0.8717
STTx SMTq	-0.0106	0.0335	-0.3162	0.7818
e2	0.0165	0.0193	0.8518	0.4841
GT	0.0171	0.0193	0.8826	0.4706
GTq	0.0194	0.0335	0.5792	0.6210
STTx SMT	-0.0200	0.0193	-1.0352	0.4094
STT	-0.0377	0.0158	-2.3848	0.1399
SMTq	0.0389	0.0335	1.1600	0.3658
IV	-0.0435	0.0193	-2.2520	0.1531
GP	-0.0453	0.0193	-2.3431	0.1439
GDq	-0.0600	0.0335	-1.7918	0.2150
GD	0.2672	0.0193	13.8158	0.0052
R^2	0.9908		Multiple R	0.9954
F	14.3175		Residual σ	0.0230

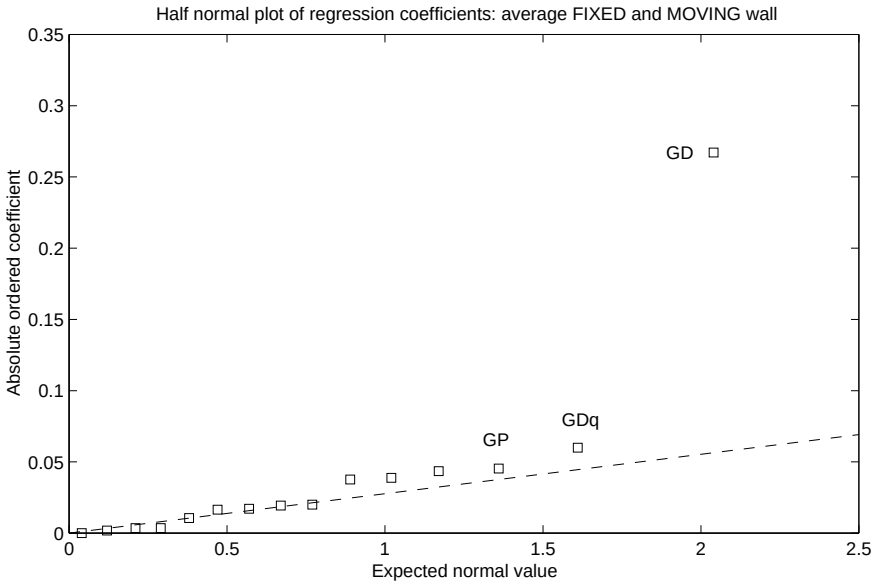

Figure 4.25: Multiple regression output and half-normal plot for average FIXED and MOVING walls.

Wall	Factors	R^2	σ
FIXED	GD GDq IV GP STT	0.971	0.042
MOVING	GD GDq GP STT IV	0.979	0.048
Av. LHS RHS	GD GDq IV SMT	0.884	0.085
Av. FIX MOV	GD GDq GP IV STT	0.970	0.041

Table 4.5: Coefficients considered for regression equation for each wall

dard error of the factor settings. The standard error for the 2^{nd} to the 8^{th} factor (IV to e2 respectively) is the same since the number of -1, 0 and +1's is the same in each column. Although tables indicate what the critical t-statistic value is, the general rule is that a t-statistic above 2.0 is worth considering as a real effect [53]. This means that approximately a 10% probability exists that the effect is caused solely by random variation, which is low enough to consider the effect to be real. The P-value indicates the probability that the effect is due to random variation and a value less than 5% is a positive indication that the effects is real.

Table 4.5 is a summary of the factors to be included in the regression model for each wall. The R^2 value for the regression model fit to the response data and the standard deviation (σ) are also shown for each respective model. The regression model for the fixed wall includes all of the factors with a t-statistic above 2.0 except for GDq. Adding GDq only improved the R^2 value by 0.01, but since the GD factor was included and was clearly the most significant linear factor GDq was also included within the model.

The factors included within the moving wall regression model are the same as for the fixed wall regression model. This is expected since both walls are on opposite sides of a line of symmetry. However, the relative magnitude of the factor coefficients and hence the order in which they appear on the half-normal

plots differ. The signs of the factor coefficients between the fixed and moving walls are the same, which indicate that the tendency is the same for the factors to increase or decrease the residual wall. A regression equation formed for the average of the fixed and moving wall responses serves as a check on the regression method and a means to produce a single wall thickness prediction along the short dimension axis of symmetry. The factors included within the regression equation are the same as for the individual fixed and moving wall regression equations. Again the signs of the regression coefficients are the same as for the individual cases.

The regression equations for the fixed and moving walls provides R^2 values of 97% which indicates a good fit to the experimental data points.

The factors included within the average LHS and RHS regression equation are different from the fixed and moving case. The LHS RHS equation does not contain gas pressure (GP) and tool temperature (STT), but adds melt temperature (SMT) as a significant factor.

Residual values are calculated in order to calibrate the model and obtain the accuracy of the regression equation fit to the experimental data points. Residuals for each of the 18 observations are calculated from the difference between predicted responses using the regression equation and the experimentally obtained responses originally used to derive the regression equation. Clearly only the experimental settings that correspond to coefficients within the regression equation are used to predict the new response matrix.

The residuals calculated for each regression model and over the 18 observations

Observation	FIXED	MOVING	Average LHS RHS	Average FIX MOV
1	-0.0302	-0.0298	0.0413	-0.0300
2	-0.0149	0.0149	-0.0808	0.0000
3	0.0404	0.0196	0.2077	0.0300
4	-0.0326	-0.0463	-0.0112	-0.0394
5	-0.0479	-0.0133	-0.0342	-0.0306
6	-0.0232	-0.0345	-0.0466	-0.0288
7	0.1099	0.1043	0.1203	0.1071
8	0.0263	-0.0345	-0.0655	-0.0041
9	-0.0278	0.0196	0.0106	-0.0041
10	0.0232	0.0557	-0.0932	0.0395
11	0.0231	0.0275	-0.0844	0.0253
12	0.0384	0.0298	0.0201	0.0341
13	-0.0322	-0.0926	-0.0430	-0.0624
14	-0.0498	0.0133	0.0791	-0.0182
15	0.0114	0.0369	0.0348	0.0241
16	-0.0286	-0.0008	0.1026	-0.0147
17	0.0443	0.0110	-0.0477	0.0276
18	-0.0298	-0.0808	-0.1097	-0.0553
σ	0.0420	0.0479	0.0854	0.0412

Table 4.6: Residuals for factors used in regression equation.

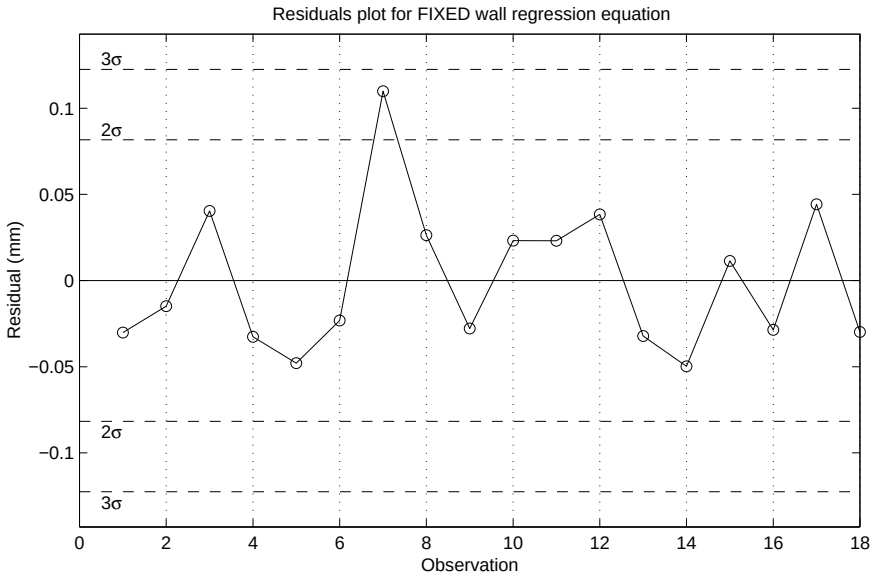

Figure 4.26: Residual plot from FIXED wall regression equation

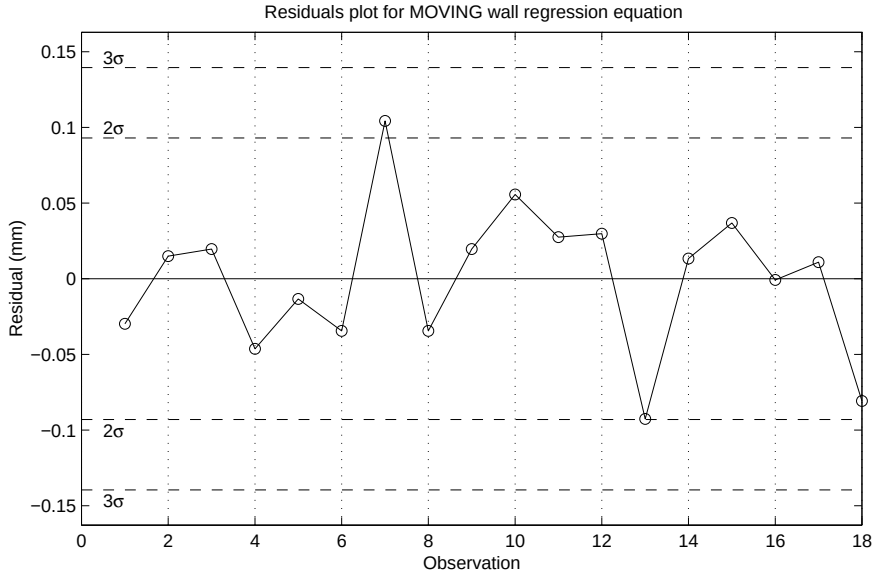

Figure 4.27: Residual plot from MOVING wall regression equation

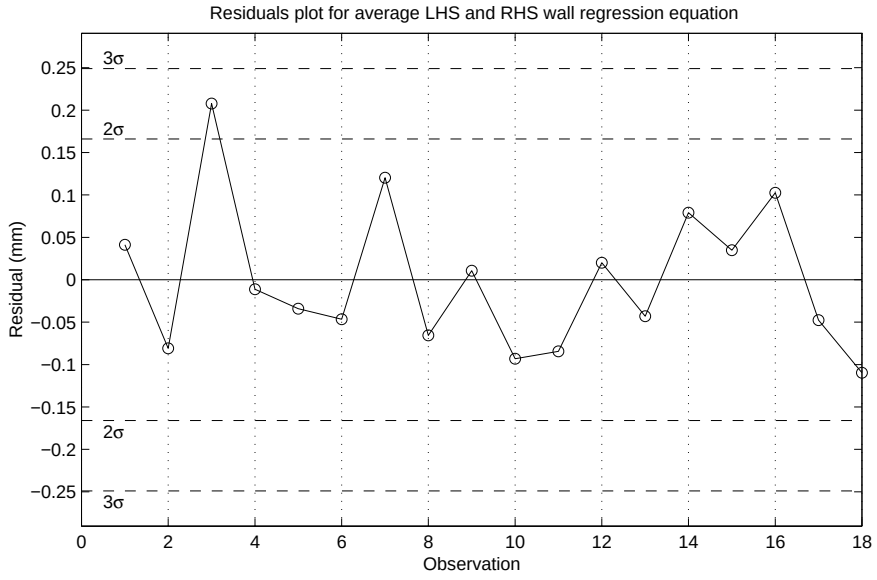

Figure 4.28: Residual plot from average of LHS and RHS wall regression equation

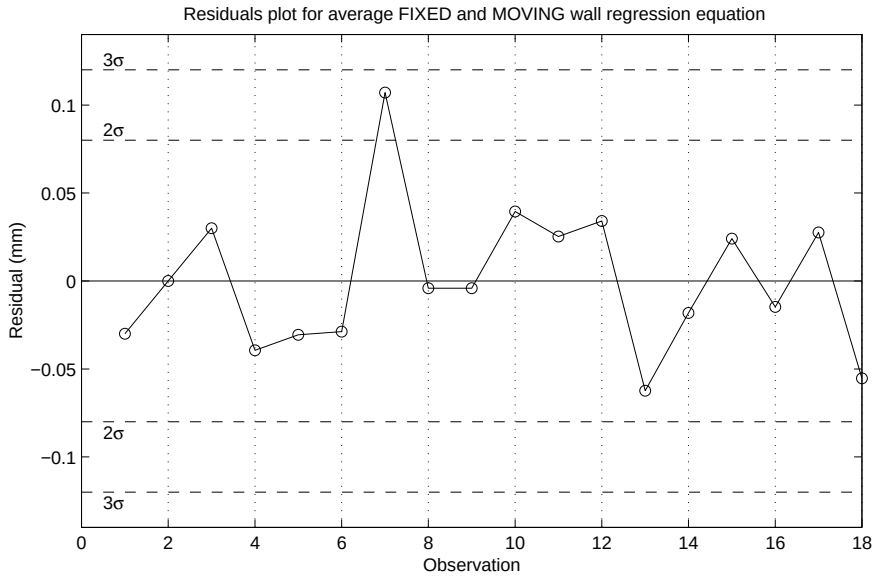

Figure 4.29: Residual plot from average of FIXED and MOVING wall regression equation

is tabulated in table 4.6. Figures 4.26 to 4.29 are plots of the residuals. The mean of the residuals is zero and the standard deviation (σ) indicates the accuracy of the model to predict the response data. The residual plots show the 2σ and 3σ limits calculated from the residual data, which assumes the residuals are normally distributed. All of the residuals are contained within 3σ and at most only 1 data point is outside the 2σ limit. The accuracy of each model can be stated as $\pm 3\sigma$ about the predicted wall thickness for each regression equation.

4.4.6 The empirical prediction equation for wall thickness

The regression equation is of the form shown in equation 4.2,

$$y_{wall} = \bar{y}_{wall} + P_1 S_1 + P_{q1} S_1^2 + ... + P_n S_n + P_{qn} S_n^2 \tag{4.2}$$

where y_{wall} is the predicted wall thickness, $\bar{y}_{wall}$ is the mean wall thickness, P is the linear parameter coefficient, P_q is the quadratic parameter coefficient and S is the setting. The setting S is in the range $-1 \leq 0 \leq +1$ and corresponds to a real set value. The regression equations for each wall, developed from the preceeding analysis, are shown in equations 4.3 to 4.6.

$$\begin{aligned} Wall_{fixed} &= 1.872 + 0.2789(GD) - 0.0482(GD^2 - 2/3) \\ &\quad -0.0471(IV) - 0.0412(GP) - 0.0314(STT) \end{aligned} \tag{4.3}$$

$$\begin{aligned} Wall_{moving} &= 1.8988 + 0.2554(GD) - 0.0718(GD^2 - 2/3) \\ &\quad -0.0494(GP) - 0.0439(STT) - 0.0400(IV) \end{aligned} \tag{4.4}$$

$$\begin{aligned} Wall_{lhs/rhs} &= 2.8553 + 0.2372(GD) - 0.1062(GD^2 - 2/3) \\ &\quad -0.1009(IV) - 0.0926(SMT) \end{aligned} \tag{4.5}$$

$$\begin{aligned} Wall_{fix/mov} &= 1.8854 + 0.2672(GD) - 0.0600(GD^2 - 2/3) \\ &\quad -0.0453(GP) - 0.0435(IV) - 0.0377(STT) \end{aligned} \tag{4.6}$$

Factor	Range	m	c
STT	30–60°C	0.0667	-3.0000
SMT	210–250°C	0.0500	-11.5000
IV	20–80%	0.0333	-1.6667
GP	30–80bar	0.0400	-2.200
GD	0–10.0sec	0.2000	-1

Table 4.7: Conversion of real factors values into the regression equation values

In order to use the regression equations using real parameter settings, such as a gas delay time of 8 seconds, the real factor value must first be converted to the range -1 to +1. The conversion equation for each factor will be simply a straight line conversion, shown in equation 4.7,

$$F = mx + c \tag{4.7}$$

where F is the factor setting entered into the regression equation within the range -1 to +1, x is the real factor setting value (e.g. 210°C) and m is the gradient of the conversion and c is the intercept. Table 4.7 contains the m and c values for each factor used in equation 4.7 and indicates the range over which the regression equation is valid.

4.5 Summary

A regression equation has been formulated in order to predict the wall thickness along the specimen gauge length as a function of processing parameter settings. Initial experiments and observations of the processing effects upon the final product have outlined the processing parameters that should be included within an

experimental study. Special attention is paid to the control of gas injection into the specimen. A gas pressure measurement chamber is used to check the behaviour of gas flow through the needle. The gas flow analysis is based upon ideal gas laws, which are too simplistic to give an accurate estimate for this application. However, the instability of the gas pressure is a useful process indicator to show that gas pressure is still building or the bubble is expanding.

The distribution of heat over a cross section before gas penetration influences the position of the gas bubble after penetration. The location of a tab gate separating the runner system and the specimen cavity causes shear heating of the melt and an uneven distribution of melt temperature over the cross section. The uneven heat distribution was indicated by differential residual wall thickness that was eradicated by removing the gate.

Chapter 5

Theory for the simulation of cavity filling

5.1 Introduction

The aim of simulation is to provide a prediction of system behaviour given the initial starting conditions and the values of any significant process variable. In this thesis the aim of the simulation is to provide 3D information regarding the residual wall thickness shape and dimensions within a representation of a real cavity. Significant filling parameters, such as quantity of melt, melt temperature and gas pressure, which are derived from experiment are utilised within the simulation. In later chapters results from the simulation are compared with real specimens.

The fundamentals of the flow equations, which are conservation of mass and momentum, are explained in the early sections. The Navier-Stokes equations provide the framework upon which the flow solution is generated. Modification

to the Newtonian scheme yields a pseudo concentration method for tracking dual fluids within the FE domain. An overview of models to represent polymer rheology is provided and the Cross-WLF model is implemented within the simulation code.

Important FE implementation issues include meshing, solution procedure and computational requirements. These issues are addressed at the end of the chapter.

The modelling code is written by Dr. Peter Olley (University of Bradford) in the first instance. The implementation of the FE pseudo-concentration method has been developed jointly between the author and Dr. Olley. In particular, the author has investigated the rheological models and obtained parameters with values for the model.

5.2 Modelling the GAIM process physics

Derivation of the conservation of mass and momentum equations is based upon an infinitesimally small fluid element fixed in space. Many of the following constitutive equations for fluid flow have been taken from Anderson [60].

5.2.1 Conservation of mass

An infinitesimally small fluid element is considered in figure 5.1. The dimensions of the fluid element are dx, dy, dz. Fluid of a variable density ρ has velocity $\mathbf{V}$, where $\mathbf{V} = u\mathbf{i} + v\mathbf{j} + w\mathbf{k}$. The unit vectors $\mathbf{i}, \mathbf{j}$ and $\mathbf{k}$ lie along the x, y and z axes respectively. The mass flux through the element is resolved along the x-axis, although similar expressions for mass flux along the y and z-axes are omitted for

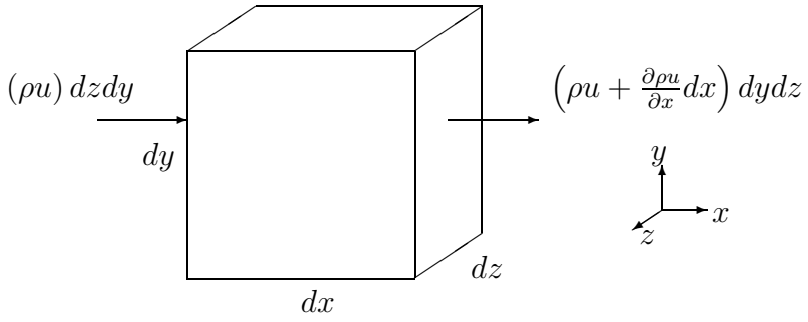

Figure 5.1: An infinitesimally small fluid element showing the mass flux through the faces normal to the x-direction. Similar mass fluxes can be derived from the faces normal to the y-direction and z-direction.

clarity.

The conservation of mass principle, when applied to a fixed region of fluid in space states:

> "...the net mass flow out of the element must equal the time rate of *decrease* inside the element." [60]

Applying this principle to the element shown in figure 5.1, along the x,y and z-axes, yields the following equation,

$$\left[\frac{\partial(\rho u)}{\partial x} + \frac{\partial(\rho v)}{\partial y} + \frac{\partial(\rho w)}{\partial z}\right] dxdydz = -\frac{\partial \rho}{\partial t} dxdydz \ ,$$

rearranging,

$$\frac{\partial \rho}{\partial t} + \left[\frac{\partial(\rho u)}{\partial x} + \frac{\partial(\rho v)}{\partial y} + \frac{\partial(\rho w)}{\partial z}\right] = 0 \ ,$$

which is usually expressed in vector notation to yield a partial differential form

of the continuity equation, shown in equation 5.1,

$$\frac{\partial \rho}{\partial t} + \nabla . (\rho \mathbf{V}) = 0 \ . \tag{5.1}$$

When the density is considered to be constant, equation 5.1 further simplifies to equation 5.2,

$$\frac{\partial u}{\partial x} + \frac{\partial v}{\partial y} + \frac{\partial w}{\partial z} = 0 \ . \tag{5.2}$$

5.2.2 Conservation of momentum

The conservation of momentum equations are derived from Newton's second law of motion (equation 5.3).

$$\mathbf{F} = m\mathbf{a} \tag{5.3}$$

The infinitesimally small fluid element moving with the fluid flow, shown in figure 5.2, experiences a number of surface forces. These are shear viscous, normal viscous and pressure. Body forces, which are not shown in figure 5.2, include acceleration due to gravity and electromagnetic effects.

Viscous surface forces notation is in the τ_{ij} form, where i and j refer to vectors normal to the surface and in the direction of the force respectively. The body force vector per unit volume experienced by the element is $\mathbf{f}$ and the element is of density ρ. Resolving the surface and body forces yields the system of equations 5.4. Taking moments about any point in figure 5.2 proves that $\tau_{xy} = \tau_{yx}$,

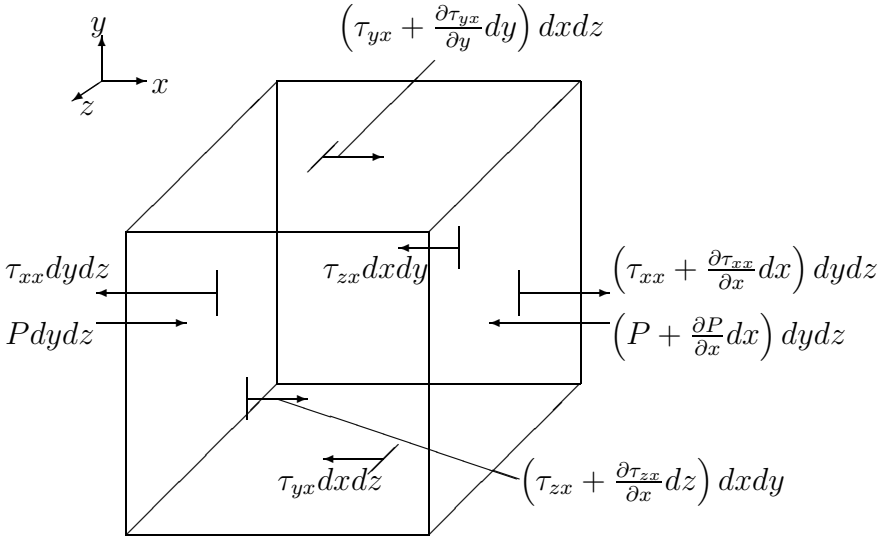

Figure 5.2: The surface forces on an infinitesimally small fluid element, of dimension dx, dy, dz, moving with the fluid flow. The velocities u, v and w are in the directions x, y and z respectively. Pressure, normal viscous and shear viscous forces are shown resolved in the x-direction. (Figure taken from Anderson, [60])

$\tau_{xz} = \tau_{zx}$ and $\tau_{yz} = \tau_{zy}$.

$$\begin{aligned}
\rho \frac{du}{dt} &= -\frac{\partial P}{\partial x} + \frac{\partial \tau_{xx}}{\partial x} + \frac{\partial \tau_{yx}}{\partial y} + \frac{\partial \tau_{zx}}{\partial z} + \rho f_x \\
\rho \frac{dv}{dt} &= -\frac{\partial P}{\partial y} + \frac{\partial \tau_{xy}}{\partial x} + \frac{\partial \tau_{yy}}{\partial y} + \frac{\partial \tau_{zy}}{\partial z} + \rho f_y \\
\rho \frac{dw}{dt} &= -\frac{\partial P}{\partial z} + \frac{\partial \tau_{xz}}{\partial x} + \frac{\partial \tau_{yz}}{\partial y} + \frac{\partial \tau_{zz}}{\partial z} + \rho f_z
\end{aligned} \tag{5.4}$$

The *Stokes' law of friction* relates stress to strain in a *Newtonian* gas or liquid system and the system of equations 5.5 shows this hypothesis [61].

$$\begin{aligned}
\tau_{xx} = \eta \left(2\frac{\partial u}{\partial x} - \frac{2}{3}\nabla.\mathbf{V}\right) \quad ; \quad \tau_{xy} = \eta \left(\frac{\partial u}{\partial y} + \frac{\partial v}{\partial x}\right) \\
\tau_{yy} = \eta \left(2\frac{\partial v}{\partial y} - \frac{2}{3}\nabla.\mathbf{V}\right) \quad ; \quad \tau_{yz} = \eta \left(\frac{\partial v}{\partial z} + \frac{\partial w}{\partial y}\right)
\end{aligned} \tag{5.5}$$

$$\tau_{zz} = \eta\left(2\frac{\partial w}{\partial z} - \frac{2}{3}\nabla.\mathbf{V}\right) \quad ; \quad \tau_{xz} = \eta\left(\frac{\partial w}{\partial x} + \frac{\partial u}{\partial z}\right)$$

Substituting the system of equations 5.5 into the system of equations 5.4 we obtain the *Navier-Stokes* equations. However, for an incompressible fluid, where $\nabla.\mathbf{V} = 0$ and where body forces are neglected ($\mathbf{f} = 0$), a simplified version of the Navier-Stokes equation is obtained and shown in the system of equations 5.6.

$$\begin{aligned}
\rho\frac{\partial u}{\partial t} &= -\frac{\partial P}{\partial x} + \frac{\partial}{\partial x}\left(2\eta\frac{\partial u}{\partial x}\right) + \frac{\partial}{\partial y}\left(\eta\left(\frac{\partial u}{\partial y} + \frac{\partial v}{\partial x}\right)\right) + \frac{\partial}{\partial z}\left(\eta\left(\frac{\partial u}{\partial z} + \frac{\partial w}{\partial x}\right)\right) \\
\rho\frac{\partial v}{\partial t} &= -\frac{\partial P}{\partial y} + \frac{\partial}{\partial x}\left(\eta\left(\frac{\partial u}{\partial y} + \frac{\partial v}{\partial x}\right)\right) + \frac{\partial}{\partial y}\left(2\eta\frac{\partial v}{\partial y}\right) + \frac{\partial}{\partial z}\left(\eta\left(\frac{\partial w}{\partial y} + \frac{\partial v}{\partial z}\right)\right) \\
\rho\frac{\partial w}{\partial t} &= -\frac{\partial P}{\partial z} + \frac{\partial}{\partial x}\left(\eta\left(\frac{\partial u}{\partial z} + \frac{\partial w}{\partial x}\right)\right) + \frac{\partial}{\partial y}\left(\eta\left(\frac{\partial w}{\partial y} + \frac{\partial v}{\partial z}\right)\right) + \frac{\partial}{\partial z}\left(2\eta\frac{\partial w}{\partial z}\right)
\end{aligned} \tag{5.6}$$

5.2.3 Pseudo concentration method

The basis of the pseudo-concentration method is to assign a label to material that is present within the FE domain. Tracking of two different fluids within the same domain is therefore possible using the concentration parameter, c, which is defined,

$$\left.\begin{aligned} c_{polymer} &= 1.0 \\ c_{gas} &= 0.0 \end{aligned}\right\} 0 \leq c \leq 1 \tag{5.7}$$

The boundary between polymer and gas is distinct in the real process. Since a gradient of concentration can exist within the definition given in equation 5.7, the boundary is taken to be $c = 0.5$. The transport equation for concentration

is,

$$\frac{\partial c}{\partial t} + u\frac{\partial c}{\partial x} + v\frac{\partial c}{\partial y} + w\frac{\partial c}{\partial z} = \frac{dc}{dt} = 0 \tag{5.8}$$

Local viscosity (η) and density (ρ) are interpolated according to equations 5.9 and 5.10 respectively.

$$\eta(x,y,z) = c(x,y,z)\eta_{polymer} + (1 - c(x,y,z))\eta_{gas} \tag{5.9}$$

$$\rho(x,y,z) = c(x,y,z)\rho_{polymer} + (1 - c(x,y,z))\rho_{gas} \tag{5.10}$$

These density and viscosity are then used in the next time step. The fact that density is interpolated does not conflict with the incompressible fluid assumption made in equation 5.2. Here the density change is local only to the interface between gas and polymer.

5.3 Melt viscosity models for the Pseudo concentration method

A number of models exist to describe the relationship between shear rate and shear stress for polymer melts. The models available range from simple to complex and are outlined in the following sections. In the first instance some background on the general behaviour of fluids is presented. Figure 5.3 shows schematically a number of different shear stress against shear rate relationships for different categories of fluids.

The simplest type of real fluid is *Newtonian*, where the shear stress is linearly

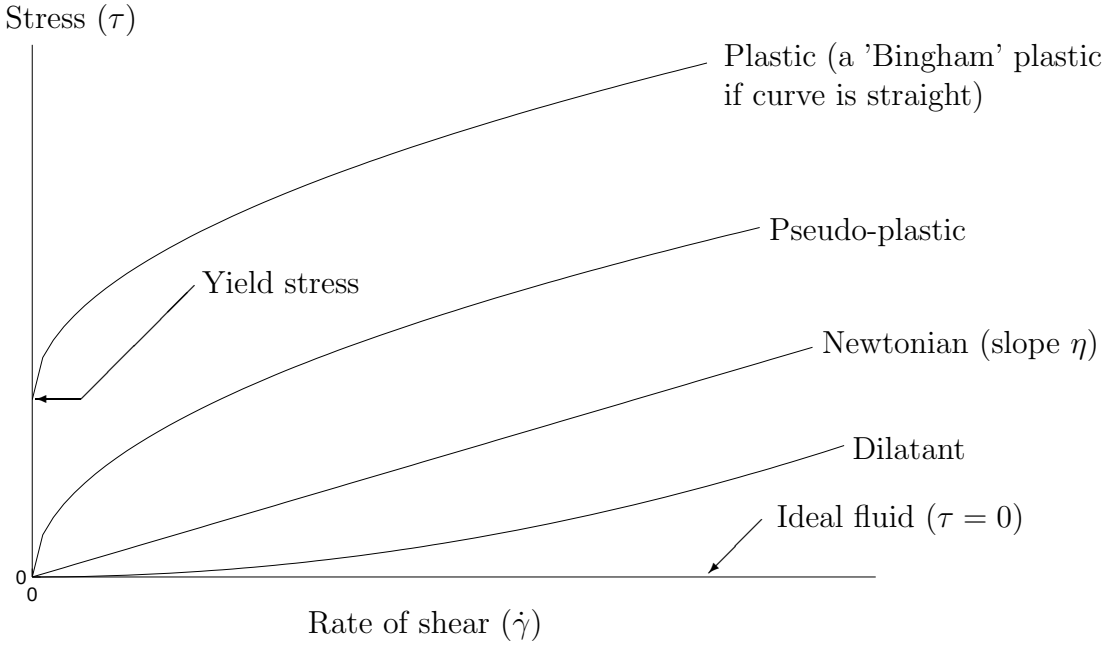

Figure 5.3: A schematic plot showing a number of different fluid types and the relationship between shear stress (τ) and shear rate ($\dot{\gamma}$). (Figure taken from Massey, [10])

dependent upon the rate of shear, therefore viscosity is constant and not dependent upon the rate of shear. Gases and some small molecule liquids like water approximate to the Newtonian model [62].

Dilatant fluids exhibit an increase in viscosity with increasing rate of shear. Examples are concentrated solutions of sugar in water and aqueous suspensions of rice starch (in certain concentrations) [10]. Shear thickening sometimes indicates complications with some fluids such as instability, phase separation and lack of reversibility [62]. Dilatant fluids will not be considered any further.

Polymer melts fall into the *pseudo-plastic* category of fluids, where the shear viscosity decreases with an increasing rate of shear. Other fluids in this category are gelatine, blood, clay and milk.

Some fluids exhibit viscosity time dependency, where the viscosity may change over time at constant rate of shear. Increasing viscosity is termed *rheopectic* and decreasing viscosity is termed *thixotropic*.

5.3.1 Newtonian

The Newtonian fluid is the simplest model of a fluid that can physically exist. Here the viscosity of the fluid remains constant (i.e. independent of rate of shear) and the relationship between shear stress and rate of shear is shown in equation 5.11 [10].

$$\tau = \eta \frac{\partial u}{\partial y} \tag{5.11}$$

The more general 3D form of the relationship (for an incompressible fluid) is shown in equation 5.12,

$$\tau_{ij} = \eta \left(\frac{\partial u_i}{\partial x_j} + \frac{\partial u_j}{\partial x_i} \right) \ . \tag{5.12}$$

Stokes' law of friction in equation 5.5 shows the full expansion of equation 5.12.

5.3.2 Power law

The power law model offers a good approximation for fluids that exhibit shear thinning to the relationship between viscosity and rate of shear. A pseudo-plastic behaviour is shown in figure 5.4, where the power law model describes the linear portion of the relationship. The power law is of the form shown in equation 5.13 [62].

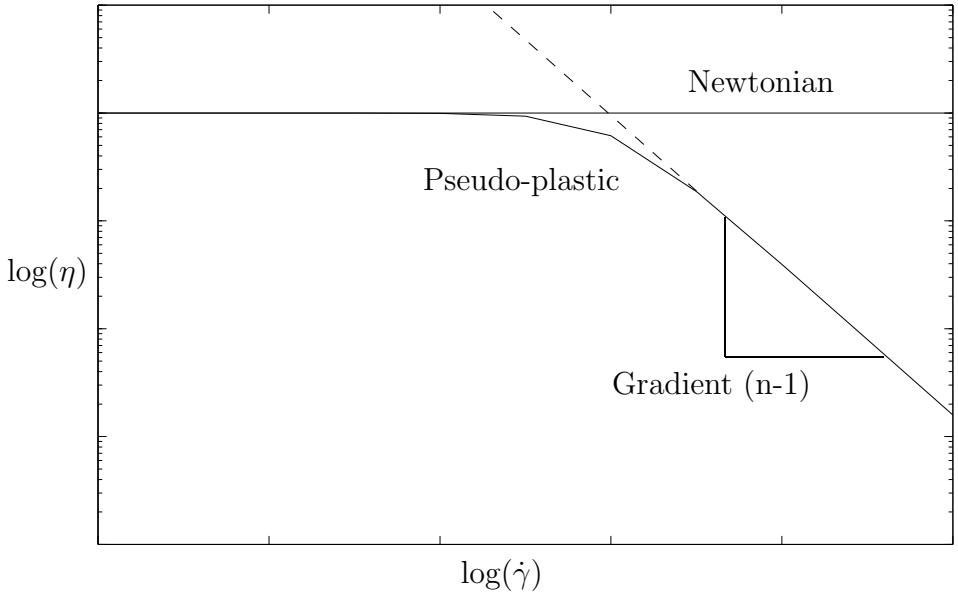

Figure 5.4: Viscosity (η) against rate of shear ($\dot{\gamma}$) for a Newtonian and pseudo-plastic fluid. The power law model is a linear fit to the pseudo-plastic region. At low shear rates the approximation is less accurate, tending to ∞, which is shown by the dotted line.

$$\eta = m\dot{\gamma}^{n-1} \tag{5.13}$$

The gradient of the power law model is (n-1) and is a good approximation to the viscosity above a certain shear stress that is material dependent. The viscosity of pseudo-plastic fluids at low shear rates is more like a Newtonian relationship. The power law approximation fails to predict this behaviour and tends to ∞.

5.3.3 Cross model for shear rate viscosity dependence

In order to fit a model to the low shear rate Newtonian region and higher shear rate power law region Cross proposed the following model (equation 5.14).

$$\eta = \eta_\infty + \left(\frac{\eta_0 - \eta_\infty}{1 + (\lambda\dot{\gamma})^m} \right) \tag{5.14}$$

where, η_0 and η_∞ are viscosity at low and high shear rates respectively. At intermediate rates of shear ($\eta_0 \gg \eta \gg \eta_\infty$) equation 5.14 gives an approximation to power law behaviour with $m = 1 - n$. In this region $log\eta/log\dot{\gamma} = -m$. At sufficiently low shear rates λ can be determined from $\lambda = \eta_0/G_0$ where G_0 is the Hookean shear modulus [63, 64].

A popular form of the Cross model is the modified Cross model that takes the form shown in equation 5.15.

$$\eta = \frac{\eta_0}{1 + \left(\frac{\eta_0\dot{\gamma}}{\tau^*}\right)^{1-n}} \tag{5.15}$$

where, τ^* characterises the shear-stress level related to the transition between the Newtonian and power-law regimes [65, 62, 66].

To illustrate the Cross model, a plot is shown in figure 5.5, where arbitrary parameter values have been used to calculate the shear rate and viscosity relationship. The zero shear rate (η_0) values are also chosen arbitrarily to represent four different melt temperatures.

5.3.4 Williams-Landel-Ferry (WLF) temperature dependence

The effect of temperature upon viscosity for most polymer melts is significant. The viscosity tends to decrease with increasing temperature. Ferry [67] intro-

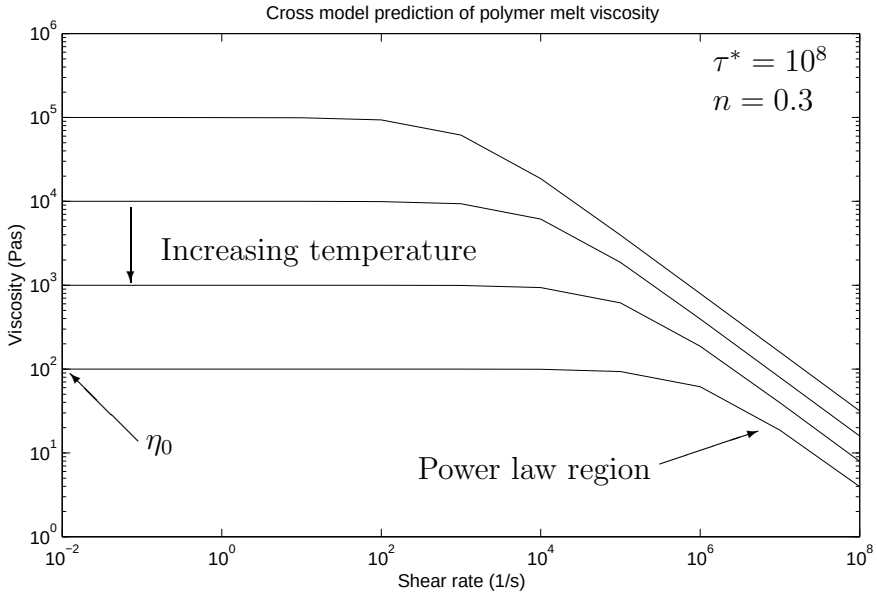

Figure 5.5: The Cross model applied to an arbitrary fluid with the parameters $\tau^* = 10^8$ and $n = 0.3$. The temperature dependence of zero shear rate (η_0) is assumed at four temperatures.

duced a shift factor based upon shear rate temperature superposition to account for a change in shear rate at constant shear stress from a reference temperature. The relationship is shown in equation 5.16,

$$a_T = \frac{\dot{\gamma}(ref)}{\dot{\gamma}(T)} \qquad \text{(const. } \tau\text{)} \tag{5.16}$$

where, a_T is the shift factor (or relaxation times at two different temperatures), $\dot{\gamma}(ref)$ is the shear stress at the reference temperature and $\dot{\gamma}(T)$ is the shear rate at temperature T. The shear rate ratio is calculated at constant shear stress [68]. Equation 5.16 can also be written [68],

$$a_T = \frac{\eta(T)}{\eta(ref)} \qquad \text{(const. } \tau\text{)} \tag{5.17}$$

The Williams-Landel-Ferry (WLF) equation is,

$$log\ a_T = \frac{-c_1(T - T_g)}{c_2 + T - T_g} \tag{5.18}$$

where, c_1 and c_2 are empirical constants and T_g is the glass transition temperature [67]. However, T_g can be replaced by any reference temperature (T_s) and the empirical constants c_1 and c_2 recalculated.

5.3.5 Cross-WLF model

The model for melt viscosity used in this theses employs both the cross model and WLF temperature dependence. The cross model (equation 5.15) is repeated here.

$$\eta = \frac{\eta_0(T)}{1 + \left(\frac{\eta_0(T)\dot{\gamma}}{\tau^*}\right)^{1-n}}$$

The zero shear rate viscosity at a given temperature ($\eta_0(T)$) is take from the WLF model of the form shown in equation 5.19 [65, 66].

$$\eta_0(T) = \eta^* exp\left(\frac{-c_1(T - T_s)}{c_2 + T - T_s}\right) \tag{5.19}$$

where η^* is the zero shear rate viscosity at the reference temperature T_s

5.4 Outline of the finite element implementation

The equations outlined in section 5.2 have, in the first instance, been implemented in 2D. Many initial parameter investigations are carried out in 2D before a more computationally intensive, but realistic, 3D study.

The following sections outline in detail the steps taken to implement the theory into a finite element scheme suitable for solution by computer. Ultimately the finite element implementation is written into a FORTRAN code. The three main steps involved in implementation are mesh generation, numerical solution and post-processing. The mesh generation stage involves defining the model geometry with discrete elements. Boundary conditions associated with zero wall slip and symmetry are defined here.

The solution stage takes the defined geometry and boundary conditions along with any other filling information and begins the process of solving the Navier-Stokes equations. The results of the solution are written to a file that can be read by a post-processing application to display, graphically, the geometry and nodal values.

5.4.1 Linear finite elements

The domain is represented by rectangular linear finite elements [69, p.411]. Linear elements are selected to avoid the condition where interpolation between known values, such as viscosity, may become negative in value and lead to instabilities

within the solution. Figure 5.6 illustrates how a quadratic interpolation of three points, which all have values greater than zero, can be negative between the known values. A linear interpolation of two points greater than zero will never become negative.

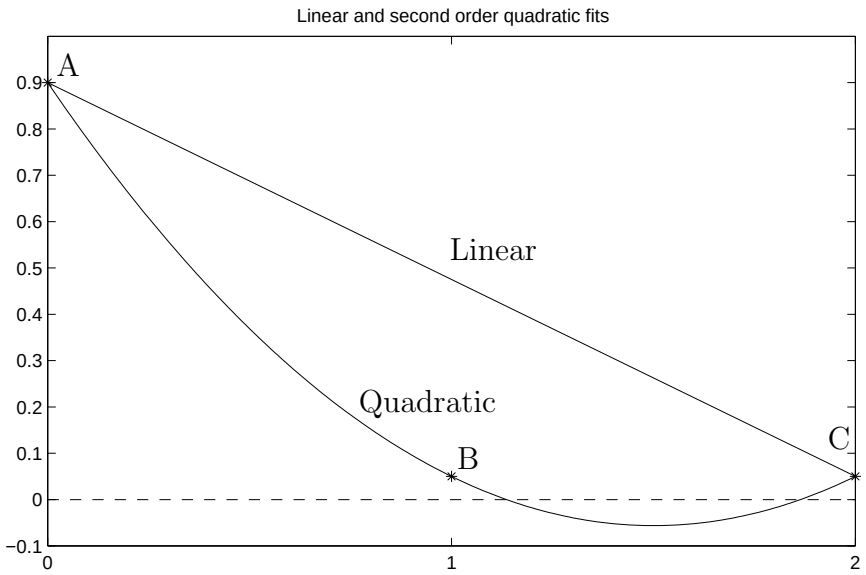

Figure 5.6: Consider three points A, B and C that all have values greater than zero. A quadratic interpolation of the points can lead to some points on the approximation becoming negative. However, a linear interpolation of the first and last point (A and C) will ensure that all points of the approximation are greater than zero.

The geometry of the tensile test specimen is generally rectangular. This is convenient for the rectangular finite elements to describe the geometry with sufficient accuracy.

5.4.2 Finite element equations

The general form of the finite element equation considers the variation of a variable over an element as a function of position within the element and nodal values. The variation form is expressed in equation 5.22,

$$X = \sum_{i=1}^{n} \psi_i x_i \tag{5.20}$$

where n is the number of nodes in the element, ψ_i is the shape function which is a function of shape within the element and x_i are the nodal values of the variable x [70]. The derivative of X according to equation 5.20 is,

$$\frac{dX}{da} = \sum_{i=1}^{n} \frac{d\psi}{da} x_i \tag{5.21}$$

There are different continuity requirements on the interpolation of the velocity field and pressure. So the finite element equations for velocity (u, v, w) and pressure (P) are,

$$u = \sum_{i=1}^{n} \psi_i x_i \quad v = \sum_{i=1}^{n} \psi_i y_i \quad w = \sum_{i=1}^{n} \psi_i z_i \quad P = \sum_{i=1}^{n} \phi_i P_i \tag{5.22}$$

An example is shown below of the finite element equations 5.22 applied to the x-component of the Navier-Stokes equations. The momentum equation (5.6) is repeated,

$$\rho \frac{\partial u}{\partial t} = -\frac{\partial P}{\partial x} + \frac{\partial}{\partial x}\left(2\eta \frac{\partial u}{\partial x}\right) + \frac{\partial}{\partial y}\left(\eta\left(\frac{\partial u}{\partial y} + \frac{\partial v}{\partial x}\right)\right) + \frac{\partial}{\partial z}\left(\eta\left(\frac{\partial u}{\partial z} + \frac{\partial w}{\partial x}\right)\right)$$

If we consider steady state (i.e. $\rho\frac{\partial u}{\partial t} = 0$) and apply the finite element equations 5.22 and 5.21 the momentum equation becomes,

$$\begin{aligned} 0 &= -\frac{\partial \phi_i}{\partial x}P_i + \frac{\partial}{\partial x}\left(2\eta\frac{\partial \psi_i}{\partial x}u_i\right) + \frac{\partial}{\partial y}\left(\eta\left(\frac{\partial \psi_i}{\partial y}u_i + \frac{\partial \psi_i}{\partial x}v_i\right)\right) \\ &\quad + \frac{\partial}{\partial z}\left(\eta\left(\frac{\partial \psi}{\partial z}u_i + \frac{\partial \psi}{\partial x}w_i\right)\right) \end{aligned} \tag{5.23}$$

Multiplying through by ψ_i and integrating over the element, Ω,

$$\begin{aligned} 0 &= \int_\Omega -\psi_i\frac{\partial \phi_i}{\partial x}P_i \; d\Omega + \int_\Omega \psi_i\frac{\partial}{\partial x}\left(2\eta\frac{\partial \psi_i}{\partial x}u_i\right) \; d\Omega \\ &\quad + \int_\Omega \psi_i\frac{\partial}{\partial y}\left(\eta\left(\frac{\partial \psi_i}{\partial y}u_i + \frac{\partial \psi_i}{\partial x}v_i\right)\right) \; d\Omega \\ &\quad + \int_\Omega \psi_i\frac{\partial}{\partial z}\left(\eta\left(\frac{\partial \psi}{\partial z}u_i + \frac{\partial \psi}{\partial x}w_i\right)\right) \; d\Omega \end{aligned} \tag{5.24}$$

Substituting an integration by parts to avoid any second derivatives yields,

$$\begin{aligned} 0 &= \int_\Omega \frac{\psi_i}{\partial x}\phi_i P_i \; d\Omega - \int_\Omega \frac{\partial \psi_i}{\partial x}\left(2\eta\frac{\partial \psi_i}{\partial x}u_i\right) \; d\Omega \\ &\quad - \int_\Omega \frac{\partial \psi_i}{\partial y}\eta\left(\frac{\partial \psi_i}{\partial y}u_i + \frac{\partial \psi_i}{\partial x}v_i\right) \; d\Omega \\ &\quad - \int_\Omega \frac{\partial \psi_i}{\partial z}\eta\left(\frac{\partial \psi}{\partial z}u_i + \frac{\partial \psi}{\partial x}w_i\right) \; d\Omega \end{aligned} \tag{5.25}$$

5.4.3 Time stepping and upwinding procedures

This model is based upon a time stepping or time marching procedure explained by Reddy [69, p.224]. The time stepping procedure attempts to find the value of u_j at time t_{s+1} using the values of u_j from previous times. The α form of the

time stepping approximation is described by equation 5.26.

$$(1-\alpha)\{\dot{u}\}_s + \alpha\{\dot{u}\}_{s+1} = \frac{\{u\}_{s+1} - \{u\}_s}{\Delta t_{s+1}} \qquad \text{where } 0 \leq \alpha \leq 1 \tag{5.26}$$

The α family of well known time approximation schemes is shown below.

$$\alpha = \left| \begin{array}{ll} 0 & \text{forward difference (or Euler) scheme, (conditionally stable); accuracy} = 0(\Delta t) \\ \frac{1}{2} & \text{Crank-Nicholson (stable); } 0((\Delta t))^2 \\ \frac{2}{3} & \text{Galerkin method (stable); } = 0((\Delta t))^2 \\ 1 & \text{the backward differencing scheme (stable); } = 0(\Delta t) \end{array} \right.$$

Solution stability is aided by limiting the gradient of the change in concentration over an element. An upwinding scheme is used that introduces a diffusive tensor ($\mathbf{K}$) into equation 5.8. The diffusive tensor $\mathbf{K}$ is shown in equation 5.27. The upwinding scheme can be switched on and off within this implementation.

$$K_{ij} = \frac{dt.u_i.u_j}{2} \tag{5.27}$$

5.4.4 Numerical solution considerations

In order to solve the Navier-Stokes equations and take into consideration the incompressibility constraint, a penalty method is employed. The penalty method, in essence, allows us to reformulate a problem with constraints as one without

constraints [69, p.488]. The penalty method formula is shown in equation 5.28,

$$F_p(x, y, z) = f(x, y, z) + \frac{1}{2}\gamma[G(x, y, z)]^2 \tag{5.28}$$

where γ is the penalty parameter and $f(x, y, z)$ is the function to be solved subject to the constraint $G(x, y, z)$. The problem now is to find the minimum of the function F_p with respect to its' arguments, that is:

$$\frac{\partial F_p}{\partial x} = \frac{\partial F_p}{\partial y} = \frac{\partial F_p}{\partial z} = 0 \tag{5.29}$$

In terms of least squares, the larger the value of γ, the more accurately the constraint, $G(x, y, z)$, is satisfied.

5.5 Simulation methodology

The theory surrounding the modelling of flow is described in previous sections and here some important practical considerations are outlines. Specific use of mesh generation software and detailed step-by-step instructions on performing the simulation is not attempted. An overview is offered that draws from the guidelines for FE modelling described in the literature.

5.5.1 Domain meshing

The geometry of any domain is described using a FE mesh made exclusively from linear quadrilateral elements that have been discussed previously in section 5.4.1.

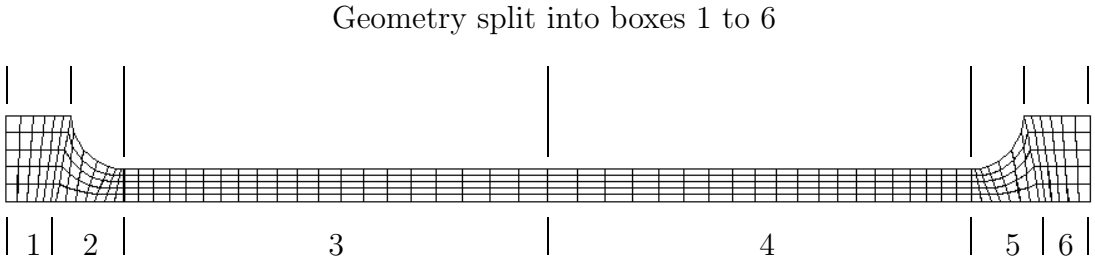

Figure 5.7: Simple boxes are used to define the geometry of a tensile test specimen. In this case 6 boxes are used that are various in shape and contain different numbers of elements. Mating boxes must have corresponding corner coordinates. The number and distribution of elements along mating boundary must also match.

The criterion to be satisfied for a successful FE mesh is as follows:- [71]

1. Essential geometrical features must be represented.

2. Element size, h, must be sufficiently small to keep approximation good.

3. Aspect ratio must be close to 1 to avoid degradation of numerical solution.

The mesh is generated from a pre-processing program written in FORTRAN specifically for this application.

The geometry of a cavity is split into simple boxes that connect together to make up the full geometry. A typical mesh describing a tensile test specimen geometry is shown in figure 5.7. Here, six boxes are used to describe the full geometry. The corners of each box are specified and the mating boundaries have identical coordinates in order to connect. Similarly, the number and distribution of elements along the mating boundary must be identical. Note, the number of elements in the vertical direction is constant throughout the geometry.

The top edges of boxes 2 and 5 are an approximation to an arc. The approximation could be more accurate if the number of nodes along that edge were increased. This would also increase the memory requirements from the computer.

In areas of the geometry where the gradients of variables are expected to be at their highest the mesh density has been increased [69]. *Bias* is useful for achieving this by increasing the nodal density (therefore number of elements) at one side of a box. This can be seen in box 3 where the left hand end of the box has a higher horizontal mesh density than the right hand end. The left hand side of the box represents a region where the flow is changing rapidly through a contraction.

5.5.2 Boundary conditions

The use of boundary conditions here has been to initiate the flow of material within the cavity, define solid boundaries that represent cavity walls and to indicate any lines of symmetry. The strategy for setting boundary conditions is to directly specify primitive variables such as u,v,w and c. This strategy is called the *Dirichlet* boundary condition [60, 69].

5.5.3 Time stepping interval

Solution stability and accuracy are affected by the time step (Δt) in this time marching procedure. A simple approach to deciding the time step interval has been employed where material cannot cross an individual element within a single time step [65]. The expected flow velocity can be estimated from the boundary conditions or a test run using a small time step.

The basis of the time step rule is to ensure that the accumulation of rounding errors from successive time step is not allowed to increase. The error from time step $n+1$ must be less than or equal to the error from time step n as in equation 5.30.

$$\left| \frac{\epsilon_i^{n+1}}{\epsilon_i^n} \right| \leq 1 \tag{5.30}$$

5.6 Summary

The theory for modelling the fluid flow within the FE domain is based on the Navier-Stokes equations. The pseudo-concentration method introduces a material label that differentiates between the gas and polymer melt within the domain. The material label is convected to produce a gas and polymer interface profile that indicates residual wall thickness.

Polymer melt rheology is described by the Cross-WLF model that gives melt viscosity as a function of temperature and shear rate. The pseudo-plastic behaviour of the melt is covered in this model. Parameters for the model are obtained from experimental rheological tests carried out off-line.

An FE implementation of the method involves meshing the domain with linear quadrilateral elements to produce a fixed grid that does not re-mesh. A time marching approach is adopted using a fixed time step. Boundary conditions to represent cavity walls and initial flow can be specified directly to relevant nodes.

This simulation technique has utilised a fixed grid that does not need to deform since the cavity dimensions remain constant throughout. Within fluids modelling the accuracy of a solution can be improved by refining the mesh dynamically,

so increasing and decreasing mesh density in regions of high and low gradient respectively. This method of adaptive meshing has been implemented successfully by Coupez et. al. [42], where the mesh at the melt flow front and gas bubble/melt interface is refined. Adaptive meshing has not been introduced here because the complexities are formidable, but this procedure is worthy of consideration for future work.

Representation of the cavity walls is achieved by setting a no-slip boundary condition ($u = v = w = 0$) at nodes falling on a wall. The implementation does not have a facility for boundary nodes to allow air past (venting), but not polymer melt (i.e. discrimination). Since air already within the cavity is represented the same way as gas which forms the bubble the convention of concentration would have to take place at the boundary nodes and the boundary would then become ineffective. Currently, the boundary at the far end of the cavity from the flow source represents an open outlet where concentration and velocity are unconstrained. Of course, a totally enclosed boundary system would lock the flow altogether.

Chapter 6

Simulation results and comparison with experiment

6.1 Introduction

The method for simulating cavity filling, outlined in chapter 5, is implemented in the form of a finite element model. This chapter details the form of the FE mesh that is used to model the tensile test specimen cavity. The specimens manufactured under an experimental framework to provide an empirical model (chapter 4) are compared with the simulation results on the basis of wall thickness. Early results for this work can be found in Johnson, Olley and Coates [72].

The accuracy of the wall thickness prediction is heavily dependent upon the correct implementation of the FE model. Issues such as mesh density and time step are shown to be influential in providing a stable and efficient result. Computational resource, particularly for a 3D solution, restricts the mesh density and

time step.

6.2 FE mesh and boundary conditions

The FE model aims to imitate the real process. Correct boundary conditions and simulation control are essential to achieve this. The symmetry of the flow and geometry are used to significantly reduce the computational requirements of the model.

6.2.1 Flow symmetry and wall boundaries

The tensile test specimen is rectangular in cross section. A small draft angle of 1^{o} exists on the side walls of the real specimen to assist with ejection from the mould. This draft angle is not likely to significantly alter the symmetrical flow assumption.

The symmetry of the model is not only governed by geometrical symmetry of the specimen; the expected flow paths and boundary conditions must also be symmetrical for symmetry to be valid. For instance, the mould wall temperature is assumed to be constant throughout the model. Any difference in wall temperature would immediately double the number of elements within the model. An outline of the model is shown in figure 6.1, which is the geometry of the specimen up to halfway along the gauge length. The cross section has two planes of symmetry along the centre lines in the xy and xz planes. The flow of melt and gas is in the positive x direction noted by the coordinate system, shown in figure 6.1.

Flow symmetry is implemented within the model using the fact that flow will

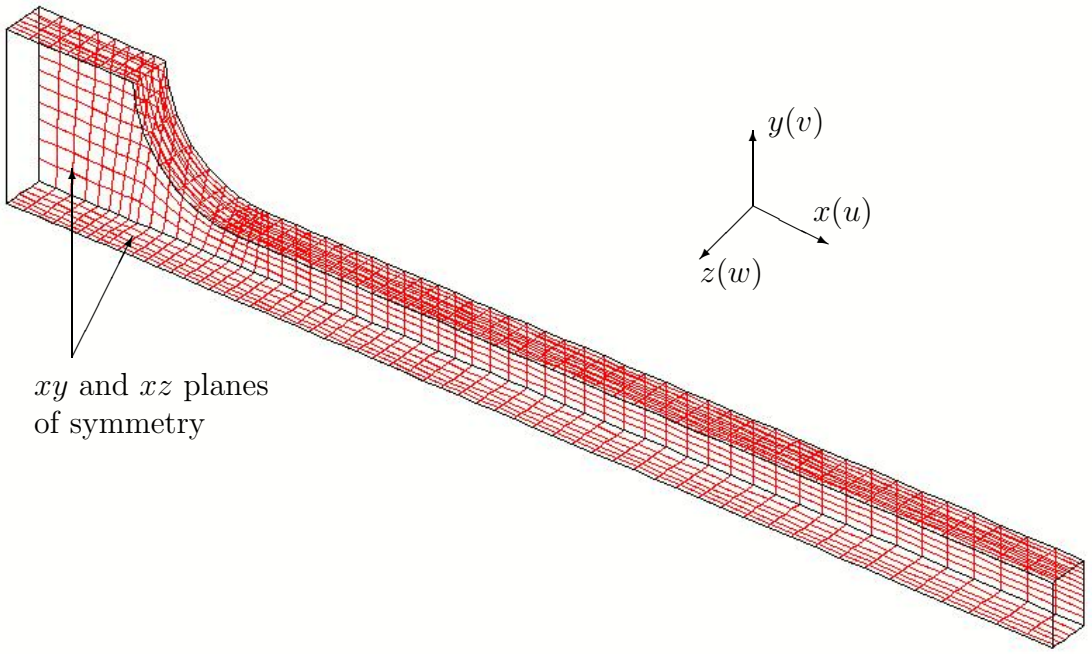

Figure 6.1: The planes of symmetry are along the xy and xz axes.

not cross the line of symmetry. Therefore, the boundary conditions are configured to prevent "normal flow", that is flow across the boundary. For example, to indicate flow symmetry along the xz-plane, flow is prevented in the y-direction by setting a $v = 0$ boundary condition over all the relevant nodes. A similar boundary condition is set of $w = 0$ over the xy-plane. Flow in the x and y directions is not restricted, so the symmetry boundaries are essentially free-slip conditions.

The mould walls are represented by nodes with a stationary boundary condition, where $u = v = w = 0$. This prevents gas or polymer from crossing the boundary that represents the mould wall. However, the solver discriminates between gas and polymer by allowing free-slip of the gas against the mould wall, but imposes a non-slip condition for the polymer. The reason for this is that in practice the mould is filled with gas (air) before the polymer is injected and the

melt needs to displace the gas from the mould wall in order to make contact with the wall and form the specimen shape. As the melt moves by convection alone, non-slip boundary conditions would prevent melt from reaching the walls.

6.2.2 Mesh density

Linear quadrilateral elements (or brick elements) are used to mesh the specimen geometry. A mesh generating code is run on an input file (journal file) containing the meshing instructions. This includes the geometry of the specimen, elements density and boundary conditions. The required density of finite elements is determined by running a test for solution convergence, that indicates when the solution does not change significantly with increasing elements. This will provide an efficient mesh that is a compromise between solution accuracy and time for solution. The measure used for the convergence test is predicted wall thickness.

A 2D model has been used to conduct an initial convergence test where the ratio of element length to height is maintained to approximately 3. The results of the convergence test are shown in figure 6.2. The test suggests that 12 elements in the y-direction are a good compromise between solution accuracy and time for solution. The change in wall thickness prediction is not great as the number of elements increases to above 12. The change observed may be due to rounding errors in the calculations resulting from an increase in the number of nodes in the model, as well as the effects of discretisation on the rapidly changing concentration values.

The mesh density in regions of high variable gradient is increased to resolve

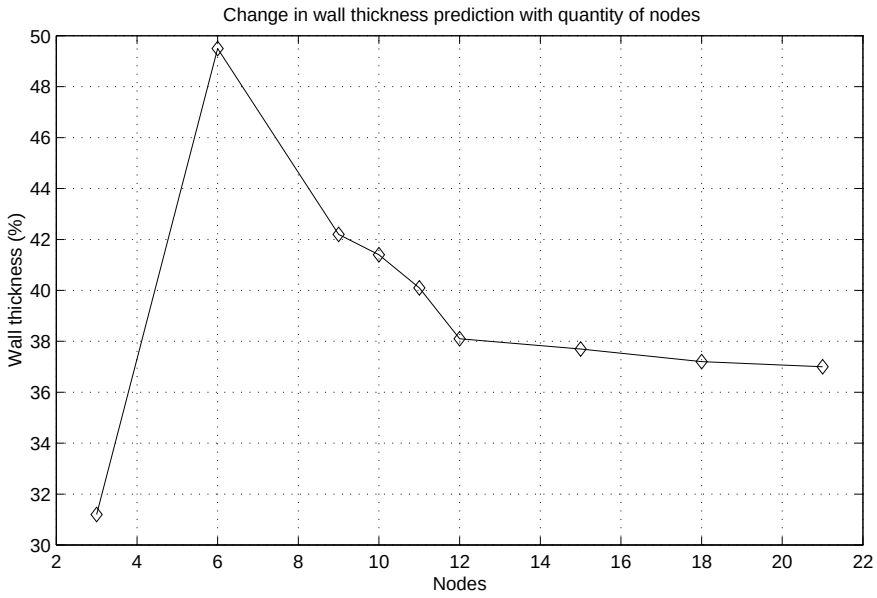

Figure 6.2: The number of nodes in the y-direction (see figure 6.1) are increased and the wall thickness calculated. The aspect ratio of the x to y dimension is maintained at approximately 3.

the changes. The mesh density is increased around the entry into the gauge length, where the flow is developing. Elements against the wall of the cavity are made smaller since the temperature gradient is generally highest in this region.

6.2.2.1 Numerical instabilities

Many simulation variables contribute to the simulation towards giving a reliable result. However, limitations are imposed on the simulation in the form of computational resources and the capabilities of the numerical solvers.

By far the greatest restriction on any simulation, particularly 3D, is the number of elements that can be used in the model. Mesh density influences the accuracy of the solution and the time taken to solve the model. Clearly some compromises have to be made in order the obtain simulation results that can be

used for validation purposes.

Figures 6.3 and 6.4 show the residual wall thickness formation at a position half way along the gauge length. Filled contours above the concentration of 0.5, relating to melt, are displayed along with the FE mesh. At the top of the frame is the residual wall thickness in the large dimension of 7.5mm (relating to the LHS and RHS walls). The bottom of the frame shows the residual wall thickness in the short cross section dimension of 5.0mm (relating to the FIXED and MOVING walls).

It is clear from figure 6.3 that some flow instability exists along the wall in the shorter dimension (z-direction that relates to the FIXED-MOVING wall). The wavy formation maps onto the mesh in the x-direction, which would indicate that the instability is linked to the form of the mesh. More elements along the short dimension would improve the result and reduce the waviness of the gas/melt interface. The mesh density in the short dimension is 1.2 elements per mm and in the large dimension (y-direction that relates to the LHS-RHS wall) 1.5 elements per mm. The flow along the plane of the larger dimension is therefore better resolved spatially.

The numerical solver used to solve the linear equations places a restriction on the number of elements in the mesh. The bandwidth of nodes that the solver can accommodate limits the mesh density. The mesh shown in figures 6.3 and 6.4 is at a limit of refinement for the computer and solver used.

However, the instability is more pronounced at higher flow rates; a reduction in time step has been implemented, but to no avail. Also, an increase in delay

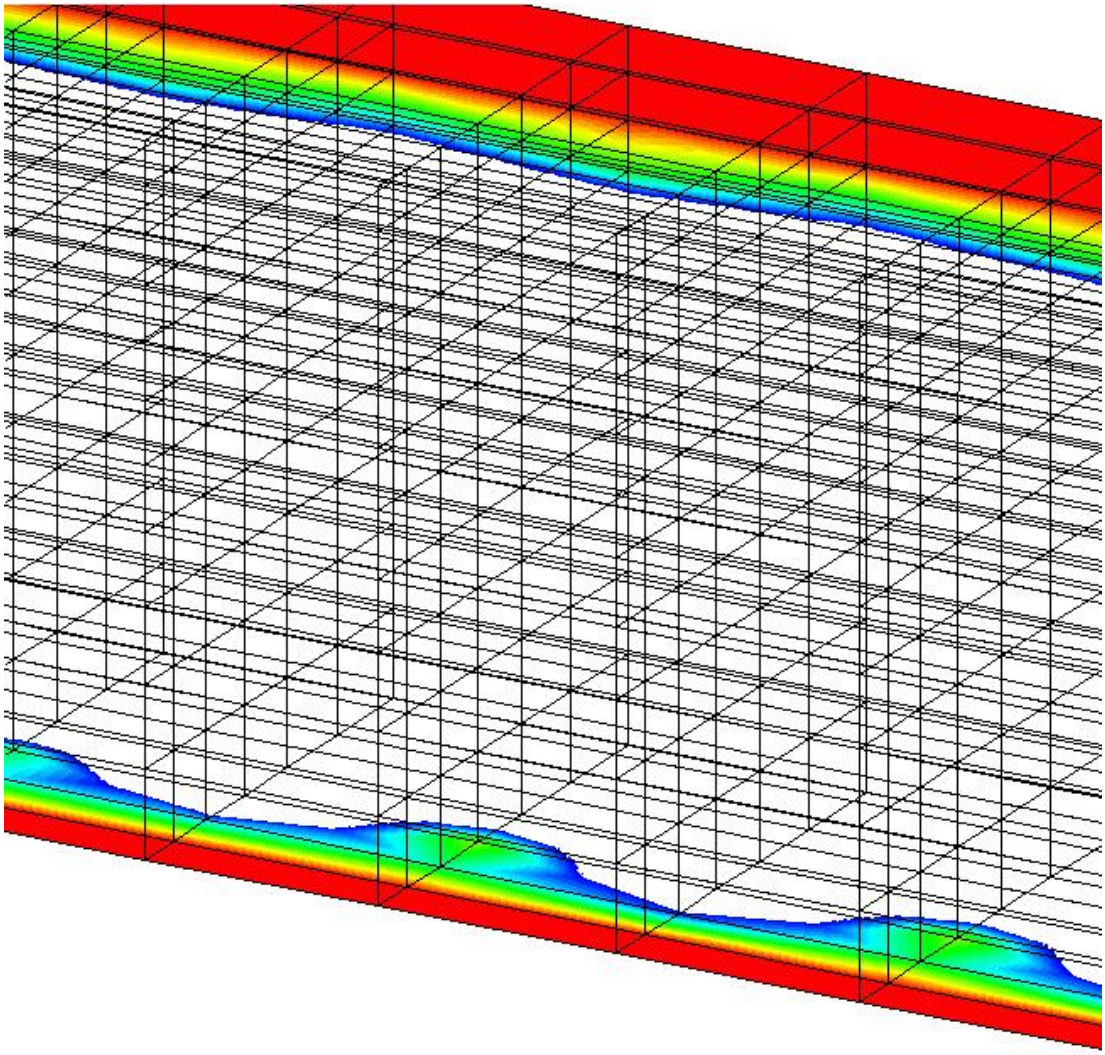

Figure 6.3: The wall thickness prediction is affected by flow instability; the instability appears to map onto the the FE mesh. The flow rate here is set to $25\text{x}10^{-6}$ m^3s^{-1} and the delay time is set to 0.05 sec.

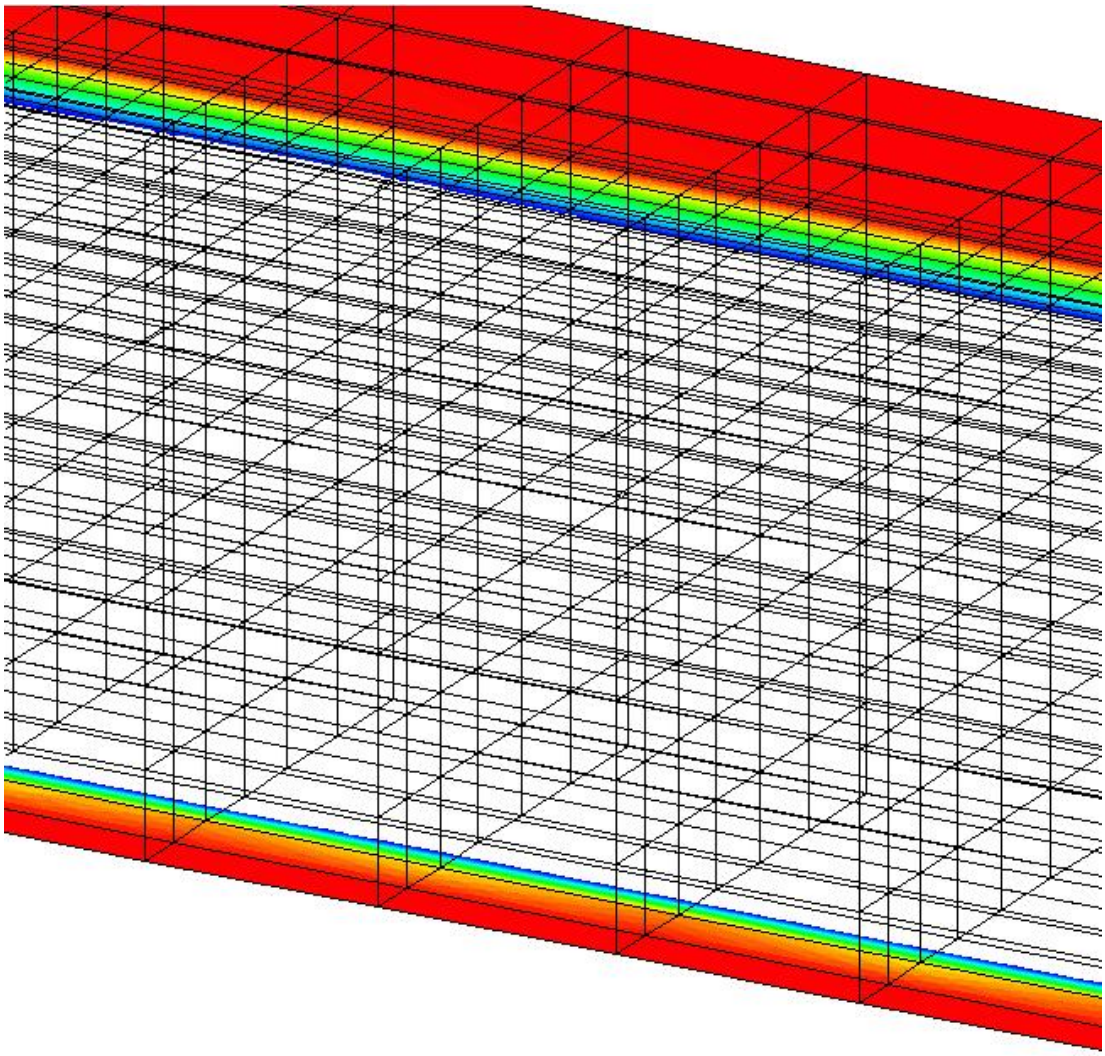

Figure 6.4: The flow instability is reduced at higher delay times. The flow rate here is set at 25x10^{-6} m^{3}s^{-1} and the delay time is set to 2.0 sec.

time tends to smooth the concentration surface as can be seen by comparing figures 6.3 and 6.4. This is likely to be due to an increase in viscosity as the melt cools near the wall, which reduces the velocity gradient near the wall.

6.2.3 Half and full geometry models

An important factor related to modelling is the time for solution. The length of time to complete an iteration of the flow solution increases with the number of elements in the model. The time for solution is related to the following parameters,

$$Time\ for\ solution\ =\ nb^2\ \times\ m \tag{6.1}$$

where, n is the number of degrees of freedom, b is the bandwidth and m is the number of time steps [73]. Therefore, steps are taken to reduce the solution time by minimising the number of elements used in the model.

Typically, the output of interest from the simulation is the predicted residual wall thickness at a point of fully developed flow along the gauge length. The testing of models that covers the whole length of the specimen have shown no significant difference in the predicted wall thickness compared with models that cover only half of the specimen length. The use of a half-model is only useful for predicting wall thickness and not bubble penetration, but the saving in the required number of elements is significant. In practice, the half model leaves room for an increase in the mesh density in order to improve solution accuracy.

The half model that covers upto half way along the gauge length from the gas and melt injection end of the specimen is shown in figure 6.1. The full model that

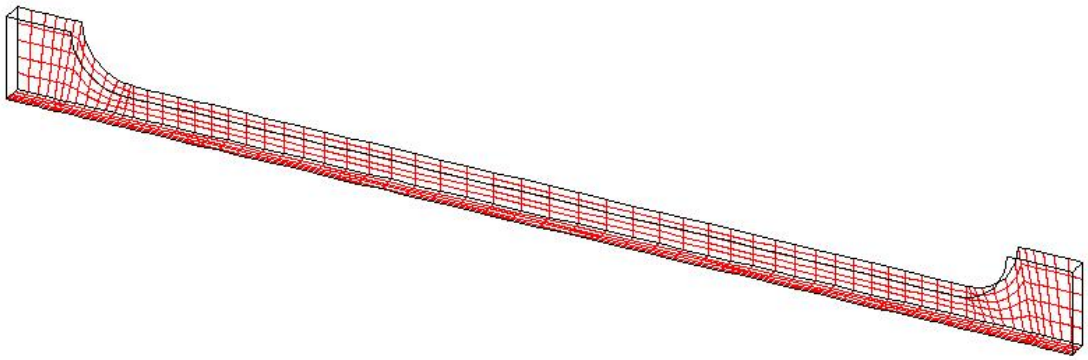

Figure 6.5: The full specimen gauge length and end tab is modelled

is used to check the validity of the half model and covers all of the gauge length and the end tab is shown in figure 6.5. The geometry of the model is defined in SI units.

6.3 Flow modelling implementation

6.3.1 Initial flow conditions

The cavity modelled by the simulation can initially be filled either with polymer melt or with gas. This is achieved by initialising the concentration value at each node to be either 1.0 or 0.0 for polymer or gas respectively. In the real process melt is injected into the cavity first and at some time later gas is injected to complete the filling of the mould. The simulation provides scope to change this.

A simulation result from a simple 2D model is shown in figure 6.6. This result replicates the real cavity filling sequence where polymer melt partially fills the empty cavity (fig 6.6a), then some time later the melt flow ceases and gas is injected (fig 6.6b) and finally the gas bubble advances enough to fill the mould

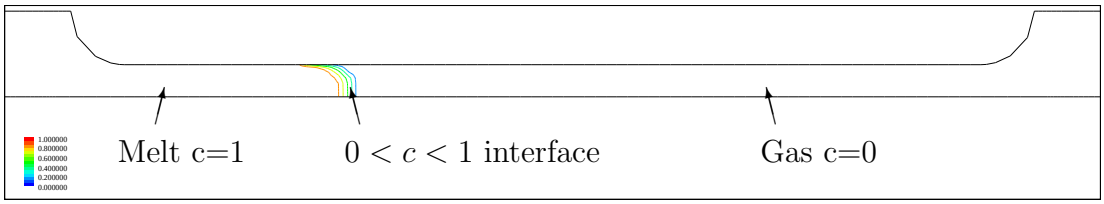

(a) Melt flow into an empty cavity

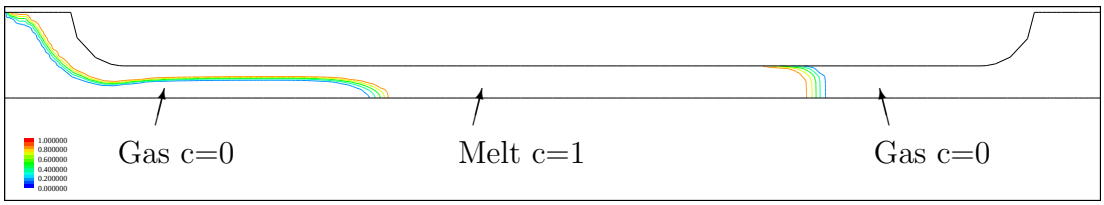

(b) The flow switches to gas to continue filling

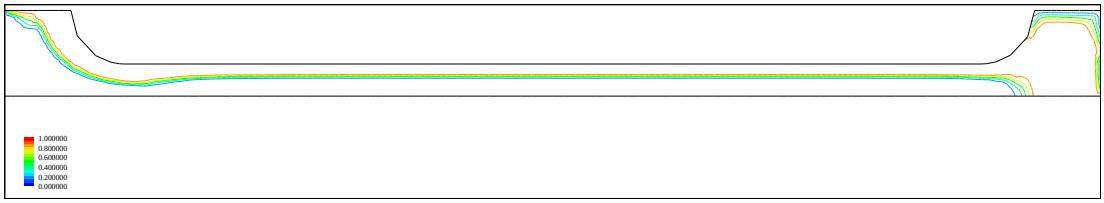

(c) The melt is forced to fill the mould

Figure 6.6: The progress of mould filling using results from a 2D simulation.

extremities with melt (fig 6.6c).

In figure 6.6 the flow of polymer and gas is controlled by setting a velocity at the nodes that lie along the left hand wall. The concentration value at the nodes determine if melt or gas is convected through the mesh.

An alternative approach, valuable in 3D simulation, is to initialise nodes within the model to a concentration of 1.0, to represent melt. This in essence mean that the mould is already filled with melt and the injection of gas can begin at any time. Results from a 3D analysis can be seen in figure 6.8. A saving on computer time can be made if the solution to the melt filling the cavity is not needed. This assumes that the flow of heat from the melt during the melt filling stage is insignificant. Evidence for this is the continuity in wall thickness along the gauge length observed experimentally that infers that the melt rheology does not change significantly during bubble penetration. Also, the time scale of bubble penetration is likely to be less that 0.5 seconds. Therefore, the most significant time that melt cooling can effect the predicted wall thickness is during the delay time between the end of melt injection and the start of gas injection and during bubble penetration.

6.3.2 Exit flow

In the GAIM process the polymer melt is contained within the mould cavity. Air that is in the cavity before melt filling is allowed to vent from the tool through properly constructed air gaps. This situation is complex to simulate since some provision for an air vent needs to be made within the mesh. Ideally, specific nodes

at the end of flow need to discriminate between gas and polymer to allow gas to escape, but prevent polymer from passing. The ideal situation of discrimination nodes is not implemented, so material is either allowed to pass through the end wall un-hindered or a vent hole is implemented through specific nodes on the end wall that allow melt to pass through; the higher viscosity of the melt means that the polymer flow encounters greater resistance than gas flow through the vent hole.

The vent hole is implemented by specifying a non-slip boundary condition for all surfaces that represent the cavity wall. The boundary condition files, generated by the meshing application, are then manually edited to remove selected nodes from the non-slip condition. This effectively forms a vent hole, the size of which is determined by the distance to the nearest wall nodes.

Within this thesis the flow is not restricted at the exit of the mesh that forms the half-length specimen. The bubble penetration is not meaningful in this half-length model and melt fills the model initially. In the real process the flow of melt to the end wall is unrestricted, so remains as such in the simulation.

The exit from the 3D half model is shown in figure 6.7. This is a point in the simulation where the gas bubble is approaching the end of the flow length and is indicated by the concentration contours. The small arrows show the velocity field of the melt and the larger arrows indicate the gas flowing at higher velocity.

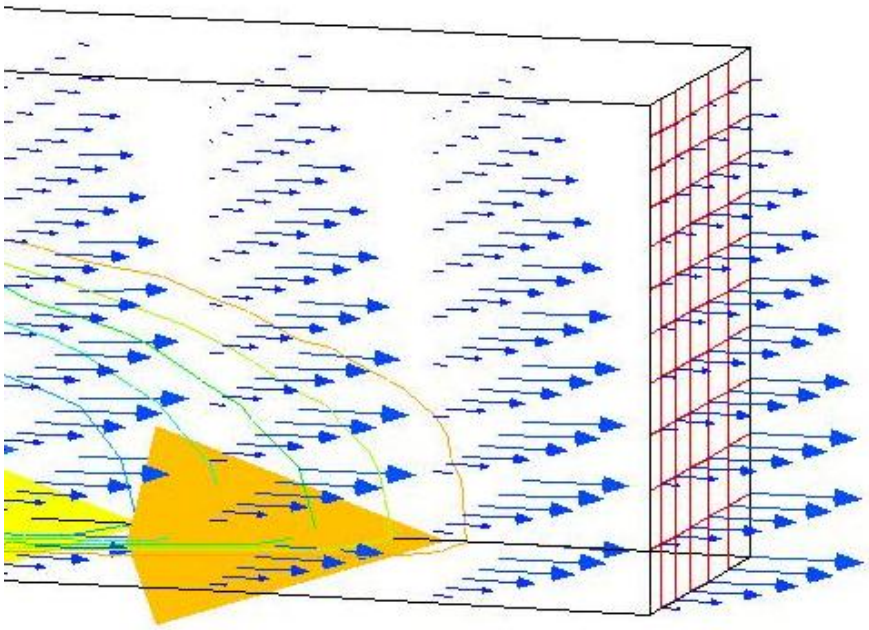

Figure 6.7: Material flows out of the mesh at the cavity extremity

6.3.3 Methods for gas injection

In the actual GAIM process the gas is injected into the melt through either a needle placed within the mould or through a specially adapted nozzle fitted to the end of the machine barrel. The simulation can replicate gas injection in a number of ways, from a simple flat velocity profile at an inlet wall to a small source placed within the mesh to represent the gas needle placed within the mould.

The methods used in the simulation to represent gas injection into the polymer melt are shown in figure 6.8. The filled contour shown represents concentration values above 0.5, which represents polymer melt. This allows the gas/melt interface to be seen clearly.

Figure 6.8a shows the simplest method of injecting gas, where a flat velocity profile is set along the inlet wall. Clearly, a flat velocity profile across a section

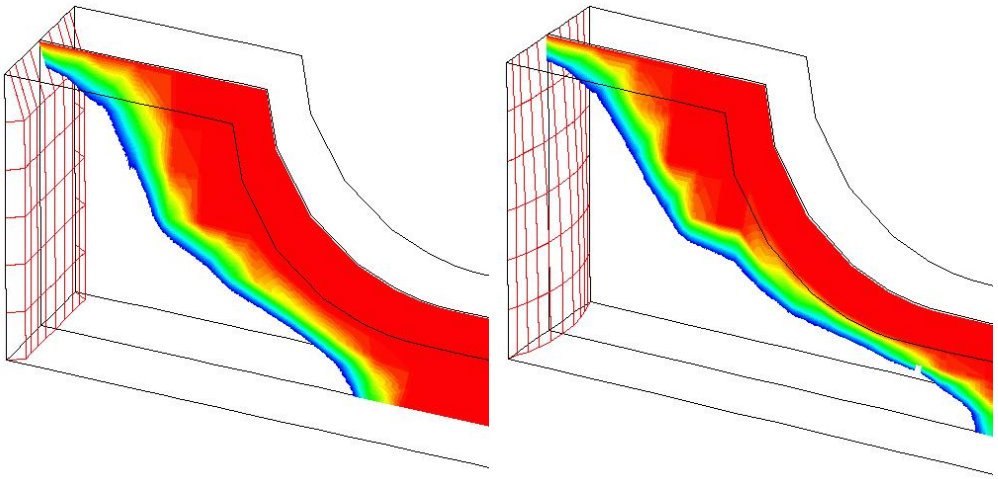

(a) Flat inlet profile

(b) Parabolic inlet profile

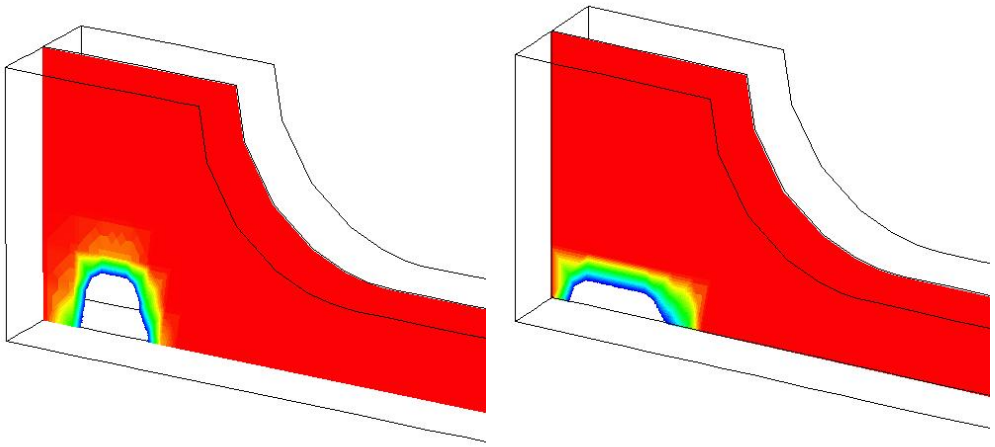

(c) Element gas source

(d) Gauss points gas source

Figure 6.8: Methods for injecting gas into the melt.

is unrealistic and a higher velocity is expected at the centre of the flow. A progression from the flat profile is the two-dimensional parabolic profile, shown in figure 6.8b. The parabolic profile is fitted to a polynomial that is second-order in two-dimensions and that relates the position on a plane to a velocity. The parabolic gas injection profile provides a smoother gas melt interface, particularly near the walls where the forced velocity gradient is less steep compared with the flat profile (which must abruptly change to zero).

The flow of gas from the injection needle is more accurately represented by using a "point" source. Figures 6.8c and 6.8d show a point source provided by a single element and by Gauss points within a spherical region respectively. The single element tends to provide a surface of concentration gradient that is rectangular in shape due to the shape of the source element. In practice, this tends to give velocity jets around the element that affects the shape of the flow further downstream.

The sphere of Gauss points provides a much smoother surface of concentration gradient emanating from the flow source. Therefore the effect on the flow further downstream is minimised and the flow pattern from the gas injection needle is approximated well.

6.3.3.1 Control of the gas injection rate

The strength of the gas source from a point source is specified directly in the simulation control file that is read by the flow solver. The source strength is specified in $m^3 s^{-1}$, so the gas injection is driven by an increase in the volume of

gas.

Since the fluid contained within the model is incompressible the volume of fluid entering the system is equal to the volume of fluid leaving the system. This principle is used to check that the flow rate setting for the gas source is accurate after discretisation.

The volumetric flow rate of material flowing along the gauge length can be determined by analysing the velocity vectors at the nodal positions over the cross section. Figure 6.9a shows the velocity vectors over the end wall of the specimen cross section. The velocity is averaged over the element bound by the 4 nodes and the volumetric flow rate for that element is determined. Summing all element flow rates over the section provides the total volumetric flow rate. Equation 6.2 describes the method used to check the volumetric flow rate,

$$\dot{Q} = \sum_{e}^{e} \left(\frac{1}{4} \sum_{j=1}^{j=4} u_j \right) \Delta x_e \Delta y_e \tag{6.2}$$

where, u is the nodal velocity in the x-direction, j is one of four nodes bounding the element i, Δx_e and Δy_e are the x and y dimensions respectively of the element j. The method of equation 6.2 assumes the cross section lies normal to the x-axis.

The result of checking the flow rate is shown in figure 6.9b, where the simulation runs through a delay time for 10 iterations before the flow of gas starts. The source flow rate is set at 7x10^{-6} m^{3}s^{-1}, which is confirmed by the calculated flow rate over the cross section.

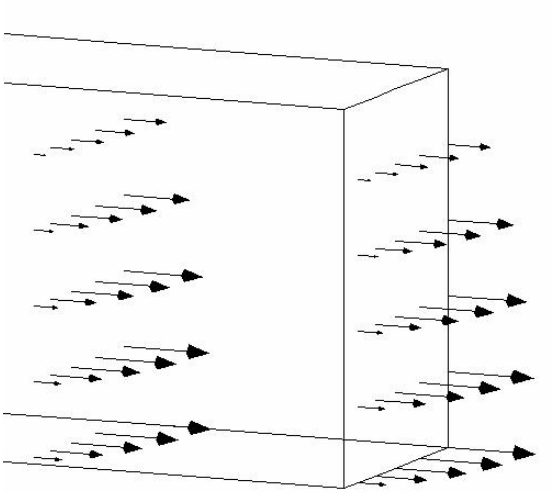

(a) Velocity vectors over a cross section

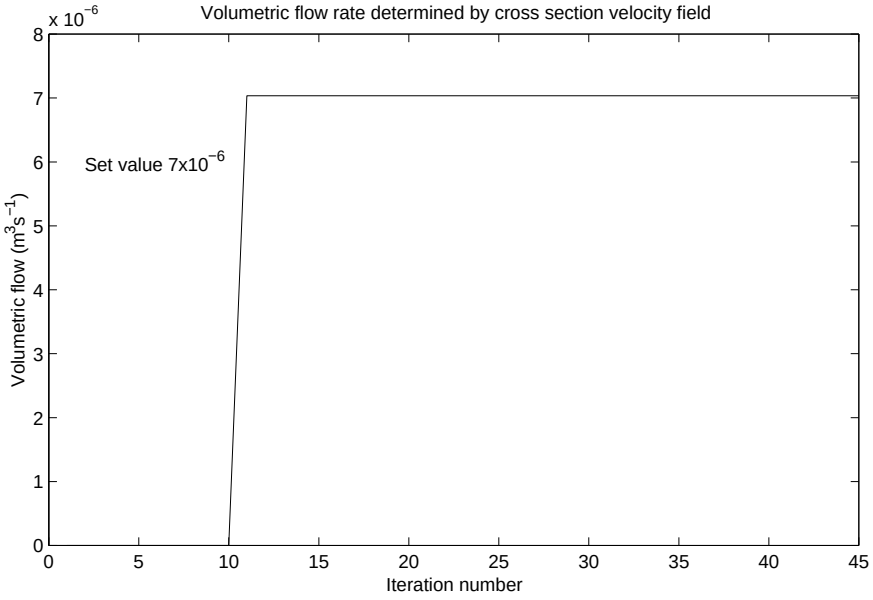

(b) Calculated volumetric flow rate

Figure 6.9: Checking of the volumetric flow rate setting for gas injection.

6.3.4 Flow velocity profiles

The flow velocity profile at a point within the gauge length changes as the gas bubble front passes. Figure 6.10 shows the change in velocity profile as the gas bubble front passes through the frame of reference. The frame of reference is in the centre of the flow on the xy-plane in a region of steady state along the gauge length.

In figure 6.10a the gas bubble is seen approaching from the left and the velocity profile through the melt is approximately parabolic. The velocity near the wall at the top of the frame is relatively low and at the wall the velociy is zero, which is a non-slip boundary condition. After the gas bubble has passed through the frame of reference, which is shown in figure 6.10b, and a residual wall thickness remains the velocity profile across the cavity changes. Flow velocity within the wall is virtually zero and nearly all of the flow takes place within the gas bubble.

The change in velocity profile is quantified in more detail by plotting the nodal values of velocity in the x-direction, which is u-velocity. Figure 6.11 shows the bubble tip as it passes the nodes from which velocity values are taken. Velocity profiles are plotted in figures 6.12, 6.13 and 6.14 that are relevent to the gas bubble approaching, coinciding and passing the point of reference respectively. Velocity profiles at the same gas source flow rate, but delay times of 1.0 and 10.0 seconds are compared.

As the gas bubble approaches the point of reference (fig 6.12) the velocity profile shows that the flow in the centre of the melt for a delay time of 10 secs is higher than for a delay time of 1.0 secs. The reason is that the flow near the wall

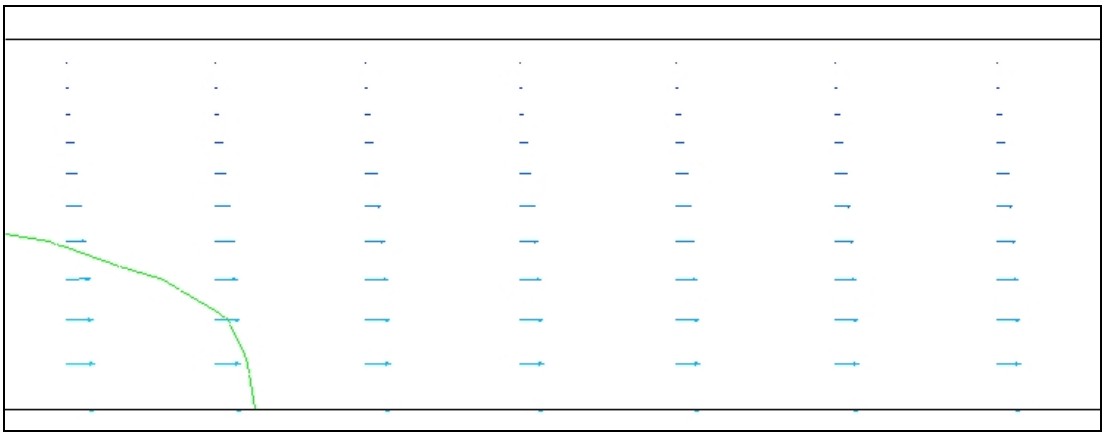

(a) Before bubble front passes

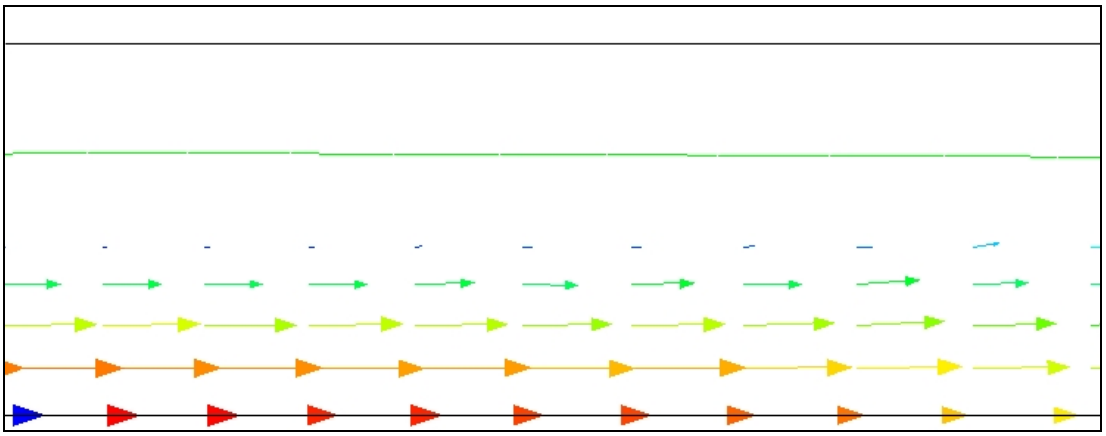

(b) After bubble front passes

Figure 6.10: Material velocity profiles before and after the gas/melt interface. The interface is moving in the direction of the arrows that indicate the velocity vector.

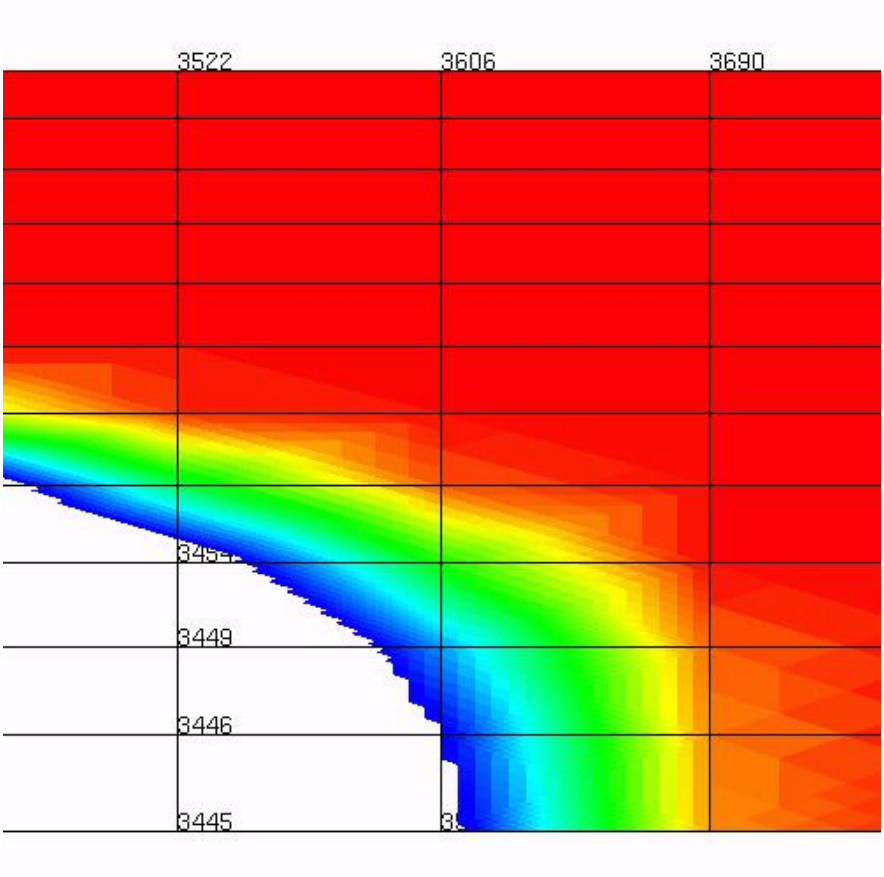

Figure 6.11: As the bubble tip passes the velocity profile in the x-direction is taken from node 3606 at the cavity wall down to the centre line of flow.

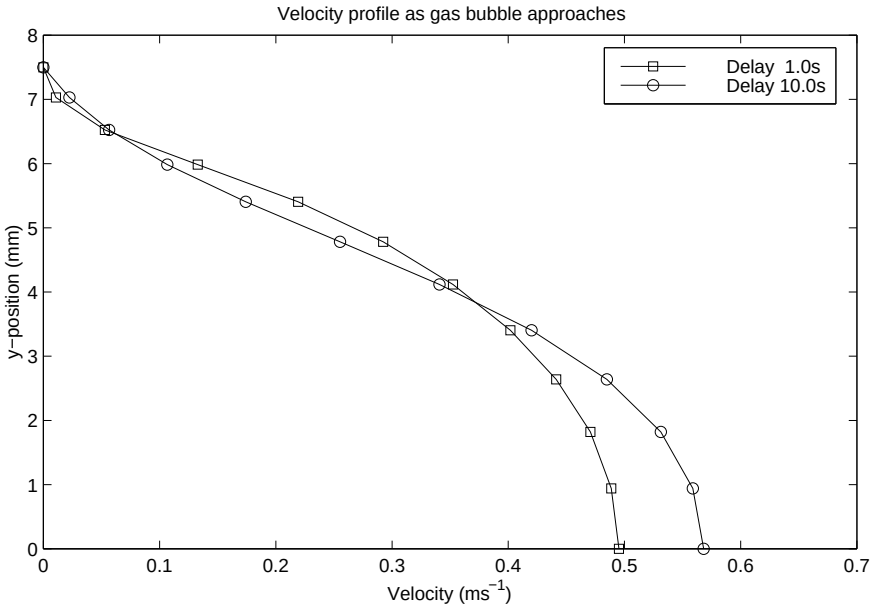

Figure 6.12: Velocity profile across the cavity as the gas bubble approaches

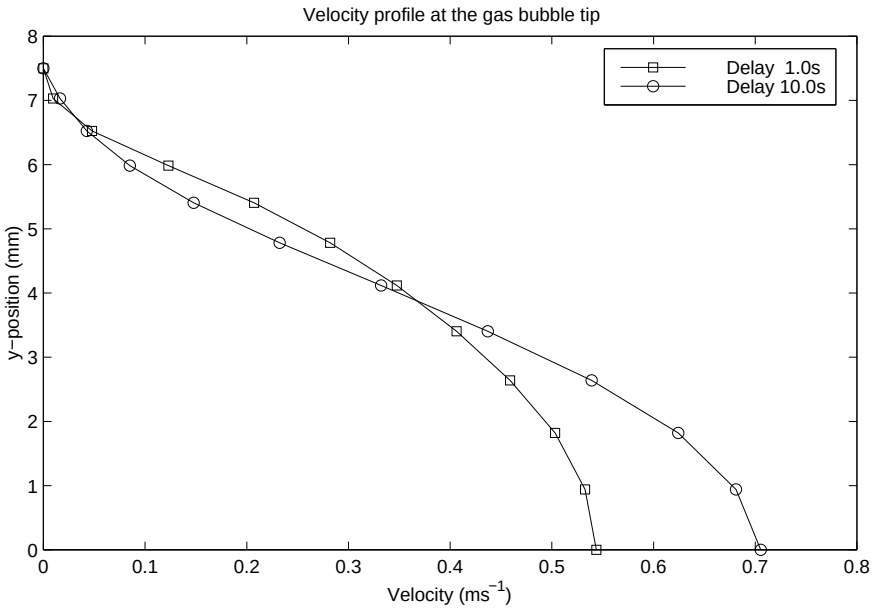

Figure 6.13: Velocity profile across the cavity at the gas bubble tip

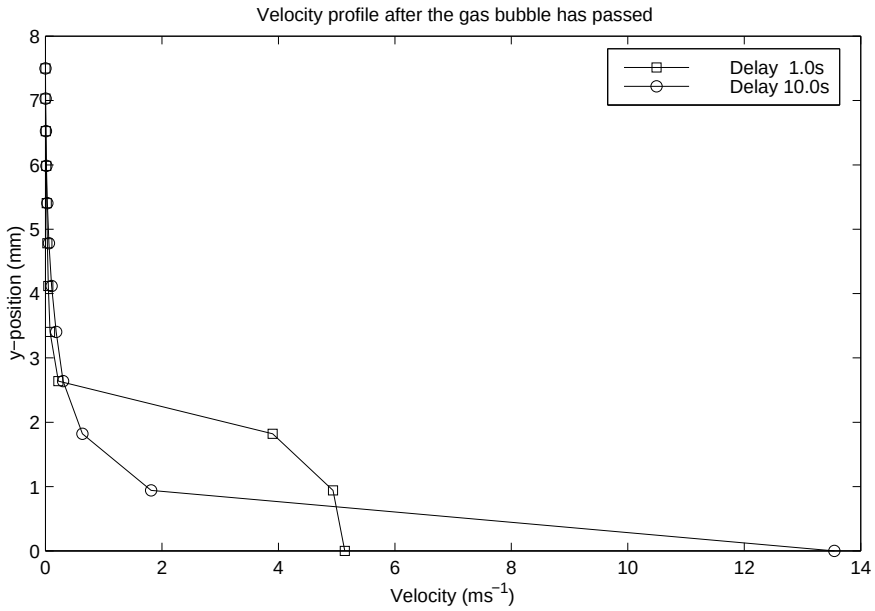

Figure 6.14: Velocity profile across the cavity when the gas bubble tip has passed.

is at a lower velocity because the delay time has reduced the melt temperature and therefore has increased the resistance to flow.

As the gas bubble reaches the point of reference (fig 6.13) the flow velocity profile changes. The lower viscosity fluid in the centre of flow forces and increase in the velocity at the centre and sees a reduction in the velocity nearer to the wall.

Finally, once the gas bubble has passed, the velocity profile takes on the form shown in figure 6.14. Here, the flow velocity is dominant within the gas bubble. There is a clear distinction between the two delay times as the velocity at the centre line node is much higher for the longest delay time. This plot indicates that once the residual wall is formed it does not move significantly compared to the progress of the bubble front.

The viscosity of the gas is at least 3 orders of maginitude less than the viscosity of the melt. Therefore, the lower resistance to flow facilitates the higher flow rate within the gas. The flow rate from the gas source is fixed and is driving the flow in the system.

It will be seen in a later section that the residual wall thickness increases as the delay time increases. This is reflected in the experimental results. The velocity profile before and after the bubble is also influenced by the delay time. Figure 6.15 shows the velocity at a node that lies on the centre line of flow, which is at the bottom of the frame of reference seen in figure 6.10.

The velocity plotted in figure 6.15 is that of the melt before the approaching gas bubble has passed. As the delay time increases the temperature of the melt nearest to the wall decreases and this melt cooling causes the viscosity to increase. The temperature profile is discussed further is section 6.3.6. The melt in the centre of flow is forced to flow faster and as the higher viscosity layer of melt, near the wall, increases in thickness.

6.3.5 Melt viscosity model

The viscosity of the melt within the simulation uses a modified Cross-WLF model. The dynamics of the model are discussed in more detail in section 5.3.5. The Cross-WLF model describes the viscosity of the melt under given temperature and shear rate conditions. The model is commonly used by respected researchers in polymer melt flow, e.g. Tucker et. al. [65, 66].

Rheological data for the melt has been generated off-line using a Rosand RH7

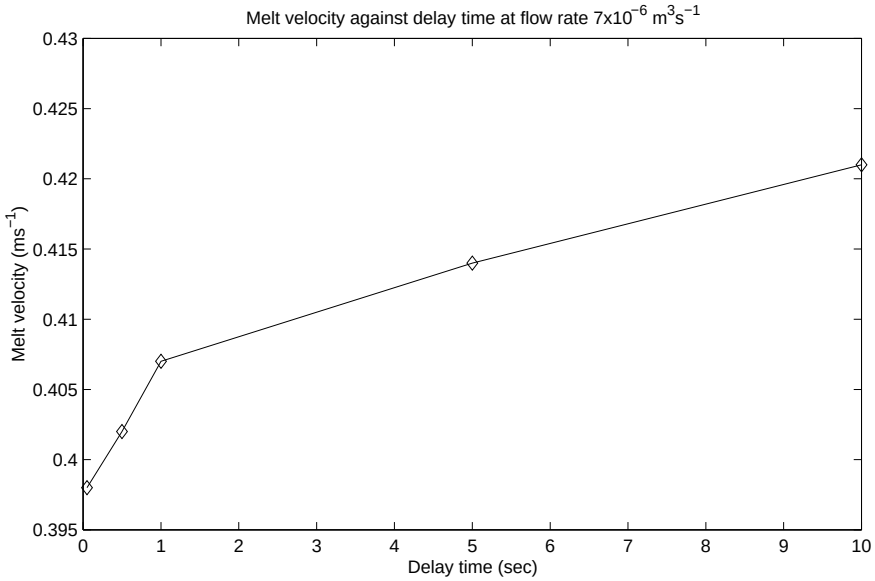

(a) Flow rate Q=7x10^{-6}m^{3}s-1

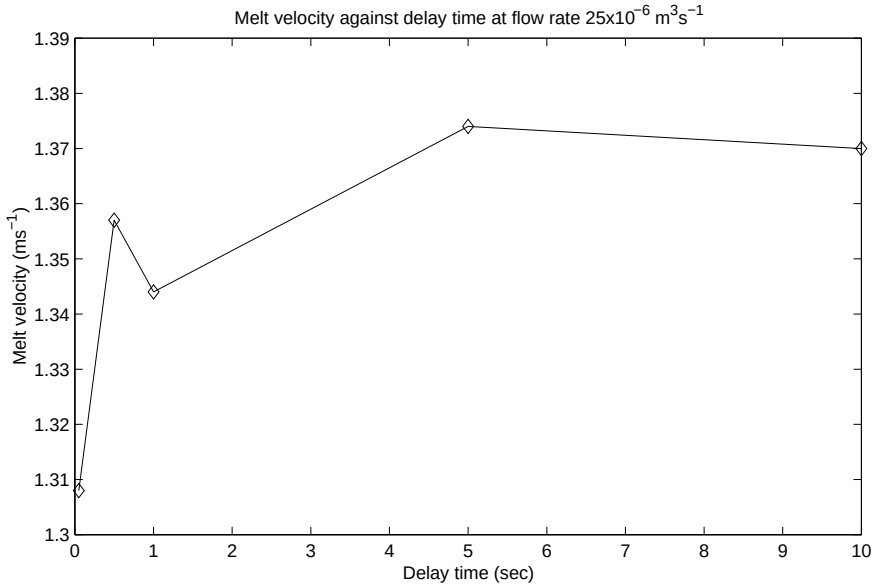

(b) Flow rate Q=25x10^{-6}m^{3}s-1

Figure 6.15: These figures indicate the melt u-velocity just ahead of the bubble front. The velocity increases with increasing delay time and increasing gas source flow rate.

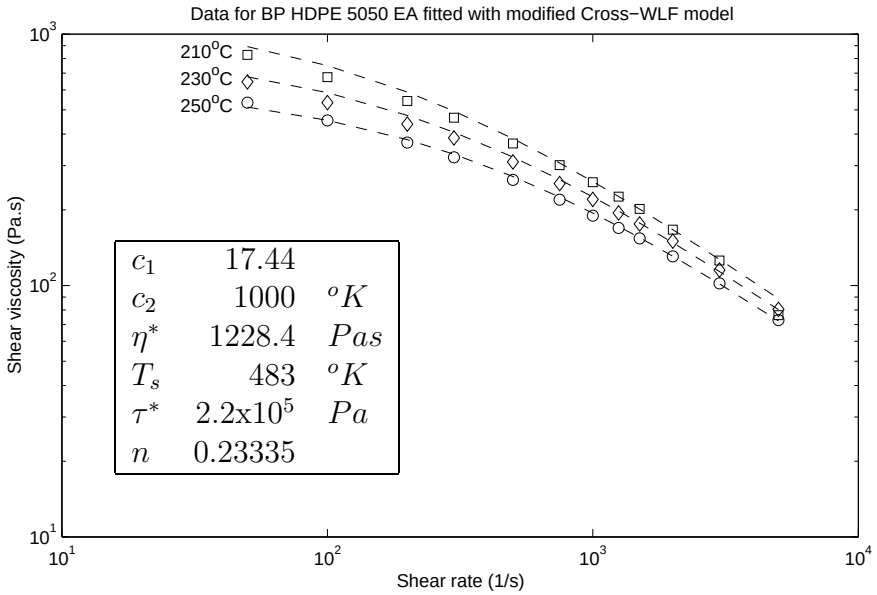

Figure 6.16: BP HDPE 5050EA melt viscosity fitted to a modified Cross-WLF model

off-line rheometer [74]. A modified Cross-WLF model is fitted to the rheological data using the rheological model module within the Compuplast Flow 2000 software. The values for the model parameters and a plot of the model fit is shown in figure 6.16.

6.3.6 Thermal effects within the model

The modelling of melt cooling is driven by the temperature boundary condition set on the mould wall. Over time, particularly during the delay time, the temperature of the melt reduces. Figure 6.17b plots the temperature of the nodes in the y-direction on the symmetry plane at a point 50mm along the gauge length, where wall thickness measurements are taken. The nodal positions over which the temperatures are noted are shown in figure 6.17a, which is taken from the

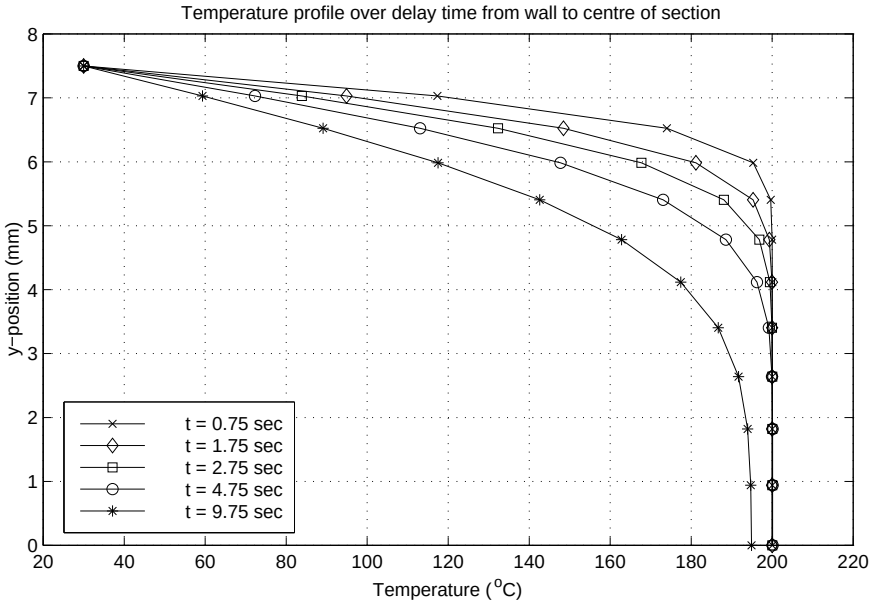

Figure 6.17: The simulated temperature profile through the melt through a 10 sec delay time. The wall temperature boundary condition (y=7.5mm) is fixed at 30°C . The initial melt temperature is 200°C

post processor and shows concentration lines that indicates the melt/gas boundary. The temperature profile over the 12 nodes show a high thermal gradient exists in regions near the mould wall. In the simulation the mould wall is set to be 30°C and fixed by a boundary condition. The temperature of 30°C since it is the lowest recommended tool temperature setting for the tool during processing [59]. The lowest tool temperature setting is used in production, if possible, to give the shortest cooling time and hence shortest cycle time. Within these tests the wall temperature is one of the fixed parameters. The temperature profiles in figure 6.17 are taken from a simulation that uses a 10 sec delay time between the start of the simulation and the start of melt injection. The wall is at the y position of 7.5mm in the simulation model.

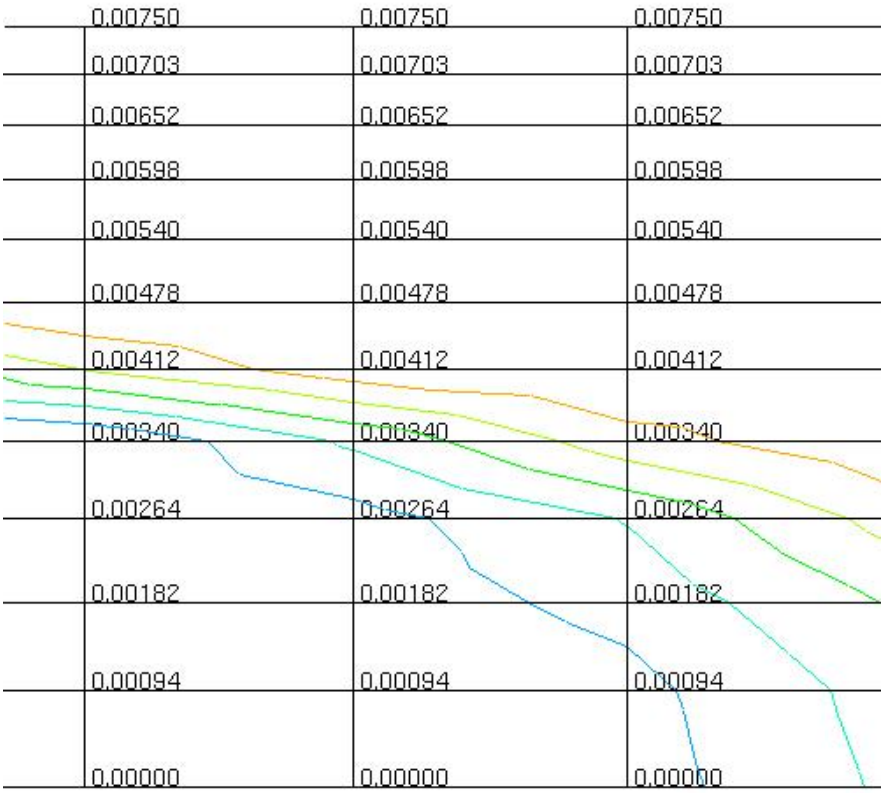

Figure 6.18: The nodal positions (metres) in the y direction from which nodal values, such as temperature and concentration, are taken

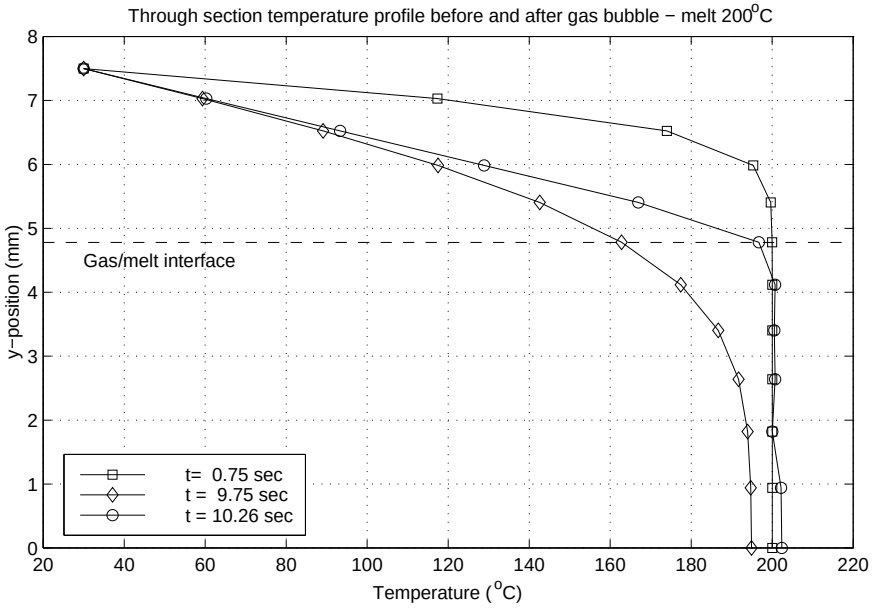

Figure 6.19: Melt temperature set to 200°C .

The temperature profile changes over time, such that the temperature near the wall reduces as heat is removed from melt within the cavity. The effect of the heat transfer is to increase the viscosity of the melt nearer to the wall. The effect of temperature in the melt viscosity model is outlined in section 6.3.5. During the delay time period, while a no-flow situation exists, the shear rate in the melt viscosity model is zero.

A temperature profile for various stages of the cavity filling simulation at set melt temperatures of 200°C , 210°C and 250°C are shown in figures 6.19, 6.20 and 6.21 respectively. The temperature profiles, for each melt temperature setting, are taken 0.75 sec, 9.75 sec and 10.25 sec into the simulation. The temperature profile is through the melt and gas bubble at the start of the simulation (t=0.75s), at the end of delay time (t=9.75s) and after the gas bubble is passed

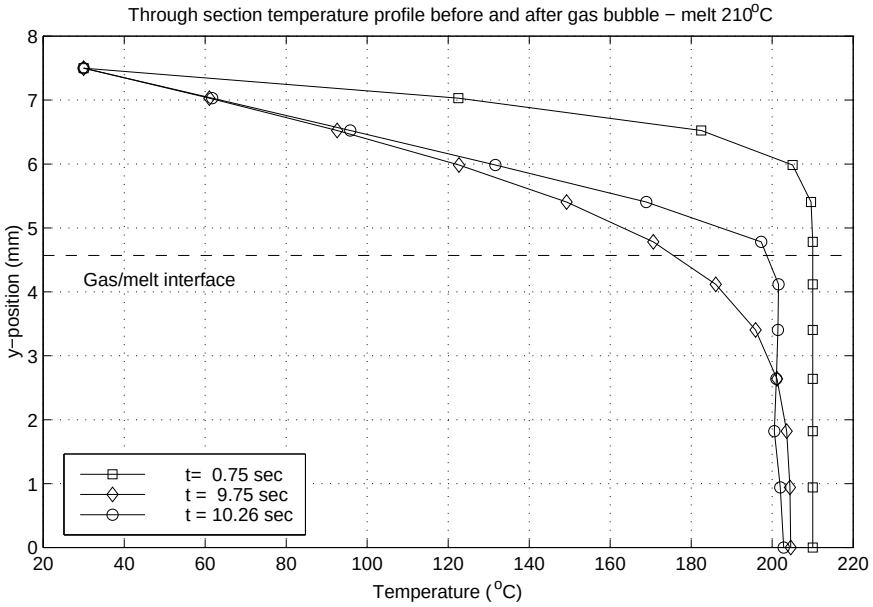

Figure 6.20: Melt temperature set to 210°C .

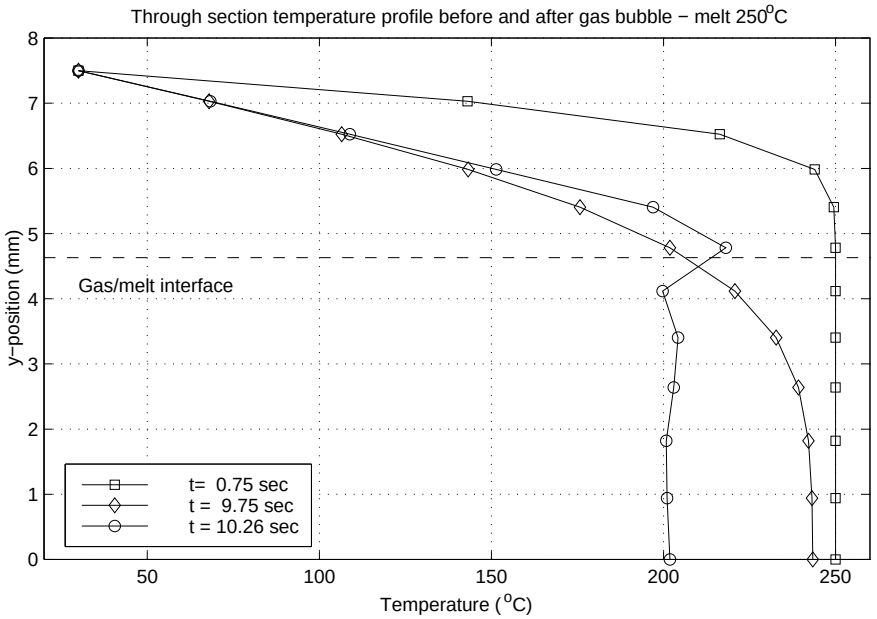

Figure 6.21: Melt temperature set to 250°C .

through (t=10.25s). The gas temperature is set at 200°C in every case and the gas/melt interface that represents the residual wall thickness after the bubble has passed is shown.

The temperature profile progression during delay time seen in figure 6.17 is observed in figures 6.19 to 6.21 during the delay time period from 0.75 to 9.75 seconds. After the gas bubble has passed and formed the residual wall the temperature profile within the gas bubble region switches to the gas bubble inlet temperature indicating that there is relatively little heat exchange between gas and polymer. So, where the melt temperature is set to 250°C , as in figure 6.21, the temperatures at the nodes within the gas bubble switches to 200°C . However, since the flow analysis is completed within a relatively short time scale the thermal transfer from the gas bubble to the melt is negligible. The consistency in the wall thickness along the gauge length, observed experimentally, is evidence that significant heat transfer does not take place during the bubble penetration time. If significant heat transfer did take place the wall thickness would be expected to increase toward the end of bubble penetration as the frozen layer of polymer increased in thickness.

Changes in predicted wall thickness are observed when a range of melt temperatures are tested. Predicted wall thickness at melt temperatures of 200°C , 210°C , 230°C and 250°C are plotted in figure 6.22. All other simulation variables are constant, the flow rate at the gas source is $7\text{x}10^{-6}$ m^3s^{-1} and the delay time is 10s. The simulated wall thickness over the temperature range does not appear to follow a definite pattern. The expected result would be for the wall thickness

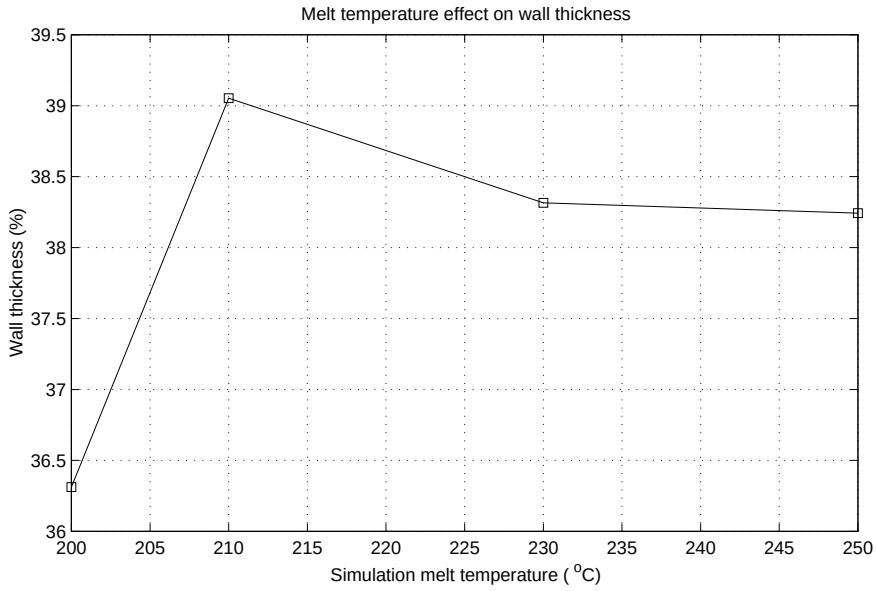

Figure 6.22: Wall thickness change with changes in the melt temperature setting.

to decrease as melt temperature increased; the temperature in the melt near the wall would be higher which slows the thickening of the wall over time.

6.3.7 Time stepping

The criterion used to determine the time step between iterations is split between the flow and delay time phases of the simulation. During the delay time the flow equations are not solved since a no-flow condition exists.

The delay time iteration time step varies depending upon the delay setting. The delay time is normally covered by 40 iterations, which gives time steps that are much smaller than the characteristic time of heat transfer in the model. So a delay time of 10s will use a time step of 0.25s to solve the temperature equation.

The time step used to solve the flow equations is determined by the smallest element size along the gauge length and the speed of flow through that element.

A useful heuristic is that the melt/gas boundary should take at least 5 iterations to cross the smallest element. This allows the boundaries progress to be resolved. In practice the dominant flow is in the x-direction along the specimen length and the highest flow velocity is on the centre line. In order to determine the appropriate time step an estimate is used and the simulation is run. The number of iterations taken for the melt/gas interface to cross the smallest element on the centre line is observed and the time step is adjusted up or down accordingly.

6.4 Comparison of simulation with experiment

6.4.1 Behaviour of the experimental models

An empirical model for residual wall thickness was developed in chapter 4, the experimental results chapter. The model is in the form of regression equations (equations 4.3 to 4.6) that correlate process variable settings to residual wall thickness. The general behaviour of the regression equations, which are a continuous function, for a range of variable settings are shown in figures 6.23 to 6.29.

The fixed and moving wall regression models have been tested and the results presented in figures 6.23 to 6.26. The processing variables present within these regression models are tool temperature (STT), injection velocity (IV), gas pressure (GP) and gas delay time (GD). The effects of the processing variables are the same for both walls, which is to be expected, but the fixed wall (shown dotted) is consistently thinner than the moving wall (shown solid). A possible explanation for the difference in wall thickness is the mould wall temperature on

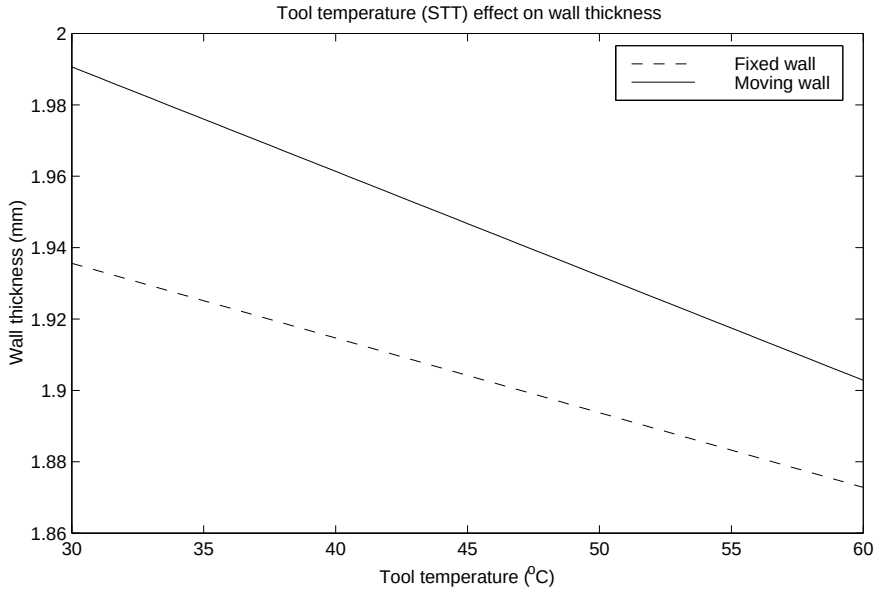

Figure 6.23: The effect of tool temperature on the residual wall thickness at the fixed and moving halves of the mould

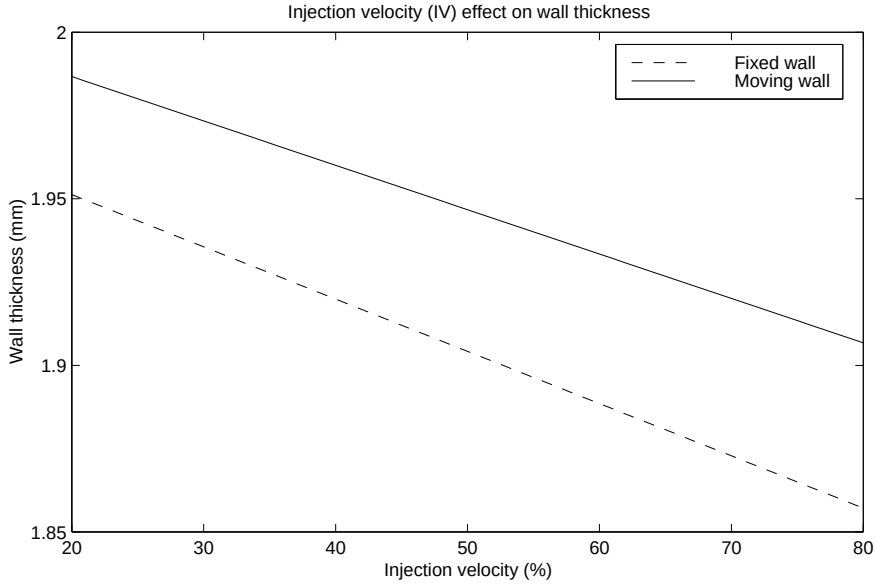

Figure 6.24: The effect of injection velocity on the residual wall thickness at the fixed and moving halves of the mould

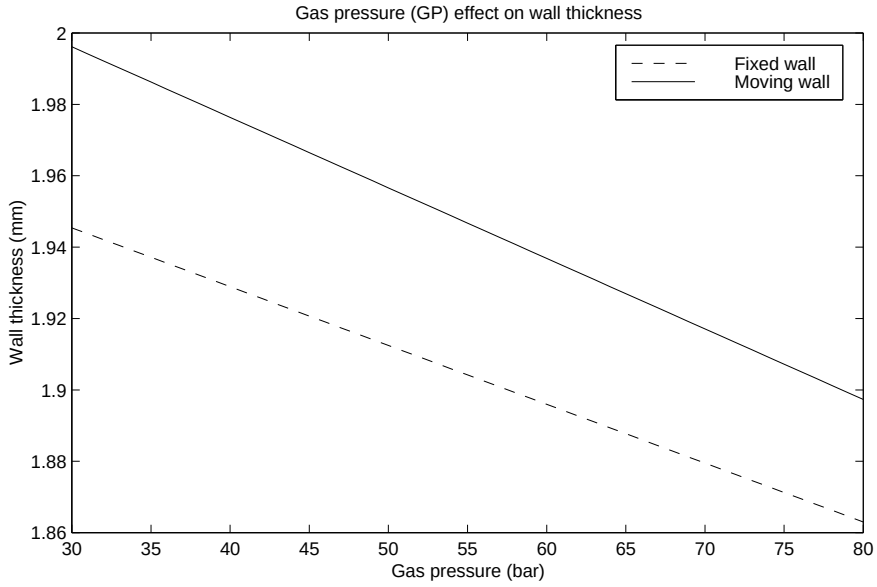

Figure 6.25: The effect of gas pressure on the residual wall thickness at the fixed and moving halves of the mould

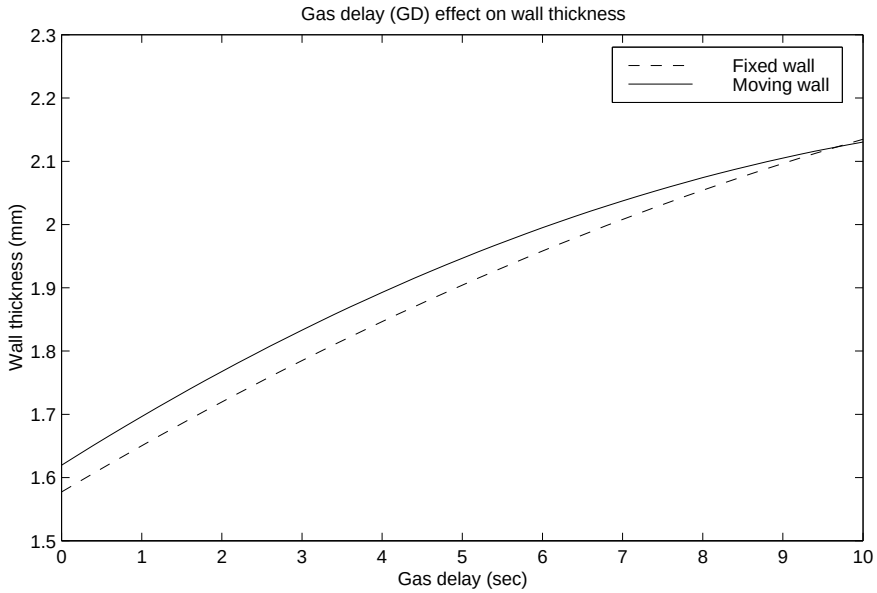

Figure 6.26: The effect of gas delay time on the residual wall thickness at the fixed and moving halves of the mould

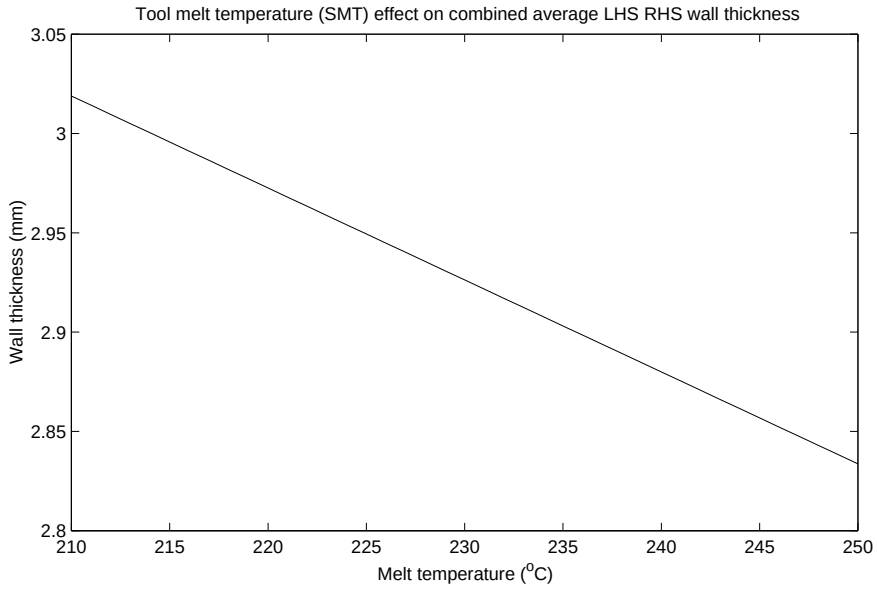

Figure 6.27: The effect of melt temperature on the residual wall thickness over the average LHS and RHS walls

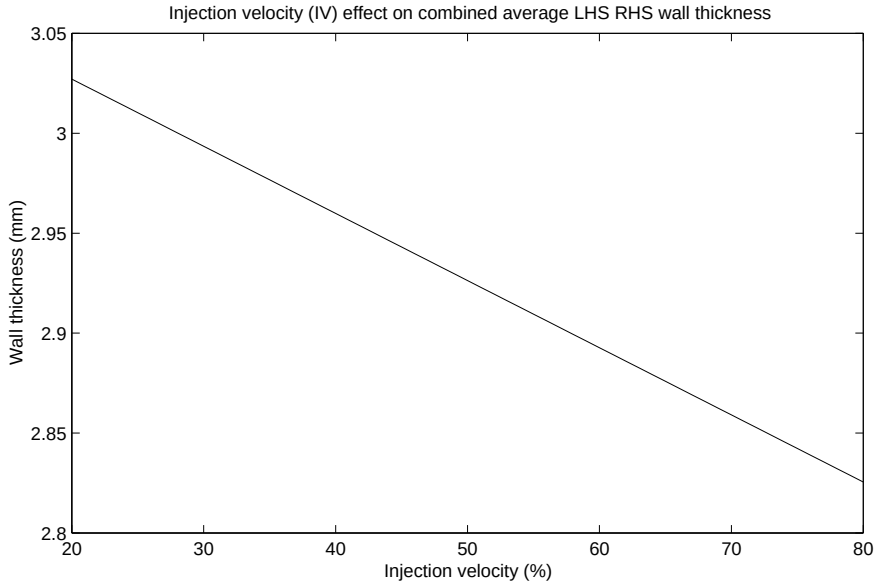

Figure 6.28: The effect of injection velocity on the residual wall thickness over the average LHS and RHS walls

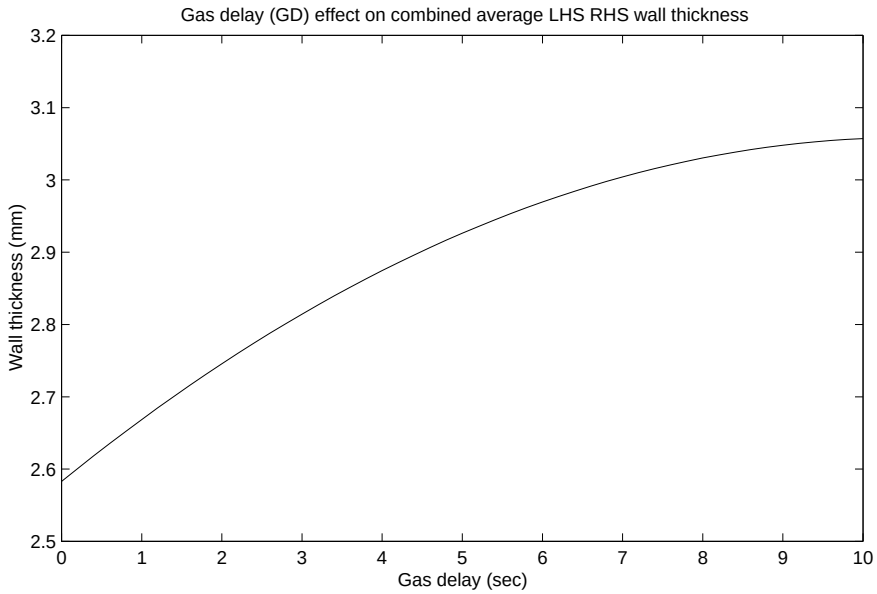

Figure 6.29: The effect of gas delay time on the residual wall thickness over the average LHS and RHS walls

the fixed side is likely to be higher than the moving side since the machine nozzle, which is at 200+°C , is pressed against the fixed half of the mould. However, the mould wall temperature during experimentation is not known so this cannot be confirmed at present. It may be possible to fit thermocouples into a mould in further work to confirm the mould wall temperature.

The regression model behaviour for the combined LHS and RHS walls is shown in figures 6.27 to 6.29. Melt temperature (SMT), injection velocity (IV) and gas delay (GD) are the processing variables present within this both regression models.

The general effect on wall thickness of changing processing parameter settings all regression models are consistent. The general effects for each of the processing parameters, as the parameter value is increased, are summarised in table 6.1.

Factor increasing in magnitude	Abrv.	Effect on wall thickness
Tool temperature	STT	Decrease
Melt temperature	SMT	Decrease
Injection velocity	IV	Decrease
Gas pressure	GP	Decrease
Gas delay time	GD	Increase

Table 6.1: The general effect on residual wall thickness of increasing the magnitude of processing variable appearing in the regression equations.

6.4.2 Material shrinkage

As the polymer melt cools and solidifies shrinkage, or an increases in density, takes place. The amount of shrinkage is difficult to quantify and is dependent upon the cooling rate of the material which affects the degree of crystallisation [75]. The measurements taken from the manufactured specimens represent the residual wall thickness after the material has gone through shrinkage. The wall thickness immediately after primary gas penetration is likely to have been greater than the measured value from the specimen.

The polymer melt represented within the simulation is an incompressible fluid that does not use a PVT model to account for density change during cooling. Therefore, the predicted wall thickness from the simulation relates to the point at which primary gas penetration has taken place. In order to compare the simulation result directly with the specimen wall thickness some consideration must be given to material shrinkage during cooling.

Data on the shrinkage of the material from the melt phase to the solid phase is not freely available from the manufacturer of the material. However, data regarding the density of the material in melt and solid states is available from

Property	Value	Source
Melt density	844.0Kg/m^3	VISDAT (Moldflow)
Solid density	950.0Kg/m^3	Manufacturer (BP Chemicals)
Solid density	952.0Kg/m^3	VISDAT (Moldflow)

Table 6.2: Values of melt and solid densities for BP HDPE 5050 EA

the Moldflow material database (VISDAT) and the manufacturer of the material. The values available for density are shown in table 6.2.

An estimate of shrinkage can be made directly from the density figures in table 6.2. Equation 6.3 estimates the material shrinkage by volume to be 11.2%, using the combination of Moldflow and manufacturer data.

$$\frac{950 - 844}{950} = 11.2\% \tag{6.3}$$

The figure of 11.2% shrinkage by volume implies a shrinkage of 3.9% in any single dimension. This can be shown by considering a cube of volume, V, and dimensions x, y and z. A shrinkage in the volume of 11.2% requires that each of the dimensions shrink by 3.9%, as shown in equation 6.4.

$$\begin{aligned} V &= xyz \\ 0.888V &= (0.961)^3 xyz \end{aligned} \tag{6.4}$$

The accuracy of the figure for shrinkage of 3.9% in any one dimension is arrived at by considering an unconstrained cube of material. In the real case the melt along the gauge length is constrained from shrinking axially by the form of

the specimen tabs at either end. More shrinkage is likely to take place in the wall thickness direction in order to compensate.

The figure of shrinkage used here is a useful estimate in the absence of any method for confirming experimentally the melt shrinkage in the wall thickness direction.

6.4.3 Relationship between simulation and experimental settings

The relationship between the process settings in a simulation and an experiment are fundamental to the capability of the simulation to accurately replicate an experimental result. Some simulation variable settings are easily transferable from the experimental conditions, such as delay time. Other settings, such as gas source rate, are not easily transferable and must be inferred from other experimental signals. The process variables investigated experimentally were mould temperature, melt temperature, injection velocity, gas pressure, gas delay time and gas trigger.

6.4.3.1 Melt temperature

The melt temperature settings are over the range 210–250 °C . For most simulations the melt temperature setting is held at 200 °C since the stability of the solution is better, possibly due to the more moderate range of viscosity across the melt. Also, the change in wall thickness up to higher melt temperatures of 250 °C does not appear to follow a trend. This can be seen in figure 6.22, which

justifies leaving the temperature at a constant setting. Clearly, the number of simulations are also kept to a reasonable number.

6.4.3.2 Mould temperature

The wall temperature is a boundary condition and is set to 30 °C in all cases. The effect of wall temperature changes on the residual wall thickness have not been investigated in this work due to practical limits on simulation time.

The wall temperature is not measured experimentally, which means the actual wall temperature during processing is not known, hence simulations with varying wall temperature could not be validated directly.

6.4.3.3 Injection velocity

As an initial starting point for the simulation the cavity is filled with polymer melt. The melt injection phase is not covered by the simulation due to solution stability problems when melt is injected into the empty cavity. Therefore, the link between melt injection rate on the machine and a melt injection rate within the simulation cannot be made.

6.4.3.4 Gas pressure

The gas pressures used in the experiments do not translate easily to the simulation. The simulation requires a gas flow rate from the source region to be specified. Therefore, bubble flow is forced by a mass increase within a region and not the direct effect of a pressure.

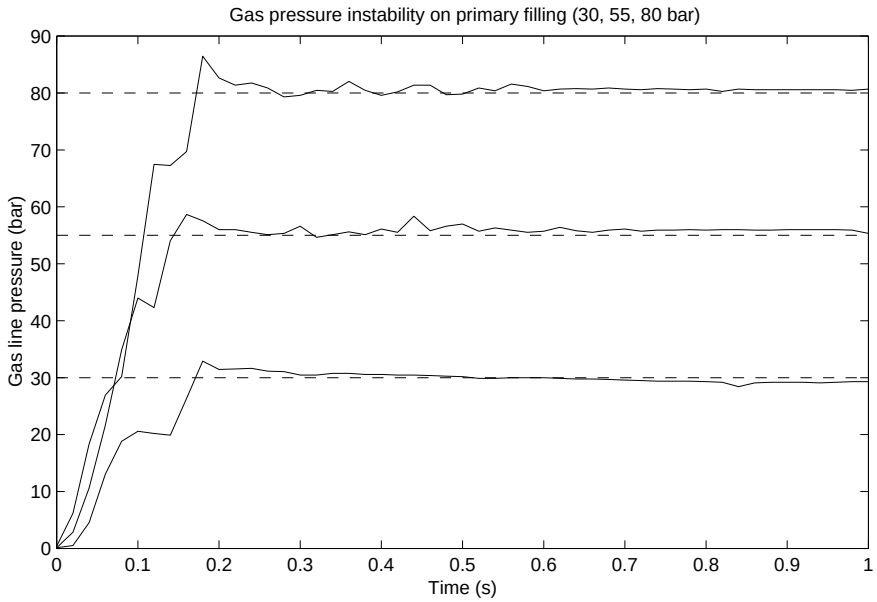

Figure 6.30: Gas pressure at the point of injection and a short time after. The instability infers gas flow into the mould. The pressure settles when the pressure in the mould is equal to the line pressure.

If the melt was made to be highly viscous the pressure in the simulation would just increase to a level that is forced by the ingress of gas from the source. Clearly, in the real system, a gas pressure that is too low may not form the bubble in the melt before the melt cools sufficiently to prevent flow all together.

So, the setting for the gas source strength needs to be inferred from other known processing phenomenon. The procedure followed to determine the gas source strength is based on estimating the time taken for the gas bubble to form in the real cavity. In order to arrive at a satisfactory estimate the gas pressure signal is utilised.

The gas pressure either side of the needle are investigated off-line using a closed volume chamber. Transducers measure chamber pressure and gas line

pressure. The equipment is described and the details of the findings presented in section 4.2.3. The findings highlighted that the gas pressure signal exhibited instability while the chamber pressure was building to the line pressure. The indication, therefore, is that instability occurs while gas is flowing through the needle.

This use of gas pressure instability to indicate flow through the needle and into the cavity has not been found within existing literature, despite a thorough search. If gas flow is continuing into the cavity either the bubble is still penetrating the melt or the bubble is fully formed, but the bubble pressure is still rising to the line pressure.

Figure 6.30 shows the gas line pressure signal during the injection of gas into manufactured specimens. Three gas pressure set points are shown in figure 6.30, which are 30, 55 and 80 bar. The time scale over which the line gas pressure settles appears to be approximately 0.6 seconds. This is worked out from the time of initial gas injection to the point at which the gas signal becomes consistent with the set value. The gas bubble may form in less than 0.6 seconds and over the remaining time the gas pressure within the bubble is building to line pressure. The exact ratio cannot be determined at present, but further work using a series of pressure or ultra sound transducers along a flow path may provide necessary data.

The approximate flow source strength is calculated on the basis that the bubble front takes 0.6 seconds to travel the length of the specimen. The length of the specimens is taken to be 200mm, since the bubble penetration into the

end tabs is not significant. The mean velocity, $\bar{u}$, of the bubble tip is therefore calculated to be 0.333m/s. If the bubble penetration causes 50-60% of the melt to flow during penetration in an isothermal system (i.e. no delay time effect) then the area of the displaced melt over the quarter model of the 15x10mm gauge section is given by,

$$A = \frac{1}{4} \times (0.015 \times 0.010) \times 55\% = 2.05 \times 10^{-5} m^2.$$

The flow rate is calculated to be approximately 7x10^{-6} m^{3}s^{-1}, from $Q = uA$. The simulation is run at other flow rates to investigate the effect on wall thickness, the results are presented later.

6.4.3.5 Gas delay time

The gas delay time is easy to transfer from the experiment to the simulation. The time between the gas trigger and the start of gas injection is entered directly into the model fill control file.

6.4.3.6 Gas trigger

The gas trigger signal that originates from the injection moulding machine controller, when the screw reaches a set position, is covered by the simulation software. The trigger essentially signals the end of melt injection into the mould. The simulation is not used to model the injection of melt before gas for reasons outlined earlier under injection velocity.

Gas delay time (sec)	Gas flow rate (x10^{-6} m^3s^{-1})			
	7	15	25	35
0.05				
0.10				
0.20				
0.50				
1.00				
2.00				
5.00				
10.00				

Table 6.3: Each gas flow rate is tested at each of the gas delay times

6.4.4 Simulated wall thickness

Delay time and gas flow rate are key simulation variables tested to predict their effects upon residual wall thickness. The effect of the delay time is investigated by varying the time between the start of the simulation and the start of gas injection.

6.4.4.1 Simulation setup

A series of simulations are completed under an array of gas flow rate and delay time conditions. The conditions are listed in table 6.3, resulting in 32 separate simulation runs.

Figure 6.31 shows the wall thickness prediction for the FIXED and MOVING wall, which is the short dimension on the gauge length cross section. The series of flow rates over the range of delay times are shown. As previously mentioned, the flow instability (possibly due to thermal gradients giving a rapid variation in viscosity) that causes a waviness in the concentration contour is affecting the

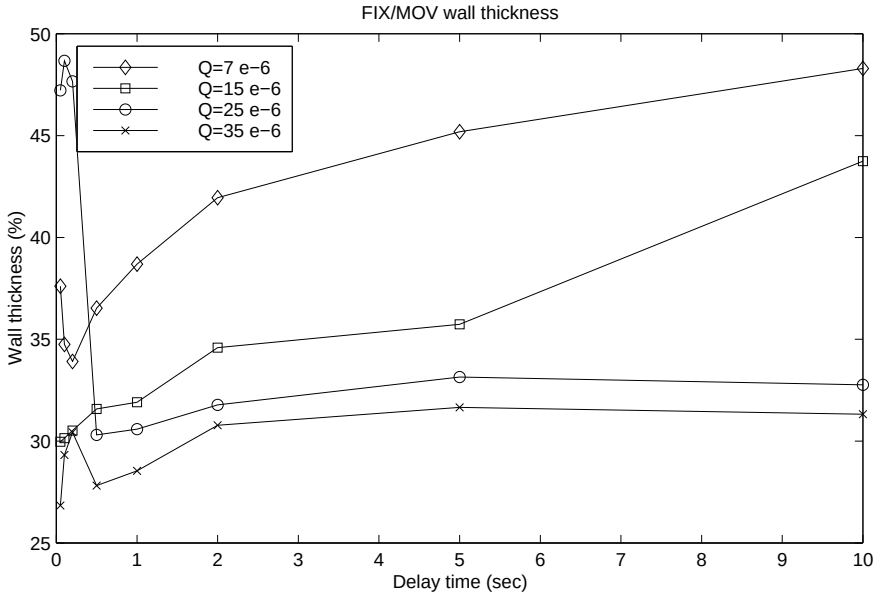

Figure 6.31: Simulated wall thickness over the range of flow rates and delay times in table 6.3.

wall prediction at low delay time and high flow rate. Lower time steps have been tested, but the instability is still present. The solution is almost certainly using more elements in the short section dimension that comprises the FIXED-MOVING wall, probably combined with smaller time step. The higher mesh density is not possible at present due to a limitation in the mesh bandwidth.

The wall thickness prediction over the delay time range of 0.05 to 0.2 sec at a flow rate of $25\text{x}10^{-6}\text{m}^3\text{s}^{-1}$ is in excess of 46%. The induced flow stability from the greater delay time brings the prediction back to around 30%.

In order to improve the simulation prediction the wall thickness is taken at nodes positioned between the high points, noted previously in figure 6.3. The resulting plot of wall thickness over the simulation conditions is shown in figure 6.32a, which is thought to be more accurate.

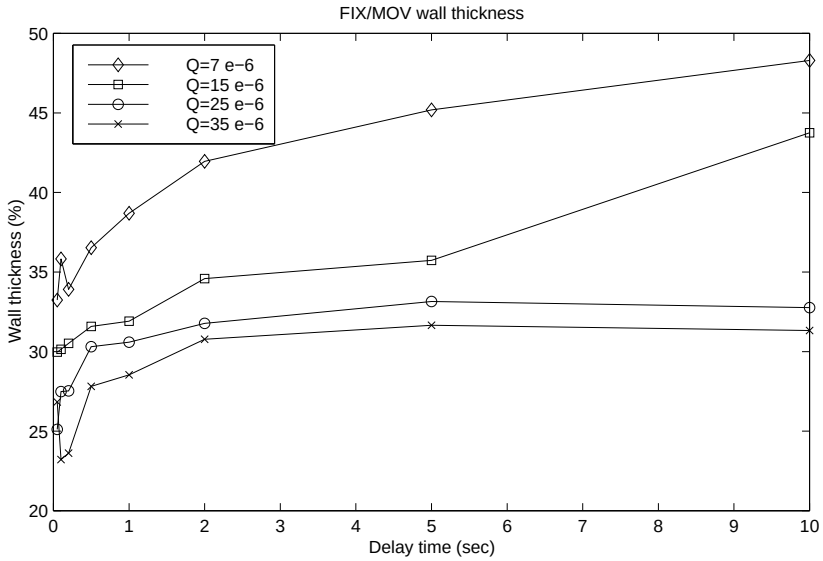

(a) Simulated fixed and moving wall thickness

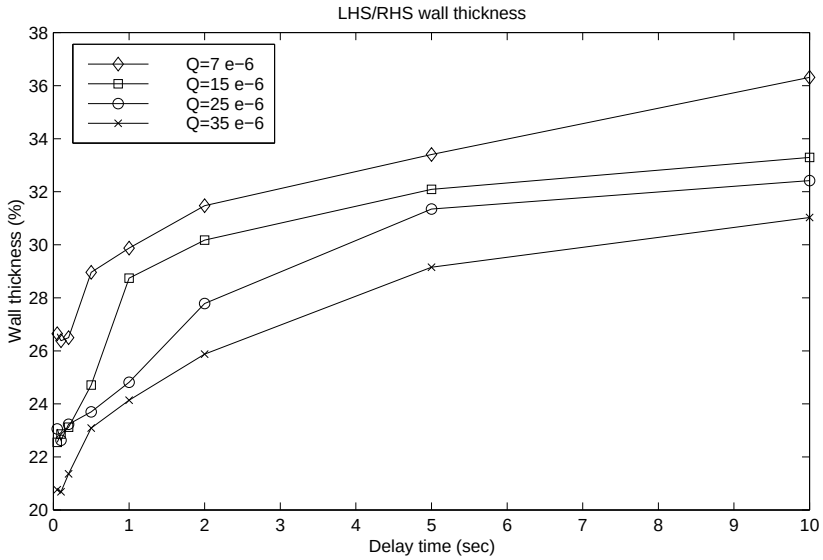

(b) Simulated LHS and RHS wall thickness

Figure 6.32: Simulated wall thickness for a range of different gas source magnitudes over a range of gas delay times. Mesh effects on the wall thickness are allowed for and improve the consistency of the prediction at low delay times.

Figures 6.32a and b present the LHS-RHS and FIXED-MOVING wall thickness prediction results, respectively, for the conditions set out in table 6.3. The predicted wall thickness is presented as a percentage of the centreline dimension. So for the LHS-RHS wall, the residual wall thickness is translated to a percentage of the large dimension of 7.5mm. Similarly, the FIXED-MOVING wall is translated to a percentage of the small dimension of 5.0mm.

6.4.4.2 Trends in the results

The wall thickness tends to decrease as the gas source flow rate increases in strength. The same trend is observed in the experimental model of the FIXED and MOVING wall, where an increase in the gas pressure causes a decrease in the residual wall thickness.

An increase in gas delay time causes an increase in residual wall thickness and the trend appears to approximate to a logarithmic function. The highest gradient of wall thickness change with gas delay time occurs at the lowest delay time settings, approximately below 1.0 seconds.

Again, the gas delay time trend of wall thickness from the simulation result is in agreement with the experimentally obtained trend. The quadratic effect of gas delay time on wall thickness is also observed in the experimentally obtained model.

6.4.5 Simulated and experimental wall comparison

The experimental results used for comparison with simulation are derived from the regression equations developed in chapter 4. Experimental wall thickness on the LHS-RHS (long dimension on cross section) is derived from the average LHS-RHS regression equation, which is equation 4.5. Similarly, the FIXED-MOVING wall thickness (short dimension on cross section) is derived from the average FIXED-MOVING regression equation, which is equation 4.6.

The active process variables present in the respective regression equations are listed in table 6.4. For clarity, the factor abbreviations are set melt temperature (SMT), injection velocity (IV), gas pressure (GP) and gas delay time (GD).

Wall equation	Active factors
LHS-RHS	SMT, IV, GD
FIXED-MOVING	STT, IV, GP, GD

Table 6.4: Active factors in experimental models of wall thickness

The minimum and maximum wall thicknesses for both the LHS-RHS and FIX-MOV experimental models can be calculated by setting the factors to appropriate levels. The effects plots are useful for indicating how each factor effects the wall thickness and which settings to use.

6.4.5.1 General section formation

The general cross sectional form observed within the experimentally produced specimens show a collection of polymer in the corners of the cavity. The bubble formation is slightly elliptical. Figure 6.33 shows a qualitative comparison between the simulation result and the experimentally obtained section. The general

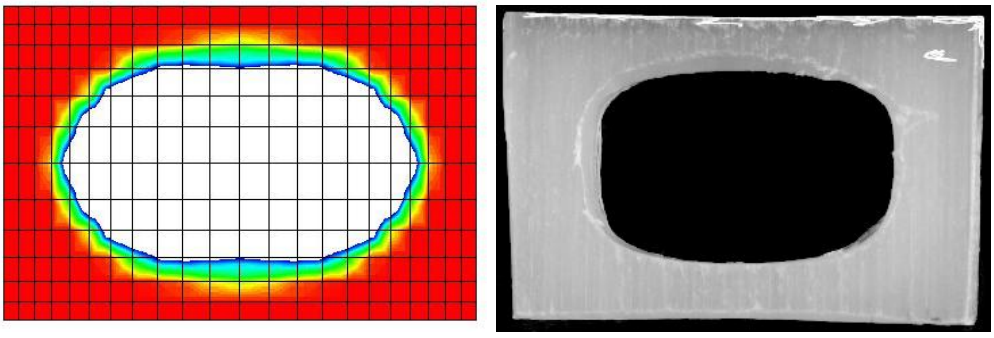

(a) Simulated section (b) Actual section

Figure 6.33: The general cross section form of the gas bubble observed experimentally is reflected with simulation results

form of the gas bubble is in good agreement. The collection of melt is evident in the corner and the wall thickness along the axes of symmetry is the thinnest point.

6.4.5.2 Thickest and thinnest residual wall

	Setting			
LHS-RHS wall	SMT	IV	GD	Wall (%)
Thinnest	250	80	0	31.9
Thickest	210	20	10	43.3

Table 6.5: Factor settings for the LHS-RHS empirical models that give thickest and thinest residual wall

	Setting				
FIXED-MOVING wall	STT	IV	GP	GD	Wall (%)
Thinnest	60	80	80	0	29.4
Thickest	30	20	30	10	45.2

Table 6.6: Factor settings for the FIXED-MOVING empirical models that give thickest and thinest residual wall

Parameter	Value	
Gas source flow rate	7, 15, 25, 35x10^{-6}	m^3s^{-1}
Melt temperature	200	°C
Wall temperature	30	°C
Delay time	$0 - 10$	sec

Table 6.7: Simulation conditions

The overall range of the empirical residual wall thickness models can be determined. The factor settings for each of the LHS-RHS and FIXED-MOVING empirical models are listed in tables 6.5 and 6.6 respectively. The range of the LHS-RHS residual wall formation is 31.9% to 43.3% (11.4% difference) and the range of the FIXED-MOVING wall formation is 29.4% to 45.2% (15.8% difference).

The range of residual wall thickness results from the FIXED-MOVING and LHS-RHS models are plotted over the gas delay time range in figures 6.34a and 6.34b respectively. The simulated wall thickness over the respective gas delay time range is over layed in each of the figures 6.34a and b. The conditions under which the simulations were run are detailed in table 6.7.

With reference to figure 6.34 the the logarithmic form of the simulated wall formation is apparent. The rate of change of wall thickness with delay time for the simulation results is greater at the shorter gas delay values than at the longer delay times, above 2.0 sec. The wall thickness result from the empirical model does not show a sharp increase in wall thickness over delay time at the lower delay times. The second order nature of the empirical model for describing wall thickness change with delay time is fitted to three delay time values equally spaced over 0–10 sec. Further specific experiments are needed to give better resolution

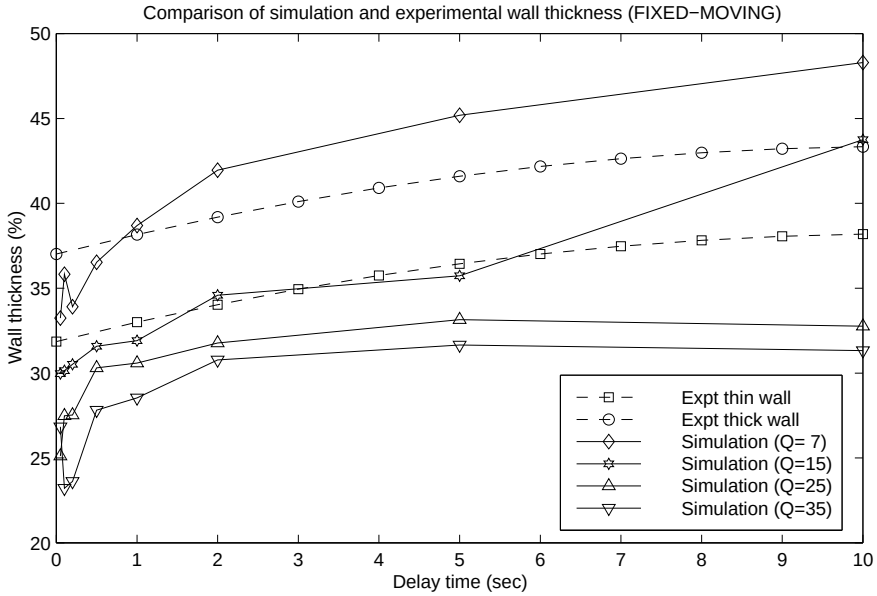

(a) FIXED and MOVING comparison

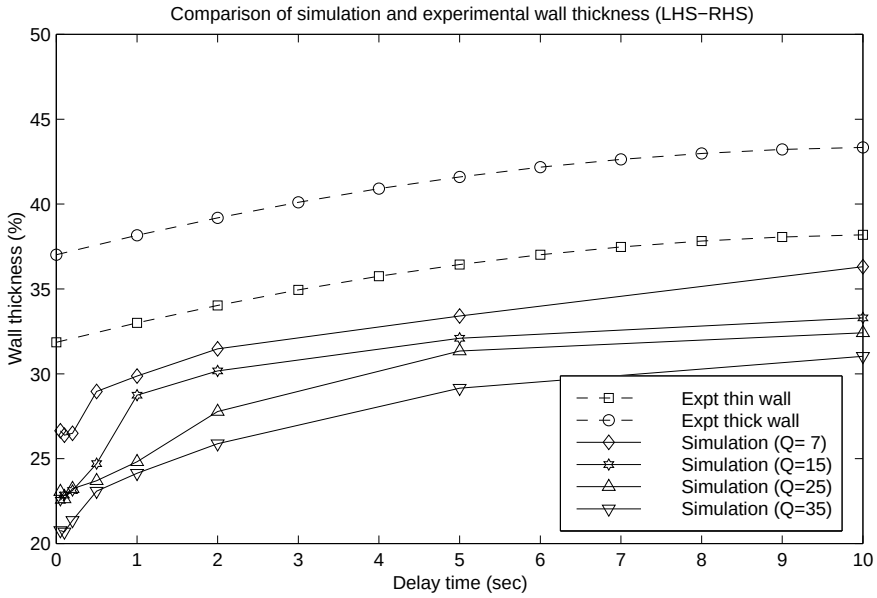

(b) LHS and RHS comparison

Figure 6.34: The thickest and thinest experimental residual wall is compared with the simulation over the gas source flow rate range of $7 - 35\text{x}10^{-6}\text{m}^3\text{s}^{-1}$.

over the shorter gas delay times.

The wall thickness range plots shown in figure 6.34 indicates a difference in matching experimental to simulation result between the LHS-RHS and FIXED-MOVING walls. The simulation results for the FIXED-MOVING wall over the gas flow rate range of $7 - 35\text{x}10^{-6}\text{m}^3\text{s}^{-1}$ coincides with the maximum range of experimentally obtained wall thickness results (fig 6.34a). The lowest gas flow rate of $7\text{x}10^{-6}\text{m}^3\text{s}^{-1}$ provides a wall thickness prediction that is greater than the thickest experimentally obtained wall at delay times greater than 1.0 sec. All other simulation results are either within or below the experimentally obtained wall thickness range.

The set of simulation results for the LHS-RHS wall over all gas flow rates are below the experimental wall thickness range. The tendency for the LHS-RHS simulation result to consistently under predict the experimentally obtained wall thickness is not reflected in the FIXED-MOVING results. Only the higher flow rate simulation results from the FIXED-MOVING wall will under predict the experimentally obtained results.

6.4.5.3 Comparison based on closest variable conditions

A direct comparison for wall thickness prediction from the simulation can be made with the experimental model based upon factor settings. The wall thickness comparison for the case where factor settings are closely matched between experiment and simulation is presented in figure 6.35.

In figure 6.35a two experimental predictions are shown, one each of 30 and

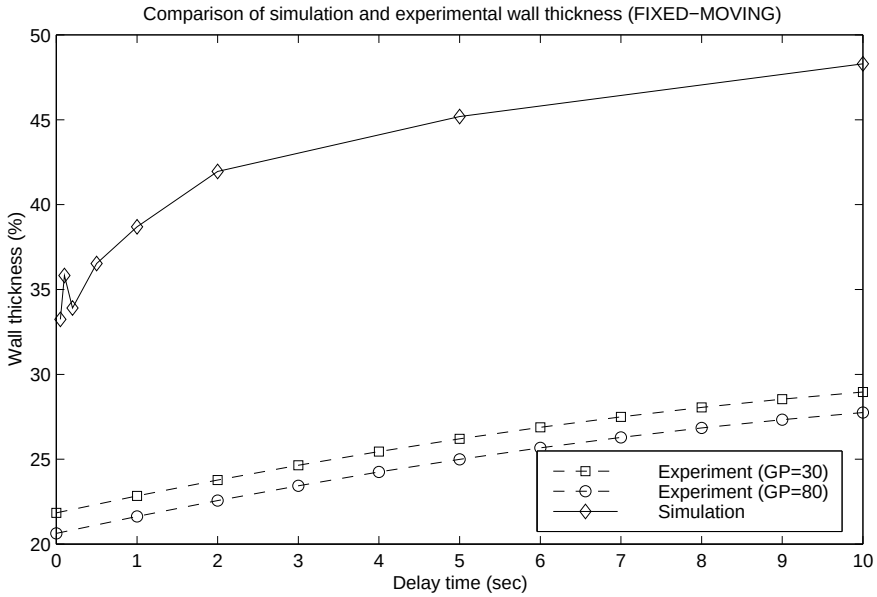

(a) FIXED and MOVING comparison

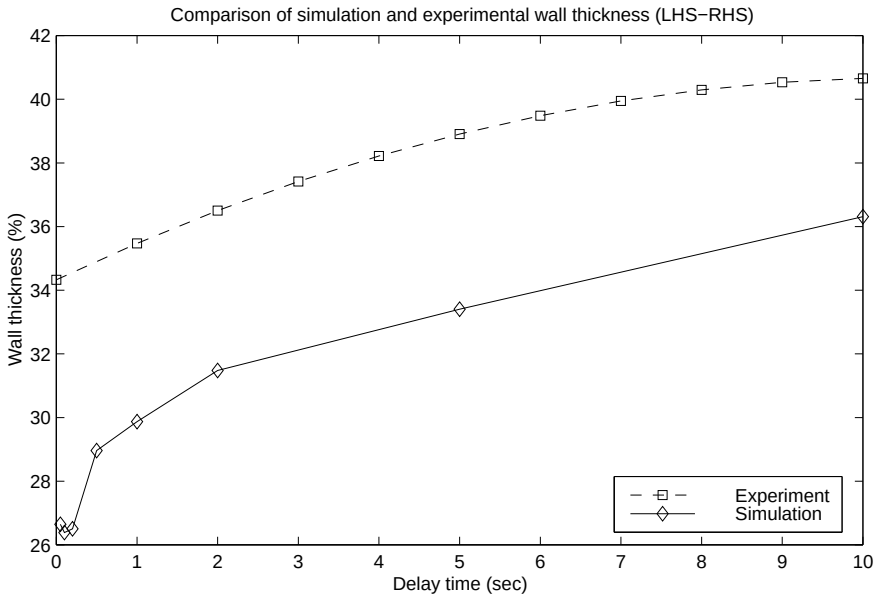

(b) LHS and RHS comparison

Figure 6.35: Simulation and experimental settings are most closely matched

60 bar gas pressure entered into the regression equation. This is useful because the relationship is not clear between gas pressure in the experiment and the gas source flow strength in the model. The gas pressure factor is not in the LHS-RHS regression model, so figure 6.35b only contains one line for experimental prediction.

The factor settings for the experimental wall thickness results in figure 6.35 are listed in table 6.8.

	Setting				
	STT	SMT	IV	GP	GD
FIXED-MOVING	30	–	80	30, 80	0–10
LHS-RHS	–	210	80	–	0–10

Table 6.8: Factor settings in the experimental models for direct comparison with simulation results.

The simulated FIXED-MOVING wall thickness prediction could be forced to match the experimental value more closely by increasing the gas source flow rate. The wall thickness prediction would therefore reduce. However, increasing the gas source flow rate would move the simulated LHS-RHS wall thickness further away from the experimentally obtained wall thickness value.

6.4.5.4 Considering melt shrinkage during cooling

Melt shrinkage during cooling is taken into account. The value for shrinkage was obtained from material data, which is outlined in more detail within section 6.4.2 and is taken to be 3.9%. The wall thickness prediction from the simulation is relevant to the time immediately after gas injection in the real process, before appreciable cooling has taken place. The wall thickness prediction results from the

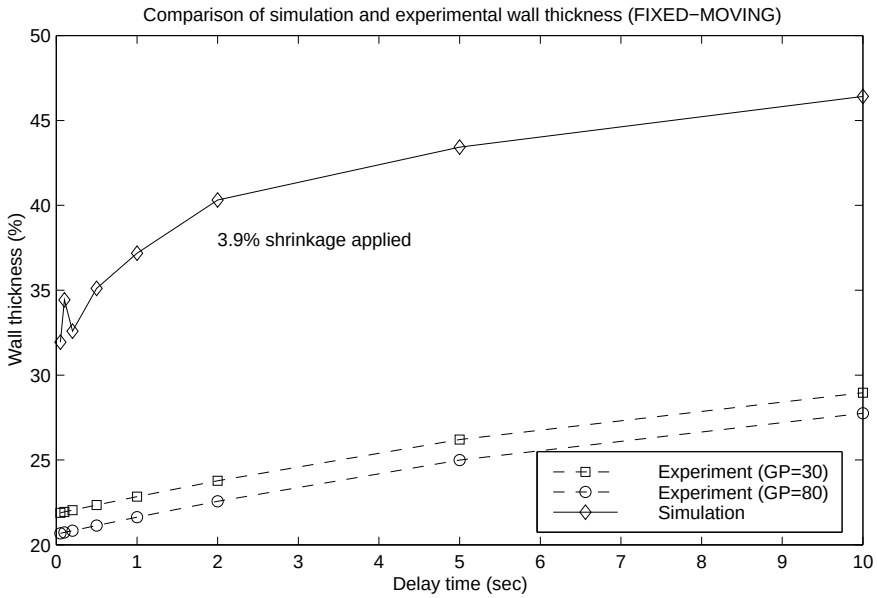

(a) FIXED and MOVING comparison

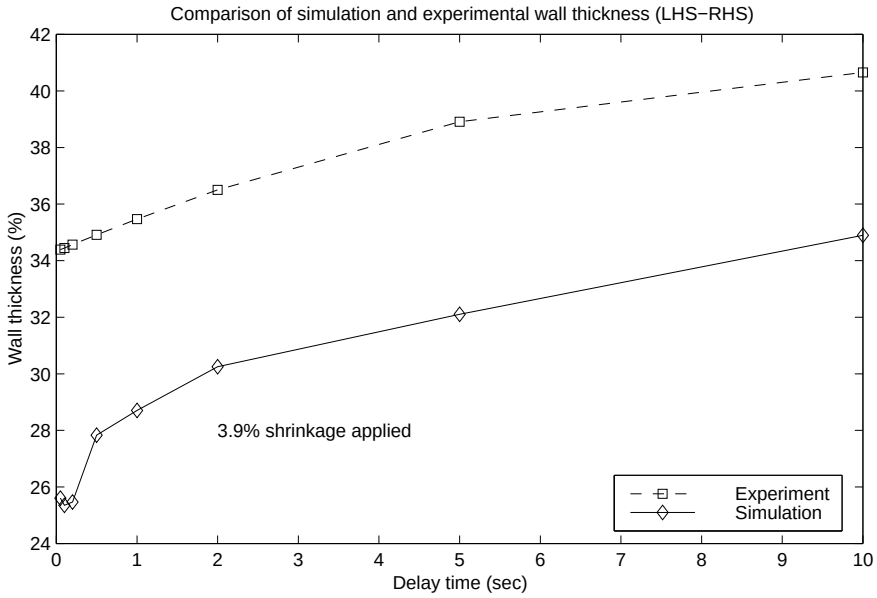

(b) LHS and RHS comparison

Figure 6.36: Simulation and experimental settings are more closely matched and material shrinkage during cooling is accounted for.

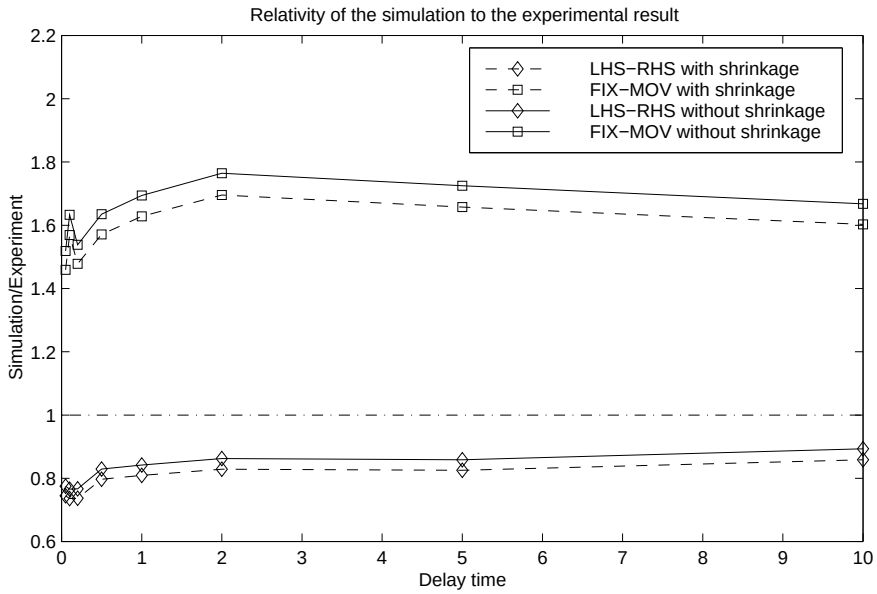

Figure 6.37: The relative error between simulation and experiment

simulation shown in figure 6.35 are re-presented with an 3.9% material shrinkage factor applied in figure 6.36.

The shrinkage factor improves the simulation comparison with the experimental data for the FIXED-MOVING wall case since the simulation over-predicted the actual wall thickness observed experimentally. However, the shrinkage factor worsens the simulation comparison with experiment in the LHS-RHS case since the simulation under-predicts wall thickness.

6.4.5.5 Simulation accuracy

A measure of the accuracy of the simulation relative to the experimental result can be quantified by dividing the simulation result by the respective experimental result. The relative accuracy is calculated over the delay time range for both the LHS-RHS and FIXED-MOVING walls and presented in figure 6.37. An exact

match in wall thickness would provide a relative value of 1.0.

The dotted lines show the simulation accuracy with shrinkage applied to the wall thickness result. The solid lines show the simulation accuracy without any modification to the result for shrinkage.

Before shrinkage is applied the LHS-RHS simulation result is closer to the experimental result. At low delay times and before shrinkage the simulation predicts approximately 80% of the experimentally obtained wall thickness and improves to 90% at a delay time of 10.0 sec.

Since the FIXED-MOVING wall simulation result is an over prediction of the experimental wall the application of shrinkage improves the accuracy. The most accurate prediction is at 0.0 sec delay time with shrinkage applied, which provides an over-prediction of 46%.

The exact shrinkage in the material during cooling experienced experimentally is not an easy quantity to measure. Therefore some flexibility in the applied shrinkage factor must be assumed, which effects the simulation accuracy. Since the gauge length is constrained axially, while inside the mould, by the end tabs the shrinkage axially is constrained. Therefore to attain the volumetric shrinkage outlined earlier (section 6.4.2) the shrinkage within the cross sectional plane may need to increase to compensate.

6.5 Summary

The implementation of the two phase flow theory into a 3D finite element model is applied, with some success, to the problem of forcing a gas bubble to penetrate

polymer melt inside a cavity form. One of the key features of gas assisted injection moulded products is the residual wall thickness formed by the passing bubble front.

The finite element implementation is governed by a number of constraints. Mesh density is restricted, particularly in the short dimension of the cross-section, that relates to the FIXED-MOVING wall. This is believed to cause flow instability and effect the accuracy of the wall thickness prediction at high gas source flow rates. The computer restrictions and solution time also limits the size of the model to half of the specimen length. Flow and geometry symmetry is utilised to further reduce the computational demand.

Restrictions prevent modelling of pre-filling of the cavity with melt. This feature is important if the extent of bubble penetration into a fully meshed cavity is desirable. A procedure to simulate air venting from the mould is needed for the pre-filling stage to be modelled more accurately. In place of venting from the cavity the flow is allowed to exit the mesh at the end of the flow path. Therefore, the gas bubble can penetrate the melt un-hindered, other than by the expected viscous stresses.

The shrinkage of the melt during cooling is dealt with, after simulation, in the form of a simple shrinkage factor. Data for the shrinkage factor is obtained from material databases and manufacturers data in the form of a density change from melt to solid. The shrinkage in a single dimension of an unconstrained cube is estimated to be 3.9%

The compromises on the modelling implementation are not thought to impinge

too greatly on the formation of the bubble and the wall thickness prediction. The agreement between the simulation and the experimentally obtained values is at best within 10%. However, the general trends observed in wall thickness caused by changes in processing parameter changes are reflected in the simulation.

Chapter 7

Discussion

The discussion of the experimental and numerical investigations of the gas assisted injection moulding process aims to summerise and comment on the important issues highlighted within this thesis. The issues are split into those that relate to experiment, those that relate to simulation and those that tie into both areas.

The major focus of this thesis is on the accurate prediction of the residual wall thickness. An FE implementation, based upon a pseudo-concentration method, is used to simulate the gas bubble formation through the melt and provide an insight into the process physics.

Firstly, some global issues are discussed that relate to mesh geometry and the extension of the simulation to more complex geometries. Later, specific issues are presented that are pertinent to experimentation, simulation and validation.

Within this thesis a FE mesh has been used that describes half the test specimen length for simulating gas bubble penetration through the melt. Flow and geometry symmetry along the specimen length are utilised to reduce computa-

tional requirements by the application of suitable boundary conditions. The mesh extends to a position that is equivalent to half way along the gauge length.

The half specimen length model is used instead of a full length model because it provides a number of advantages over the full model:-

1. the memory requirement and CPU time are much lower (<50%) for an equivalent mesh density,
2. the mesh density can therefore be increased,
3. wall thickness predictions are equivalent to those from a full model (better with higher mesh density),
4. results are normally available within two days.

The half specimen model does not have the scope to provide an estimation of gas bubble penetration into the melt. The mesh would have to be extended to the full geometry of the specimen. However, currently the simulation would not provide a meaningful estimate of bubble penetration for the following reasons:-

1. the form of the residual wall is not sufficiently accurate with the current mesh densities and thermal boundary conditions,
2. the melt flow boundary condition is not cancelled at a point when gas injection begins,
3. the solution stability is poor when melt is injected into an empty cavity.

The GAIM process is applied to other geometries, typically ribbed plaque products that connect a flat surface to a thick sectioned rib for the gas bubble

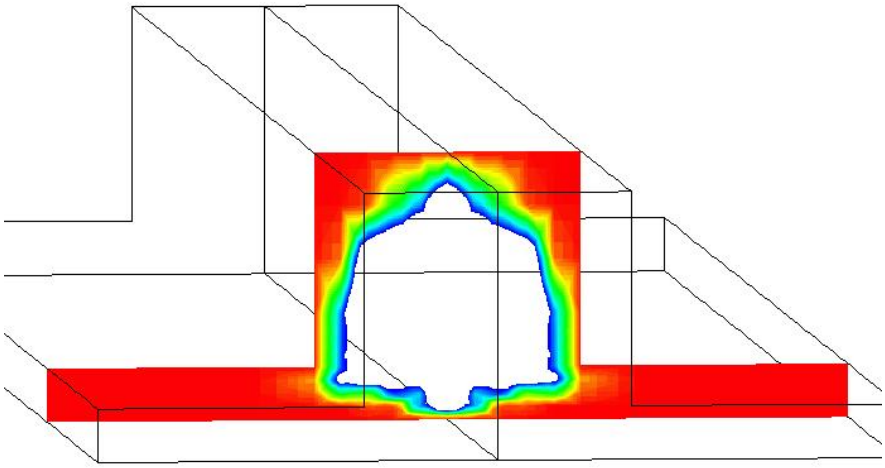

Figure 7.1: Gas bubble formation within a ribbed plaque structure

to penetrate. The main issue with this type of geometry is the uncontrolled penetration of gas from the channel to the flat section. Limited simulation has been done on the ribbed plaque geometry because the validation capability lies with the tensile test specimen. A result from a ribbed plaque geometry is shown in figure 7.1 and shows the gas bubble penetration mainly contained within the channel. Studies of the ratio between the channel and flat section thickness could be investigated in further work.

The thickness of the residual wall is influenced by processing factors such as gas delay time, melt injection velocity, melt and tool temperature and the gas pressure used to form the bubble during primary gas penetration. The correlations between key processing variables and the trend in wall thickness are common between the simulation and the experiment. This is encouraging since it indicates that key process physics are correctly described within the model.

7.1 Experimental issues

7.1.1 Choice of material

The BP grade of HDPE used within this thesis was primarily chosen because it is a well characterised material and studied by many other colleagues in the laboratory. The material is also in abundance in the laboratory, which is important when running an industrial scale machine. Particularly as the cycle needs to run uninterrupted for some hours, before experiments are conducted, to allow the process to settle.

The manufacturers data sheets describe the applications for the material as technical mouldings, bins, crates, boxes and household items [58]. These items are likely to use gas to form strengthening channels, particularly the crates and bins.

Time was not available to repeat experiments on specimens manufactured in other materials.

7.1.2 Temperature measurement

During the manufacture of GAIM specimens no provision is made for melt temperature measurement, either within the mould or machine barrel. The machine barrel can be fitted with a rheometric nozzle equipped with ports that house melt temperature sensors. However, a specially designed gas nozzle must be fitted in place of a rheometric nozzle to prevent gas from entering the machine barrel. New nozzles, specifically designed, are required to fulfil both requirements allow-

ing existing melt measurement techniques to be used, such as thermocouples and fast response infra-red devices.

Temperature sensors fitted into the mould would indicate more accurately the mould wall temperature and possibly reveal the extent of changes in the wall temperature during melt delivery, gas injection and the cooling phase. The existing mould does not lend itself to modification since the steel is now case hardened, which requires special forming techniques like Spark-Erosion.

7.1.3 Material shrinkage

The change in shape of the melt as it cools inside the mould is not known. Estimates can be made based on data from manufacturers and materials databases, but the estimates are difficult to confirm. An estimate of 3.9% has been obtained. The shrinkage of the material is dependent upon the cooling rate and Moller [52] has demonstrated this with experiments on specimens cooled at different rates after ejection from the mould.

The residual wall thickness measured from the specimens is unlikely to be the same as the wall thickness formed immediately after bubble penetration. The polymer is molten immediately after bubble formation, but when measured from the specimen, at least 24 hours later, the polymer is solid. The simulation provides a wall thickness prediction for the time immediately after bubble formation. A shrinkage factor can be later applied to the simulation result.

In order to measure wall thickness before shrinkage, which is the time immediately after bubble penetration, an ultra sound based technique could be used.

An ultrasonic probe placed at the mould wall will provide a signal indicating a reflection from the gas/melt interface. The signal can be calibrated to estimate the melt thickness through which the signal has travelled and therefore provide a measure of wall thickness.

Measures of shrinkage on the external surface of specimens, such as the distance between ejector pin impressions, are not likely to be representative of the shrinkage experienced by the residual wall. The pressure of the gas bubble allows the specimen to shrink from the inside and maintains an external profile that is faithful to the cavity shape.

7.1.4 Gas delay time

The gas delay time has proved to be an influential process variable for controlling the residual wall thickness. The prevention of uncontrolled gas penetration from gas channels into thin sections, often called "fingering", can be achieved with a delay time. However, when related to the production of real mouldings that are subject to a customer specification, the gas delay time can effect aesthetical properties in the form of external "hesitation marks" and add time to the processing cycle.

Hesitation marks are caused by the melt flow front becoming stationary during the gas delay time. The hesitation mark is located on the outside surface of the specimen at the point on the geometry where the melt flow front became stationary. Clearly, the processing window for gas assist is subject to restrictions that may conflict with desirable product features, such as no visual defects.

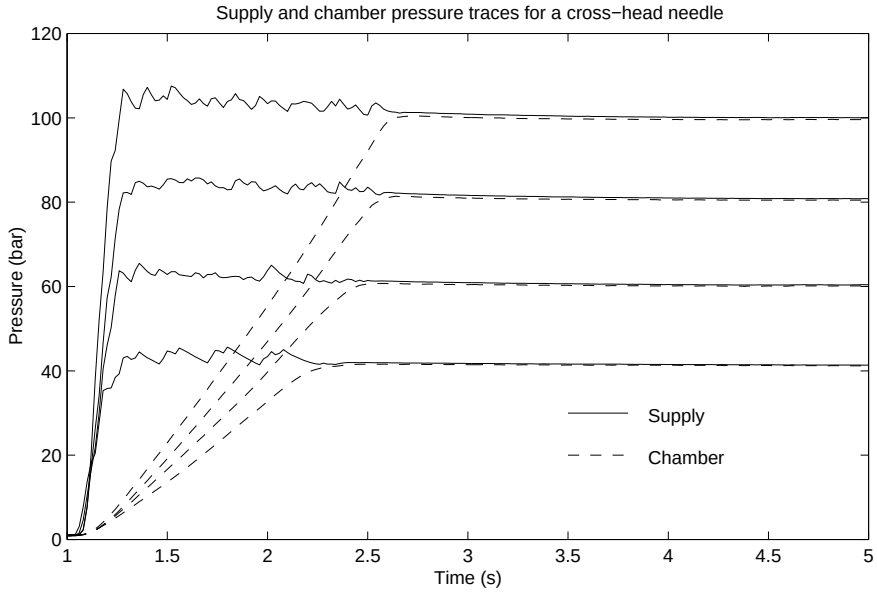

Figure 7.2: Line pressure and chamber pressure development over time for line set pressures of 40, 60, 80 and 100 bar. (Repeat of figure 4.7)

7.1.5 Gas injection needle

Gas pressure development inside the cavity can only be estimated with the help of off-line tests (section 4.2.3) on the gas injection needle. A fixed volume gas chamber fitted with pressure transducers before and after the needle monitors the difference in pressure across the needle. The volume of the gas chamber is around 1.4 times the volume of the entire tensile test cavity.

A pressure trace showing the rise in chamber pressure with respect to the supply pressure is shown in figure 7.2, which is figure 4.7 repeated. The pressure trace relates to the standard needle and clearly shows a time lag of around 1.5 seconds in the chamber pressure behind the line pressure. The pressure lag raises the possibility that the gas bubble may penetrate the melt and initially form under a pressure that is lower than the line pressure setting. The sensitivity

of wall thickness to the gas pressure setting may well be reduced as a result.

A needle with a larger opening for the gas is not feasible since melt will push into the needle, before gas injection takes place and cause a blockage. In fact, the pressure in the chamber is found to follow the line pressure almost exactly if the central gas pin is removed and is shown in figure 4.7a. The removal of the central gas pin during processing is clearly not feasible.

Attempts have been made to measure the melt pressure at the mould wall using a piezoelectric pressure transducer. However, faults developed with the charge amplifier and time restrictions led to no clear results being obtained. The piezoelectric transducer does not provide a steady pressure reading over time since the charge providing the signal decays. The transducers are typically used in conventional injection moulding to measure the changing pressure during melt injection which is used to switch over from velocity control for mould filling to pressure control for packing.

7.2 Issues relating to simulation

7.2.1 Computational requirements

The accuracy or acceptability of a numerical solution is often compromised by the computational requirements of the solution. The 3D implementation of the simulation is computationally intense and has forced some simplifications in the modelling approach in order to obtain a solution.

Methods to reduce the number of elements required by a simulation are wel-

come. The symmetry of the geometry and flow along the length of the tensile test specimen is exploited to form a quarter section model. A further saving in the number of elements necessary to describe the geometry is gained by modelling only half of the specimen length.

Modelling up to the half way point along the actual tensile specimens is not believed to effect the formation of the gas bubble. Full models are available and wall thickness comparison are made with prediction from the half model. The comparison indicates that wall thickness prediction and bubble formation over the cross section is not significantly different. Indeed, experimental observation notes that the variation of wall thickness along the gauge length is less than $\pm 0.03mm$ (fig 4.10). There is a significant saving in solution time of at least 50% along with higher mesh density associated with the specimen length model over the full length model. Experimental results show a uniform wall thickness along the gauge length and indicate a representative wall thickness measurement can be taken anywhere within the middle 50% of gauge length.

The solution time is determined by the number of elements within the model. Accuracy is generally improved as the mesh density increases, however, to avoid the concentration gradient from crossing elements within one iteration the time step must be reduced by a corresponding fraction. The number of iterations required to model the bubble flow along the specimen is a function of the flow velocity and the time step of each iteration.

The 3D simulation is initially filled with melt and gas injection starts after the specified delay time has passed. Therefore, since no requirement exists to

solve the flow of melt prior to gas injection a significant time saving is made. The time step used during the gas delay is larger than that used for solving the flow equations during gas injection. This is because the temperature changes over time are slower than the change in flow conditions.

7.2.2 Wall temperature boundary condition

The temperature at the boundary representing the mould wall does not change throughout the simulation. In most cases the wall temperature is fixed at 30°C . The temperature at the melt/cavity interface almost certainly changes in the real system as heat is conducted away from the polymer melt.

Additional elements could be defined beyond the wall boundary with a fixed temperature boundary condition set at the extreme nodes. This would provide a degree of freedom at the wall nodes for temperature and may show a more realistic wall temperature profile. The added complexity for this approach comes from the difference in coefficient of heat conduction between the steel of the cavity and the polymer melt.

This approach also has implications for computational resource since more elements would be required, particularly at the interface where the temperature gradient in the steel would be significantly higher than in the polymer. The element count and bandwidth would be increased significantly therfore demanding more memory and solution time.

7.2.3 Extent of bubble penetration

An issue that is important in the GAIM process and links closely to product quality is the distance over which the bubble penetrates into the melt. This phenomenon has not been addressed within this thesis.

Fundamental to an accurate prediction of bubble penetration is an accurate prediction of the quantity of melt pre-filling the cavity before gas injection begins and an accurate prediction of bubble formation. For example, if the wall is made thinner the quantity of melt pushed ahead of the bubble increases and the bubble penetration along the channel is reduced. This indicates, and is observed experimentally, that the quantity of melt pre-filling the cavity before gas injection influences bubble penetration.

Currently aspects of the implementation restrict the capability to achieve a bubble penetration prediction; the stability of the model is poor during the injection of melt into the empty (gas filled) mesh. Venting from nodes at the end of flow needs to be implemented, allowing gas to exit and polymer to remain. Finally, control of the boundary conditions that control melt injection must be changed to replicate the cessation of melt injection before gas injection.

7.2.4 Secondary penetration

After the initial bubble formation, termed primary penetration, the melt cools and shrinks allowing the bubble to further penetrate. The penetration of the bubble during the cooling time is termed secondary penetration and requires an extension to the current model. Work published by Chen et. al. [35, 41] has

suggested an isotropic melt shrinkage model to handle the increase in polymer density during cooling.

Secondary penetration can be very significant is some geometries, particularly were the flow length to section ratio is very high. However, the position of the bubble front after primary injection must be accurate before the extent of secondary penetration can be predicted with any certainty.

7.3 Issues that relate to validation

Correlations are observed to exist experimentally between process settings and residual wall thickness. For example, an increase in gas delay time will increase the residual wall thickness. There is good agreement qualitatively between simulation results and experimental observations. The issues influencing the accuracy of the wall thickness prediction when compared with experimentally obtained data will be discussed here.

A strength of the 3D implementation over typical commercial software is that the true bubble geometry is predicted. Commercial software uses the Hele-shaw approximation to reduce the computation time necessary to run solutions. This is a valid reason, particularly since the majority of conventional mouldings are thin walled and computation time is under pressure in industry.

7.3.1 Simulation and process variable settings

There are a number of issues arising from the correlation between process settings and configuration of the simulation. Factors readily transferable are mould and

melt temperatures along with gas delay time. These factors do not require any interpretation to be of use.

The gas pressure used to form the bubble is not readily transferable to the model since flow is induced from a source region with an assigned flow rate. The flow rate setting can only be inferred from experimental observations. For instance, instability in the gas pressure signal indicates that the pressure inside the cavity is not at line pressure. The time over which this instability occurs gives an estimate of the time taken for the bubble to form. The gas source flow rate is adjusted to provide a filling time within a similar time frame. The time frame is estimated to be 0.3 sec to fill half of the specimen gauge length and the respective flow source strength came to approximately $7\text{x}10^{-6}\text{m}^3\text{s}^{-1}$.

Flow metering of the gas as it is injected into the cavity is not practical to obtain data for the model. The response time of a flow meter to accurately track the gas at high pressures is in excess of their capabilities. The flow meters commonly supplied off the shelf would only respond to changes in flow over a few seconds and are better suited to steady state flows.

7.3.2 Comparison of wall thickness

The wall thickness measured from the manufactured sample is compared with the predicted wall thickness obtained from the simulation. The simulated wall thickness is generated purely from the action of the gas bubble passing through the melt. No further mechanisms influence the wall once the gas bubble front has passed. In particular no shrinkage of the polymer takes place that would

normally be expected to occur during cooling. The wall measurements made on the manufactured specimens are taken at least 24 hours after ejection from the mould after shrinkage has taken place.

Wall thickness comparison between real specimens and the simulation can be made directly and some error is expected since shrinkage during cooling is not accounted for. A shrinkage factor is applied to the simulation result to compare the wall thicknesses on an equal basis.

In order to obtain a consistent wall thickness measurement from the manufactured specimens an image analysis procedure is utilised on scanned cross sections. An alternative method to obtain a measurement of wall thickness is to use a vernier calliper, but this is subject to human error to a greater extent than simply scanning cross sections. The scanned image provides an permanent record of the section that could be used in future for other purposes, such as bubble form comparisons. The position within the cross section from which simulated wall thickness is taken is always consistent since the node positions are fixed.

7.3.3 The skin layer against the mould wall

A solid layer of polymer is expected to form against the mould wall due to the cooling effect of the wall. This can be observed by cutting a specimen that has not been "gassed" and is of solid section. A solid layer forms the section profile and melt is present in the centre of the section.

Clearly, the gas bubble may penetrate the molten material, but probably will

not move the solid material at the mould wall. The residual wall is formed on top of the solid polymer layer that gets thicker over time, in particular delay time. The simulation does not account for solid material at the wall to prevent movement. In effect the non-slip condition would apply to nodes within the polymer if a no-flow temperature were reached.

The anticipated result would be to provide a thicker wall prediction than is currently obtained, particularly at extended delay times. The effect on experimental comparison would be to move the LHS-RHS wall prediction higher and further away from the experimental measurement, but the FIXED-MOVING wall prediction would move closer to the experimentally obtained figure.

7.3.4 Moving the validation through time

The structure of experimental validation of the simulation result could be improved if the formation of the gas bubble can be observed. Flow visualisation may be possible through a transparent mould [40] to make possible the measurement of the residual wall thickness immediately after the bubble front had passed. Flow visualisation could be used in conjunction with the ultra sound technique.

7.3.5 Shear heating of the melt

The effect of shear heating on the melt during experiments has been minimised by removing the very narrow tab gate between the runner system and the tensile test specimen. Evidence for the effect of shear heating on the wall thickness across the specimen section is presented in section 4.3.1. There has been shown to be

a link between the melt temperature and the residual wall thickness. This link could be used to indicate the extent of shear heating taking place through the gate and the temperature of the melt when the wall was formed by the bubble. Also, in terms of simulation, the shear heating of the melt during short shot is purely a melt injection issue and is not linked to the injection of gas.

Chapter 8

Summary and Conclusions

The objective of this thesis was to obtain process measurements from the gas assisted injection moulding process and to evaluate the simulation of gas assisted injection moulding cavity filling using an FE implementation of a pseudo concentration method. The validation of the simulation results focuses on comparison of wall thickness between specimens manufactured on an industrial GAIM machine and the simulated wall thickness. The major conclusions resulting from this work are as follows.

It is possible to measure wall thickness experimentally using the method outlined in chapter 3. These are suitable for direct comparison with simulation results.

8.1 Experimental conclusions

A model has been developed using a Design of Experiments approach to describe wall thickness along the cross section lines of symmetry. The model correlates process variable settings to the observed wall thickness. The model can be used to predict wall thickness given process settings that may not have been tested experimentally.

Of the major processing options, the processing variable that has the most significant effect on wall thickness is gas delay time. The gas delay time was tested over the range 0 to 10 seconds and wall thickness increased with increasing delay time.

The injection velocity of the melt into the cavity is a significant processing variable. The wall thickness increases with decreasing injection velocity. Decreased injection velocity effectively increases the gas delay time by allowing melt to sit against the cavity wall for some time before the gas trigger signal is activated by screw position.

Instability in the gas pressure signal after initial injection of gas indicates that the pressure on the cavity side of the needle is not at line pressure. This implies that the bubble does not form entirely under line pressure and may in fact form under a lower pressure that overcomes the resistance to bubble penetration. The instability can last for up to 0.6 seconds after the line pressure first increases.

8.2 Simulation conclusions

The pseudo-concentration method provides a means by which to identify the gas/melt interface. The concentration of 0.5 contour indicates the position of the boundary between the two fluids.

The geometry of the gas bubble can only be fully described by a 3D implementation of a simulation methodology. The $2\frac{1}{2}$D implementation employing flow approximations in the thickness dimension only provide summary information about the melt fraction within any given element. Summary information is of little use when attempting to compare experimentally prepared wall thickness formations in a non-trivial geometry such as a rectangle.

The mesh density influences the prediction of flow. A higher mesh density is desired, but this conflicts with the desire for a timely solution and acceptable computational resource.

The half-length specimen model efficiently provides information about the cross sectional wall thickness. For the mesh densities and thermal model studied the simulated cross-section was qualitatively, but not quantitatively accurate.

The gas bubble flow geometry from the region around the gas injection needle can be simulated. A size and position of a single point of gas injection is described and the strength of the flow source is specified.

8.3 Validation conclusions

The formation of the simulated bubble geometry is qualitatively in good agreement with the bubble geometry observed in the experimentally produced specimens. The wall thickness is consistent along the gauge length and the bubble shape is elliptical where melt collects in the corners of the rectangular section.

There is agreement between the simulation and experiment on the trend in wall thickness with set changes in process variables. This indicates that the process physics linked to key variables are captured within the simulation.

Both simulation and experiment show that gas delay time has a strong influence on the residual wall thickness. The trend in wall thickness against gas delay time is logarithmic in both cases. The rate of change in wall thickness with delay time decreases with increasing delay time.

For the mesh densities and thermal model used the simulated wall thickness is at best within 10% of the wall thickness measured experimentally, given the most closely matching process conditions and simulation control settings.

The simulated wall thickness along the LHS-RHS long section dimension is generally lower that the actual wall thickness measured experimentally. Along the FIXED-MOVING shorter dimension the simulated wall thickness is higher than the thickness measured experimentally. The simulated wall thicknesses in both dimensions reduce as the source flow rate is increased.

The gas pressure used in the experimental preparation of specimens cannot be transferred to the simulation directly. A flow rate from a source used in the simulation is difficult to calibrate against the set gas pressure.

The extent of shrinkage in the residual wall thickness between formation immediately after bubble penetration and ejection from the cavity after cooling has not been measured. An estimate of linear shrinkage of 3.9% is obtained from a material database and is based on a density change from melt to solid.

8.4 Further work

The simulation requires steps to be taken that will improve the accuracy of the wall formation over the cross section. The numerical issues associated with the simulation should be addressed. The bandwidth restriction imposed by the linear algebra library needs to be investigated and the solution code re-written to include a replacement library if necessary. The increasing of the bandwidth restriction would provide scope for greater mesh density and larger and more complex geometries.

Simulation of bubble penetration requires a number of changes to the modelling code. The boundary condition controlling the injection of melt into the cavity must be configurable such that melt injection can cease before gas injection begins. Also, the development of a method to allow gas to escape from the cavity walls to replicate venting, but retain polymer melt. Better accuracy in the prediction of wall thickness and melt fraction formation is fundamental to an accurate prediction of bubble penetration.

Other materials should be used for experimental investigations. Off-line rheometry tests will provide the rheometric data necessary for the simulation. Popular materials for gas assist applications are ABS, acetal and polyamide.

The geometry used for experimental testing has so far been of simple cross section. Other typical geometries need to be investigated, the most obvious being the ribbed plaque configuration. Simulations of this type of geometry can be done and validated against an experimentally observed bubble formation.

The machine barrel and mould should be instrumented further. A new rheometric nozzle is necessary that can take melt pressure and temperature measurements, but also incorporates a non-return valve to prevent gas penetration into the barrel. The mould may have pressure and temperature transducers placed against the mould wall. Ultra sound transducers within the mould could be used to measure the wall thickness formation immediately after bubble penetration. An array of such devices may be used to track bubble penetration through the melt at discrete locations.

Further validation of the simulation could be achieved with a transparent mould. The progress of the bubble through the melt could be observed and recorded with a video camera. Image analysis techniques could be used to estimate bubble velocity and the residual wall thickness. Transparent materials seeded with particles give scope to measure fluid velocity at the bubble tip, again using image analysis.

References

[1] L. S. Turng. Development and application of CAE technology for the gas-assisted injection molding process. *Advances in Polymer Technology*, 14(1):1–13, 1995.

[2] G. A. A. V. Haagh. *Simulation Of Gas Assisted Injection Moulding*. PhD thesis, University of Eindhoven, March 1998.

[3] K. S. Barton and L. S. Turng. General design guidelines for gas-assisted injection molding using a CAE tool. In *SPE Tech. Papers*, volume XL, pages 421–425, San Fransisco CA, USA, May 1994.

[4] GE Plastics. Gas-Assisted Injection Moulding. Design and processing guide for GE Plastics resins.

[5] Battenfeld. Airmould Gas Injection Technology, 1996.

[6] D. V. Rosato. *Injection molding handbook : the complete molding operation technology, performance and economics*. Chapman and Hall, 2 edition, 1995.

[7] H. Eckardt. Fluid-assisted injection moulding. In *Polymer Process Engineering*, pages 121–155, University of Bradford, UK, June 2001.

[8] R. Magalhaes and G. F. Smith. Investigation into heat transfer enhancement in GAIM using low temperature gas. In *Polymer Process Engineering*, pages 171–182, University of Bradford, UK, June 2001.

[9] Walter Michaeli, André Brunswick, and Marco Gruber. Step on the gas with water injection. *Kunststoffe*, 89(4):20–21, 1999.

[10] B. S. Massey. *Mechanics of Fluids*. Chapman & Hall, 6 edition, 1989.

[11] G. I. Taylor. Deposition of a viscous fluid on the wall of a tube. *Journal of Fluid Mechanics*, 10:161–165, 1961.

[12] K. W. Koelling, V. Gauri, M. Tendulkar, R. Kaminski, and O. Becker. Understanding the controlling mechanisms of gas-assisted injection molding through visualization. In *SPE Tech. Papers*, volume XLIII, pages 3697–3701, Toronto, CAN, April 1997.

[13] B. G. Cox. On driving a viscous fluid out of a tube. *Journal of Fluid Mechanics*, 14:81–96, 1962.

[14] W. B. Kolb and R. L. Cerro. Coating the inside of a capillary of square cross section. *Chemical Engineering Science*, 46(9):2181–2195, 1991.

[15] A. J. Poslinski and D. J. Coyle. Steady gas penetration through non-Newtonian liquids in tube and slit geometries: isothermal shear thinning effects. In *Polymer Processing Society*, pages 219–220, 10th annual meeting, 1994.

[16] A. J. Poslinski, P. R. Oehler, and V. K. Stokes. Isothermal gas-assisted displacement of viscoplastic liquids in tubes. *Polymer Engineering and Science*, 35(11):877–892, 1995.

[17] K. W. Koelling and R. C. Kaminski. Gas-assisted injection molding: Influence of processing conditions and material properties. In *SPE Tech. Papers*, volume XLII, pages 644–648, Indianapolis IN, USA, May 1996.

[18] V. Gauri and K. W. Koelling. Gas-assisted displacement of viscoelastic fluids: flow dynamics at the bubble front. *Journal of Non-Newtonian Fluid Mechanics*, 83(3):183–203, July 1999.

[19] S. Y. Yang, S. J. Liou, and W. N. Liou. Flow visualization of the gas-assisted injection molding process. *Advances in Polymer Technology*, 16(3):175–183, Fall 1997.

[20] S. Y. Yang and F. Z. Huang. Basic study of rib geometry for gas-assisted injection molding. In *SPE Tech. Papers*, volume XLI, pages 747–759, Boston MA, USA, May 1995.

[21] T. J. Wang, H. H. Chiang, X. Lu, and L. Fong. Computer simulation and experimental verification of gas-assisted injection molding. In *SPE Tech. Papers*, volume XLIV, pages 26–30, Atlanta GA, USA, Apr 1998.

[22] J. Zhao, X. Lu, L. Fong, and H. H. Chiang. Statistical experiment study of gas-assisted injection molding process. In *SPE Tech. Papers*, volume XLIV, pages 454–459, Atlanta GA, USA, Apr 1998.

[23] S. J. Liu and Y. C. Wu. Factors affecting the stability of gas penetration in gas assisted injection moulded bifurcation parts. *International Polymer Processing*, XV(3):297–303, 2000.

[24] S. Y. Yang and S. J. Liou. Development of moldability diagrams for gas-assisted injection molding. *Advances in Polymer Technology*, 14(3):197–205, 1995.

[25] S. Y. Yang and S. J. Liou. Influence of processing parameter on quality of gas-assisted injection-molded parts. In *SPE Tech. Papers*, volume XL, pages 408–410, San Fransisco CA, USA, May 1994.

[26] V. Kapila, N. R. Schoft, and S. Shah. Experimental study to investigate the influence of processing conditions in the gas-assisted injection molding process. In *SPE Tech. Papers*, volume XLII, pages 649–654, Indianapolis IN, USA, May 1996.

[27] S. C. Chen, J. G. Dong, W. R. Jong, J. S. Huang, and M. C. Jeng. Effect of gas channel design on molding window and part mechanical properties of gas-assisted injection molding. In *SPE Tech. Papers*, volume XLII, pages 663–667, Indianapolis IN, USA, May 1996.

[28] W. J. Fallows. *Plastics Engineering*, page 27, December 1982.

[29] S. Y. Yang and S. J. Liou. Experimental study on gas-assisted injection molding. In *SPE Tech. Papers*, volume XL, pages 404–407, San Fransisco CA, USA, May 1994.

[30] G. Sherbelis. Filling and packing cae software for gas injection molding. In *SPE Tech. Papers*, volume XL, pages 411–416, San Fransisco CA, USA, May 1994.

[31] S. C. Chen, K. F. Hsu, and K. S. Hsu. Polymer melt flow and gas penetration in gas-assisted injection moulding of a thin part with gas channel design. *International Journal of Heat and Mass Transfer*, 39(14):2957–2968, 1996. Elsevier Science Ltd.

[32] S. C. Chen, N. T. Cheng, and M. C. Jeng. Simulation of polymer melt and gas flow during gas assisted injection moulding of uniform thick part. *Plastics, Rubber and Composites Processing and Applications*, 25(1):23–28, 1996.

[33] S. C. Chen, K. S. Hsu, W. L. Liu, Y. C. Chen, and K. K. Ho. Case studies of the gas-assisted injection molded parts designed with a gas channel of different geometry. In *SPE Tech. Papers*, volume XLI, pages 530–533, Boston MA, USA, May 1995.

[34] S. Y. Hu, R. D. Chien, S. C. Chen, and Y. Kang. Investigations of structural performance of gas assisted injection moulded parts reinforced by gas channels. *Plastics, Rubber and Composites Processing and Applications*, 26(4):172–177, 1997.

[35] S. C. Chen, N. T. Cheng, and S. Y. Hu. Integrated simulations of structural performance, molding process and warpage for gas-assisted injection molded parts. *CAE and Intelligent Processing of Polymeric Materials*, 79:15–32, 1997. ASME.

[36] S. C. Chen, S. Y. Hu, and Y. P. Chang. Integrated simulations of gas injection molding process and part structural performance under a unified model. In *SPE Tech. Papers*, volume XLV, pages 566–570, New York City NY, USA, May 1999.

[37] S. C. Chen, N. T. Cheng, and K. S. Hsu. Simulation and verification of the secondary gas penetration in a gas assisted injection molded spiral tube. *International Communications in Heat and Mass Transfer*, 22(3):319–328, May 1995.

[38] G. A. A. V. Haagh and F. N. van de Vosse. Simulation of three dimensional polymer mould filling processes using a pseudo-concentration method. *International Journal for Numerical Methods in Fluids*, 28:1355–1369, 1998.

[39] G. A. A. V. Haagh and H. Zuidema. Towards a 3-D finite element model for the gas-assisted injection moulding process. *International Journal for Numerical Methods in Fluids*, 12(3):207–215, 1997. Hanser.

[40] IKV Aachen. Video entitled gas injection technique.

[41] S. C. Chen, N. T. Cheng, and S. Y. Hu. Simulations of primary and secondary gas penetration for a gas-assisted injection-molded thin part with gas channel. *Journal of Applied Polymer Science*, 67(9):1553–1564, February 1998.

[42] T. Coupez, D. Daboussy, and E. Bigot. Mesh adaptation for 3D injection numerical simulation. In *Polymer Processing Society*, number 397, 15th annual meeting,'s-Hertogenbosch, NL, May 1999.

[43] Battenfeld, Austria. *CDK750 with Airmould and Unirob 4000.*

[44] R. G. Speight. *In-line process measurements for injection moulding control.* PhD thesis, University of Bradford, UK, 1993.

[45] C. Peters, J. B. Hull, P. D. Coates, and R. G. Speight. In-line process monitoring for injection moulding control. *Journal of Process Mechanical Engineering*, 211(2):115–128, 1997.

[46] National Instruments. PCI E series user manual. Multifuncional I/O boards for PCI bus computers, 1999.

[47] MTS systems corporation. Product manual: LP series magnetorestrictive linear displacement trasducers.

[48] Dynisco. Product catalogue, May 2000.

[49] R. G. Speight, P. D. Coates, J. B. Hull, and C. Peters. In-line process monitoring for injection moulding control. *Proceedings of the IMechE*, 211(E):115–128, 1997.

[50] A. J. Dawson. *Process and production measurements for automatic inspection and control of injection moulding.* PhD thesis, University of Bradford, 1999.

[51] BSI. BS EN ISO 178:1997, BS 2782-3:Method 335 A 1993 (ISO 178:1993). Plastics – determination of flexural properties.

[52] J. Moller and M. Carlson. Post-ejection cooling behaviour of injection molded parts. In *SPE Tech. Papers*, volume XLIV, pages 525–527, Atlanta GA, USA, April 1998.

[53] D. M. Grove and T. P. Davis. *Engineering, quality and experimental design.* Harlow, Essex, England Longman Scientific, 1992.

[54] W. Y. Fowlkes and C. M. Creveling. *Engineering methods for robust product design: using Taguchi methods in technology and product development.* Engineering process improvement. Addison-Wesley, 1995.

[55] R. J. Freund and W. J. Wilson. *Regression analysis: statistical modelling of a response variable.* Academic press, 1998.

[56] K. A. Stroud. *Engineering Mathematics.* Macmillan, 3 edition, 1987.

[57] D. C. Montgomery. *Design and Analysis of Experiments.* John Wiley and sons Inc, 3 edition, 1991.

[58] BP chemicals Ltd. Material specification for Rigidex HDPE 5050 EA.

[59] Moldflow Corportaion. VISDAT material database.

[60] J. D. Anderson. *Computational fluid dynamics: the basics with applications.* Mechanical Engineering. McGraw-Hill, 1995.

[61] H. Schlichting. *Boundary layer theory.* Mechanical Engineering. McGraw-Hill, 4 edition, 1960.

[62] C. W. Macosko. *Rheology principles, measurements and applications.* VCH, 1994.

[63] M. M. Cross. Analysis of flow data on molten polymers. *European Polymer Journal*, 2:299–307, 1966. Pergamon press Ltd.

[64] M. M. Cross. Relation between viscoelasticity and shear-thinning behaviour on liquids. *Rheologica Acta*, 5:609–614, 1979.

[65] C. L. Tucker. *Fundamentals of computer modelling for polymer processing.* Computer aided engineering for polymer processing. Hanser, 1989.

[66] B. E. VerWeyst, C. L. Tucker, P. H. Foss, and J. F. O'Gara. Fibre orientation in 3-D injection moulded features: prediction and experiment. In *Polymer Processing Society*, number 390, 15th annual meeting,'s-Hertogenbosch, NL, May 1999.

[67] J. D. Ferry. *Viscoelastic properties of polymers.* John Wiley & sons, Inc (NY), 1961.

[68] R. A. Mendelson. Prediction of melt viscosity flow curves at various temperatures for some olefin polymers and copolymers. *Polymer Engineering and Science*, 8(3):235–240, 1968.

[69] J. N. Reddy. *An introduction to the finite element method*. Engineering Mechanics. McGraw-Hill, 2 edition, 1993.

[70] C. T. Shaw. *Using computational fluid dynamics*. Prentice Hall, 1992.

[71] H. Kardestuncer, editor. *Finite elements handbook*. McGraw Hill, 1987.

[72] L. Johnson, P. Olley, and P. D. Coates. Gas assisted injection moulding: finite element modelling and experimental validation. *Plastics, Rubber and Composites*, 29(1):31–37, 2000.

[73] Conversation with Dr. Peter Olley, University of Bradford. Dated 13 September 2001 as part of a supervisory meeting.

[74] Dr Mike Woodhead, IRC in Polymer Science and Technology, University of Bradford, provided the rheological data for the BP HDPE 5050EA.

[75] J. A. Brydson. *Plastics materials*. Butterworths, 5 edition, 1989.